Doctorate of National Interest

on

Space Science and Technology

Study for Nanosatellites of Multiscale Temporal Evolution of Quasi-Periodic Pulsations in X-Class Solar Flares

Characterization of Quasi Periodic Oscillations with fast X/Gamma-ray Detectors

PhD Student: Archana Giri Nair

Supervisor: Prof. Francesco Berrilli

Co-Supervisor: Prof. Dario Del Moro

September 2026

Abstract

Solar flares are among the most energetic phenomena in the heliosphere, releasing up to 10^{32} erg of magnetic energy within minutes to hours. The temporal structure of this energy release is highly complex, often exhibiting quasi-periodic pulsations (QPPs) across timescales ranging from fractions of a second to several minutes. Despite decades of research, the physical origin of these pulsations remains unresolved.

This thesis investigates the multiscale temporal evolution of QPPs in X-class solar flares using high-cadence X-ray observations from the Spectrometer/Telescope for Imaging X-rays (STIX) onboard Solar Orbiter. The Hilbert-Huang Transform—combining Empirical Mode Decomposition (EMD) with Hilbert spectral analysis—is employed to extract instantaneous frequency and energy information from five X-class flare light curves in the 16–28 keV energy band. This adaptive method overcomes the limitations of traditional Fourier-based approaches for non-stationary flare signals. The reliability of the EMD-Hilbert pipeline is assessed through synthetic-data experiments with known oscillatory components and correlated noise

The analysis reveals recurrent frequency concentrations spanning low (∼6–10 mHz), intermediate (∼18–30 mHz), and higher (∼45–70 mHz) ranges across the analyzed events. The low and intermediate components are consistent with standing Alfvénic modes in coronal loops. The high-frequency components, predominantly observed during the decay phase, point to nonlinear energy transfer.

A key finding is the transition from resonance-dominated impulsive phase to turbulence-dominated decay phase, with power-law spectral scaling $\beta \approx 1.8 \pm 0.1$ during the decay phase. This scaling agrees with theoretical predictions for reduced magnetohydrodynamic (RMHD) turbulence in coronal loops (Nigro et al., 2008).

The results demonstrate that QPPs manifest the interplay between resonant wave excitation, fragmented reconnection, and turbulent cascade processes. This unified interpretation provides new observational constraints on flare energy release.

Additionally, this thesis supports the Sun CubE OnE (SEE) mission, a proposed 12U CubeSat for high-cadence solar monitoring. Laboratory characterization of Silicon Photomultiplier (SiPM) detectors validates compact detector systems for nanosatellite-based flare observations, establishing key requirements for future space weather missions.

Keywords: solar flares, quasi-periodic pulsations, MHD, magnetic reconnection, RMHD turbulence, Hilbert-Huang Transform, STIX, CubeSat, space weather

Acknowledgements

First and foremost, I would like to express my deepest gratitude to my parents, Bavani and Giri, and my brother Arjun, whose unwavering belief in me has been my greatest source of strength throughout this journey. Their encouragement, sacrifices, and constant motivation have shaped me into the person I am today. They have always stood by me in every decision I made, offering support without hesitation and reminding me never to give up on my dreams. I dedicate this thesis to them, for their love and faith in me, which have been my foundation.

I am profoundly grateful to my supervisor, Prof. Francesco Berrilli, for his guidance, patience, and unwavering support throughout my PhD journey. His friendly demeanor and ever-present smile made this research feel manageable. He listened to my ideas and provided thoughtful feedback that helped me grow as a researcher. His trust in my abilities and his willingness to let me explore my own scientific questions gave me the confidence to push the boundaries of this work.

I extend my sincere thanks to Prof. Dario Del Moro and Dr Luca Giovanelli for their guidance and support. And special thanks to Dr Giuseppina Nigro, whose foundational findings provided the crucial theoretical framework for this research.

I am greatly thankful to my friends, Anjana and Ardra, who have been my pillars of support throughout this long journey. Their constant encouragement, late-night conversations, and willingness to listen whenever I needed to talk made the difficult days in my life bearable and the good days even better. Their friendship has been a source of joy and strength.

I would also like to acknowledge my colleagues and fellow researchers at the Solar Physics Laboratory of the University of Rome Tor Vergata: Fallon, Matteo, Ronish, Letizia, Raffaele, and Andrea. Their camaraderie and support helped me immensely throughout this journey. Fallon has been a wonderful friend whom I could always reach out to, regardless of the distance between us; she always offered resources, suggestions, and a patient ear for my rants. Ronish was always there to hear me out and provide thoughtful advice and suggestions. Matteo never failed to make us laugh, and I cannot thank him enough for his invaluable help with bureaucracy and translations. Letizia, Raffaele, and Andrea were amazing friends who gave me unforgettable memories in the lab and were always ready to assist with translations and administrative matters. I am truly grateful to each of them for making this journey so memorable.

My sincere appreciation goes to my husband, Amaldev, for supporting me through the last phase of this PhD. Also helping me earn one other title during the course of this journey—one that I will cherish forever. I am forever grateful for his love and companionship.

Finally, I would also like to acknowledge the Doctorate of National Interest in Space Science and Technology, University of Trento and University of Rome Tor Vergata, for providing an inspiring research opportunity to pursue this work. I thank the Italian Space Agency for supporting the Sun CubE OnE (SEE) mission. The STIX team for providing the high-quality data that made this analysis possible. I am also grateful to the developers of the open-source scientific software used in this work, including the EMD Python package, NumPy, SciPy, and Matplotlib, which were indispensable tools in this research.

Contents

Abstract **1**

1 The Active Sun: Magnetic Activity, Space Weather, and High-Energy Solar Variability **1**

1.1 Introduction . . . 1

1.2 The Sun as a Magnetically Active Star . . . 3

1.2.1 Generation of the Solar Magnetic Field . . . 3

1.2.2 Magnetic Energy Storage in the Corona . . . 5

1.3 Magnetohydrodynamics in the Solar Corona . . . 7

1.3.1 The Magnetohydrodynamic Framework . . . 7

1.3.2 Wave Modes and Oscillatory Dynamics . . . 8

1.3.3 Multiscale Dynamics and Turbulent Energy Cascades . . . 9

1.4 Magnetic Reconnection and Solar Flares . . . 10

1.4.1 The Energy Release Problem . . . 10

1.4.2 Magnetic Reconnection . . . 11

1.4.3 Intermittent Reconnection and QPP Generation . . . 13

1.5 Solar Drivers of Space Weather . . . 13

1.5.1 Solar Flares . . . 14

1.5.2 Coronal Mass Ejections . . . 16

1.5.3 Solar Wind and Interplanetary Magnetic Field . . . 18

1.5.4 Geomagnetic Storms and Space Weather Impacts . . . 18

1.6 Motivation and Scope of This Thesis 20

2 The Sun CubE OnE (SEE) Mission and High-Cadence Solar X-Ray Instrumentation 22

2.1 The Sun CubE OnE (SEE) Mission 22

2.1.1 Science Objectives 24

2.1.2 Spacecraft Platform 25

2.1.3 Scientific Payload 26

2.1.4 Orbit and Mission Planning 29

2.2 Instrumentation for Solar Flare Studies on Nanosatellites 30

2.2.1 Overview of High-Energy Solar Instrumentation 31

2.2.2 Constraints in CubeSat-Based X/Gamma Detectors 31

2.3 Design and Characterization of the SEE X/Gamma Detector 32

2.3.1 X/Gamma Detector 32

2.3.2 Readout Electronics and Data Processing 33

2.4 Observational Motivation and Connection to QPP Studies 35

2.5 Chapter Summary 37

3 Theoretical Models for Quasi-Periodic Pulsations in Solar Flares 38

3.1 Introduction 38

3.2 MHD Oscillations of Coronal Loops 40

3.2.1 Fundamental MHD Wave Modes 40

3.2.2 Standing Kink Modes 41

3.2.3 Standing Sausage Modes 42

3.2.4 Alfvénic Modes 42

3.2.5 Observational Signatures and Predictions 43

3.3 Oscillatory Reconnection and Plasmoid Dynamics 43

3.3.1 Plasmoid Instability 44
3.3.2 Plasmoid Coalescence 44
3.3.3 Plasmoid-Induced Reconnection 45
3.3.4 Observational Signatures and Predictions 45
3.4 RMHD Turbulence and Coronal Loop Models 46
3.4.1 RMHD Turbulence Model 46
3.4.2 Turbulent Cascade and QPP Generation 47
3.4.3 Spectral Evolution of Flare Emission 48
3.4.4 Observational Signatures 48
3.4.5 Testing MHD Wave Models 49
3.4.6 Testing Reconnection Models 49
3.4.7 Testing Turbulence Models 49
3.5 Summary 51

4 Results - I **52**

4.1 Empirical Mode Decomposition of Stix X-ray signal 52
4.2 Identification of Intrinsic Mode Functions 57
4.3 Instantaneous Frequency Distribution 59
4.3.1 Characteristics of the Frequency Distribution 60
4.3.2 Phase-Dependent Frequency Evolution 62
4.3.3 Physical Interpretation of Frequency Components 64
4.3.4 Nonlinear Nature of the Frequency Evolution 65
4.3.5 Implications for Quasi-Periodic Pulsations 65
4.4 Oscillatory Behavior During the Impulsive Phase 66
4.5 Long-Period Oscillations and Loop Dynamics 69
4.6 Oscillatory Behavior During the Decay Phase 71
4.7 Energy Evolution of Oscillatory Components 75

4.8 Multiscale Nature of Flare Dynamics 78
4.9 Wavelet Analysis and Comparison with Empirical Mode Decomposition . 80
4.9.1 Wavelet Transform Results 80
4.9.2 Comparison with EMD Results 80
4.10 Summary of Results 81

5 Results - II 84

5.1 Multiscale Frequency Structure of QPPs 84
5.2 Alfvén Timescale Constraints and Loop Resonance 85
5.3 Nonlinear Energy Transfer in the RMHD Framework 86
5.4 The Nigro et al. (2008) Coronal Loop Model 87
5.5 Spectral Evolution from Impulsive to Decay Phase 88
5.5.1 Quantitative Spectral Scaling 89
5.6 Consistency with RMHD Turbulence 91
5.7 Physical Interpretation 92
5.8 Implications for Flare Energy Dissipation 92
5.9 Summary 93

6 Conclusion 94

6.1 Summary of Main Findings and Contributions 94
6.2 Fulfillment of Research Objectives 96
6.3 Limitations of the Current Study 96
6.4 Implications for Space Weather Sources Understanding 98
6.5 Recommendations for SEE and Space Weather Missions 99
6.6 Final Remarks 99

A Detailed List and Results of the Analyzed Flares 101

A.1 Empirical Mode Decomposition 101

A.2 Instantaneous Frequency Analysis 105
A.3 Energy Analysis 108
A.4 Wavelet Analysis 110

B Synthetic Validation of the EMD–Hilbert Pipeline 113

B.1 Introduction 113
B.2 Synthetic Signal Construction 114
B.2.1 Flare-like Envelope 114
B.2.2 Injected Oscillatory Components 115
B.2.3 Correlated Noise 116
B.3 Analysis Pipeline 117
B.4 Validation Scenarios 117
B.5 Recovery Results 118
B.5.1 Recovery of the Low- and Intermediate-Frequency Components . 119
B.5.2 High-Frequency Component 119
B.5.3 Effect of Noise 120
B.5.4 Effect of Signal Duration 120
B.5.5 Dependence on the Noise Realization 121
B.6 Bootstrap Analysis of the KDE Frequency Distribution 121
B.7 Frequency-Recovery Limitations 122
B.8 Synthetic Validation Figures 123
B.9 Implications for the STIX Analysis 123
B.9.1 Identification of Candidate Frequency Bands 123
B.9.2 Interpretation of Low-Frequency Components 128
B.9.3 Interpretation of High-Frequency Components 128
B.9.4 Implications for Frequency-Drift Measurements 129
B.10 Limitations of the Synthetic Validation 129

B.11 Summary 130

List of Figures

1.1 Solar cycle sunspot numbers 4
1.2 White-light image of an active region observed by SDO/HMI, showing dark sunspots where strong magnetic fields suppress convective heat transport. Sunspots typically appear in pairs of opposite magnetic polarity. Data courtesy of NASA/SDO and the HMI science team. 5
1.3 SDO/AIA image (171 Å) showing coronal loops in an active region (left) with a magnified view of a loop system (right). 6
1.4 CSHKP model for solar flares that explains their observable features on the basis of magnetic reconnection. Circles mark the emission from all key points. (Adapted from Christe et al. (2017)). 12
1.5 The GOES X-ray profile of SOL03102024 which was one of the flares used for the study. The area marked in green from the onset of the flare to the end. The yellow dotted line shows the peak of the flare. Data courtesy of NOAA/NCEI. 15
1.6 A Coronal Mass Ejection event happened on 4th January 2002 imaged by SOHO/LASCO C2 coronagraph.Data courtesy of ESA/NASA 17
1.7 A schematic representation of Solar wind and Earth magnetosphere interaction. 19

2.1 Artistic depiction of Sun CubE OnE (SEE) Cubesat 23
2.2 Argotec HAWK platform 25

2.3 SEE UV payload 27
2.4 Silicon Photomultiplier (SiPM)-Scintillator detector. Schematic of the SiPM-scintillator detector module showing the scintillator crystal coupled to SiPM array. 28
2.5 Testing of 4x4 pixel SiPM in the Solar Physics Lab of University of Rome Tor Vergata 34
2.6 Preliminary testing of pulse duration and readout time 35
2.7 Readout Electronics 36

4.1 The figure on the top shows the Location of the flare SOL03032023 and the below is the GOES X-ray profile of the flare 55
4.2 The Intrinsic Mode Functions (IMFs) of SOL03032023 58
4.3 The Instantaneous frequency (IFs) of SOL03032023 61
4.4 Instantaneous frequency profile during the impulsive phase of IMF2 of SOL03032023 67
4.5 KDE fit of the frequency distribution of IMF2 of SOL03032023 during the impulsive phase 68
4.6 Instantaneous frequency profile during the decay phase of IMF2 of SOL03032023 72
4.7 KDE fit of the frequency distribution of IMF2 of SOL03032023 during the decay phase. 74
4.8 Energy profile of IMF2 of SOL03032023 76
4.9 Wavelet transform of SOL20230303 81

A.1 Intrinsic Mode Functions (IMFs) for SOL2023-07-02 (X1.1 flare). Lower-order IMFs correspond to high-frequency oscillations, while higher-order IMFs capture long-period variations. 102
A.2 Intrinsic Mode Functions (IMFs) for SOL2024-10-03 (X9.0 flare). 103
A.3 Intrinsic Mode Functions (IMFs) for SOL2024-05-11 (X5.9 flare). 104

A.4 Intrinsic Mode Functions (IMFs) for SOL2023-01-06 (X1.2 flare). 104
A.5 Instantaneous frequency profiles for SOL2023-07-02 (X1.1 flare). The IF of IMF2 shows the evolution of dominant oscillatory frequencies throughout the flare duration. 105
A.6 Instantaneous frequency profiles for SOL2024-10-03 (X9.0 flare). 106
A.7 Instantaneous frequency profiles for SOL2023-01-06 (X1.2 flare). 107
A.8 Instantaneous frequency profiles for SOL2024-05-11 (X5.9 flare). 107
A.9 Instantaneous energy evolution of IMF2 for SOL2023-07-02 (X1.1 flare). . 108
A.10 Instantaneous energy evolution of IMF2 for SOL2024-05-11 (X5.9 flare). . 108
A.11 Instantaneous energy evolution of IMF2 for SOL2024-10-03 (X9.0 flare). . 109
A.12 Instantaneous energy evolution of IMF2 for SOL2023-01-06 (X1.2 flare). . 109
A.13 Wavelet power spectrum for SOL2024-05-11 (X5.9 flare). Significant power above the 95% red-noise level is predominantly confined to periods between approximately 50 s and 200 s. 110
A.14 Wavelet power spectrum for SOL2023-01-06 (X1.2 flare). 111
A.15 Wavelet power spectrum for SOL2023-07-02 (X1.1 flare). 111
A.16 Wavelet power spectrum for SOL2024-10-03 (X9.0 flare). A well-defined ridge around 100 s is observed, representing the dominant QPP period. . 112

B.1 Synthetic validation for the ideal, noise-free signal. The figure shows the constructed signal, injected oscillatory components, recovered IMFs, instantaneous-frequency distributions, KDE results, frequency-recovery comparison, and residuals. 124
B.2 Synthetic validation for the low-noise case. The correlated-noise realization has an SNR of approximately 34.0 dB. Three of the four injected frequency components satisfy the matching criterion used in the validation analysis. 125

B.3 Synthetic validation for the medium-noise case. The synthetic signal has an SNR of approximately 24.5 dB. Three of the four injected components satisfy the matching criterion, illustrating the effect of correlated noise and IMF redistribution on frequency recovery. 126
B.4 Synthetic validation for the high-noise case. The calculated SNR is approximately 18.5 dB. Four of the four injected components satisfy the matching criterion in this particular realization. The result illustrates why a single noise realization is insufficient for defining a universal SNR-dependent detection threshold. 127

List of Tables

3.1 Observational predictions of competing QPP models 50

4.1 Summary of solar flare events analyzed in this study. STIX light curves were obtained in the 16-28 keV energy band. 54
4.2 Parameters used in the EMD/Hilbert analysis pipeline. 56
4.3 Dominant frequency peaks derived from KDE distributions during the impulsive phase of analyzed flares. Values represent median peak frequencies from 500 bootstrap resamples with 95% confidence intervals in parentheses. 63
4.4 Dominant frequency peaks derived from KDE distributions during the decay phase of analyzed flares. Values represent median peak frequencies from 500 bootstrap resamples with 95% confidence intervals in parentheses. 63
4.5 Comparison of wavelet (Morlet) and EMD+Hilbert methods for QPP analysis. 82

5.1 Estimated spectral slopes of the QPP frequency distribution for impulsive and decay phases. The spectral index β is defined by $E(f) \propto f^{-\beta}$. Values represent mean $\beta \pm 1\sigma$ from 1000 bootstrap resamples, with R^2 indicating the goodness-of-fit for the decay-phase power-law fit. 91

6.1 Comparison of QPP periods identified in this study with prior surveys of solar flare quasi-periodic pulsations. 95

B.1 Synthetic validation scenarios used in the EMD–Hilbert analysis. 118

B.2 Performance of the EMD–Hilbert pipeline for the synthetic validation signals. "Matched peaks" denotes the number of injected frequencies for which a recovered KDE peak was found within the matching criterion used in the validation analysis. 118

Chapter 1

The Active Sun: Magnetic Activity, Space Weather, and High-Energy Solar Variability

1.1 Introduction

The Sun is the nearest astrophysical laboratory in which highly nonlinear plasma processes can be studied in exceptional observational detail. Although the Sun appears relatively stable in visible light, observations across the electromagnetic spectrum reveal that its atmosphere is profoundly dynamic and continuously reshaped by magnetic activity. This activity manifests itself through a broad range of phenomena, including sunspots, prominences, coronal heating, solar flares, coronal mass ejections (CMEs), and continuous variations in the solar wind. Together, these processes govern the structure and dynamics of the heliosphere and strongly influence the near-Earth space environment (Fletcher, 2024; Schrijver, 2009; Shibata, 1998). The fundamental physics underlying these phenomena is governed by the principles of magnetohydrodynamics (MHD) and plasma physics (Biskamp, 2003; Priest & Forbes, 2001).

The origin of solar activity lies in the magnetic field generated within the solar interior through dynamo processes operating in the convection zone. Differential rotation and convective plasma motions amplify and reorganize magnetic fields, which subsequently emerge through the photosphere into the solar atmosphere (Shibata & Magara, 2011). Once in the corona, magnetic fields dominate the plasma dynamics and store vast amounts of free energy capable of powering eruptive phenomena.

Among the different manifestations of solar magnetic activity, solar flares represent one of the most efficient and rapid conversions of magnetic energy into radiation, plasma heating, bulk plasma motion, and non-thermal particle acceleration. These events release energies ranging from 10^{28} to 10^{32} erg over timescales spanning seconds to hours (Shibata & Magara, 2011). Observations in X-rays and γ-rays demonstrate that flare emission is highly structured in time, often exhibiting rapid fluctuations and burst-like behavior that reflect the underlying complexity of the energy release process (Fletcher, 2024).

One of the most intriguing observational signatures associated with solar flares is the presence of quasi-periodic pulsations (QPPs), which appear as oscillatory or intermittent modulations in flare light curves across multiple wavelengths. QPPs have been detected in radio, optical, EUV, soft X-ray, hard X-ray, and γ-ray observations, with characteristic timescales ranging from fractions of a second to several minutes (Nakariakov & Melnikov, 2009; Van Doorsselaere et al., 2016). Despite decades of study, the physical origin of these pulsations remains unresolved. Proposed mechanisms include magnetohydrodynamic (MHD) oscillations in coronal loops, oscillatory magnetic reconnection, periodic particle acceleration, plasmoid-mediated reconnection, and turbulence-driven intermittent dissipation processes (McLaughlin et al., 2018; Shibata & Magara, 2011).

Understanding such variability requires both theoretical and observational advances. From a theoretical perspective, flare variability emerges from the interaction between large-scale magnetic structuring and small-scale dissipation processes occurring in highly nonlinear plasma environments (Schrijver, 2009). From an observational perspective, the detection of rapid temporal variability requires instruments capable of high-cadence observations in high-energy wavelength bands.

Recent developments in compact detector technologies and nanosatellite platforms have created new opportunities for high-time-resolution solar observations. In particular, Silicon Photomultiplier (SiPM)-based detectors provide compact and sensitive systems suitable for observing rapid X-ray variability associated with flare dynamics. These technological developments motivate the observational framework of the present thesis.

This chapter establishes the physical context necessary for the investigation presented in this work. It first introduces the Sun as a magnetically active star and discusses the role of magnetohydrodynamics in shaping coronal dynamics. It then examines the physical processes responsible for magnetic energy storage and explosive energy release through magnetic reconnection. The chapter further discusses the principal drivers of space weather and their interaction with the heliospheric environment. Finally, the chapter introduces the motivation for high-cadence solar observations and the scientific importance of studying quasi-periodic pulsations in solar flare emission.

1.2 The Sun as a Magnetically Active Star

1.2.1 Generation of the Solar Magnetic Field

The Sun's magnetic field is generated through dynamo processes operating within the convection zone. The combined effects of differential rotation and turbulent convective motions transform kinetic energy into magnetic energy, producing large-scale magnetic fields that evolve over the solar cycle (Schrijver, 2009; Shibata & Magara, 2011).

One of the most visible manifestations of solar magnetic activity is the approximately 11-year solar cycle (Hathaway, 2015; Schwabe, 1844), during which the number of sunspots and the overall level of solar activity vary significantly. During solar maxi-

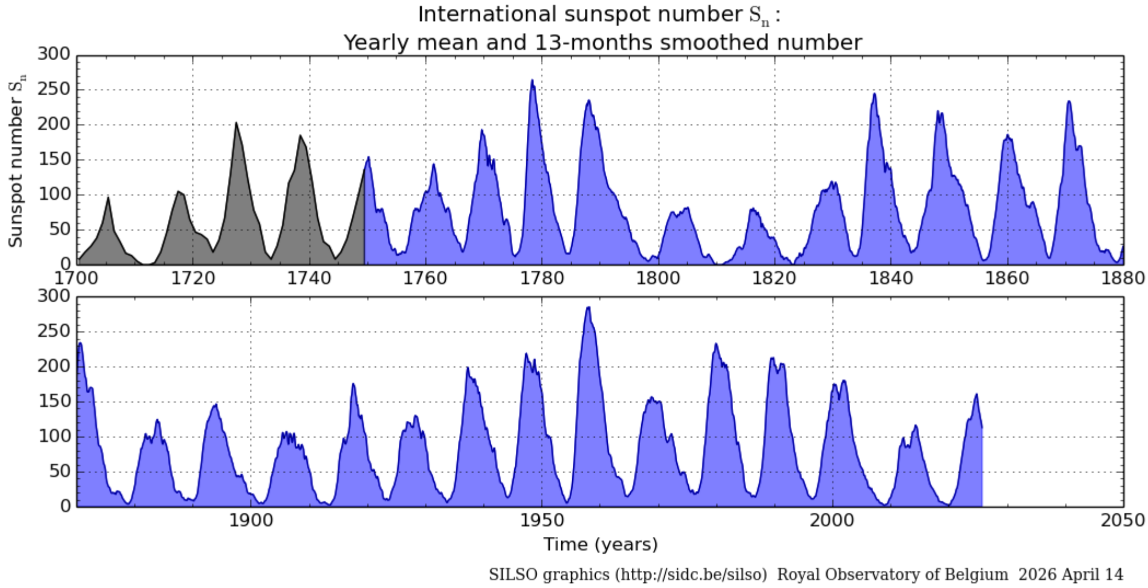

Figure 1.1: Monthly averaged sunspot numbers from 1750 to the present, showing the approximate 11-year solar cycle. The alternating maxima and minima correspond to periods of high and low solar magnetic activity, respectively. Data from SILSO (Royal Observatory of Belgium).

mum, active regions containing strong magnetic fields become highly abundant, increasing the probability of eruptive events such as solar flares and CMEs. Conversely, solar minimum is characterized by relatively weak magnetic activity and fewer eruptive phenomena (Fletcher, 2024).

Sunspots correspond to regions of concentrated magnetic flux where magnetic field strengths may reach several thousand gauss. In these regions, magnetic pressure suppresses convective heat transport from the solar interior, producing lower temperatures relative to the surrounding photosphere and causing the regions to appear darker in visible light (Shibata & Magara, 2011).

The emergence of magnetic flux from the solar interior into the atmosphere is a critical process in solar activity. Emerging magnetic structures interact with pre-existing coronal magnetic fields, generating increasingly complex magnetic topologies capable of storing substantial free magnetic energy (Schrijver, 2009).

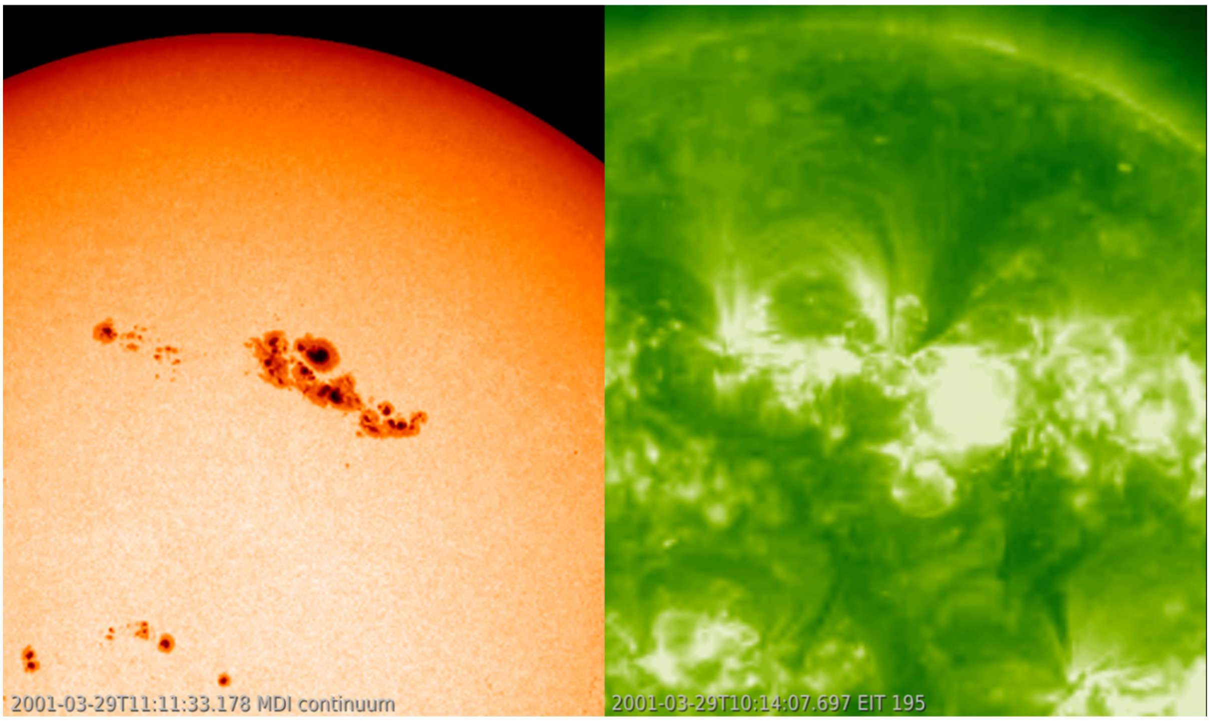

Figure 1.2: White-light image of an active region observed by SDO/HMI, showing dark sunspots where strong magnetic fields suppress convective heat transport. Sunspots typically appear in pairs of opposite magnetic polarity. Data courtesy of NASA/SDO and the HMI science team.

1.2.2 Magnetic Energy Storage in the Corona

The solar corona represents a low-density and magnetically dominated plasma environment. A useful quantity characterizing the relative importance of magnetic and thermal forces is the plasma-β parameter (Shibata & Magara, 2011):

$$\beta = \frac{2\mu_0 n k_B T}{B^2}, \tag{1.1}$$

where n is the plasma density, T is the temperature, and B is the magnetic field strength.

Under typical coronal conditions, the plasma-β parameter is much smaller than unity, implying that magnetic pressure dominates over thermal pressure. Consequently, plasma motions become strongly constrained by magnetic field structures, and magnetic

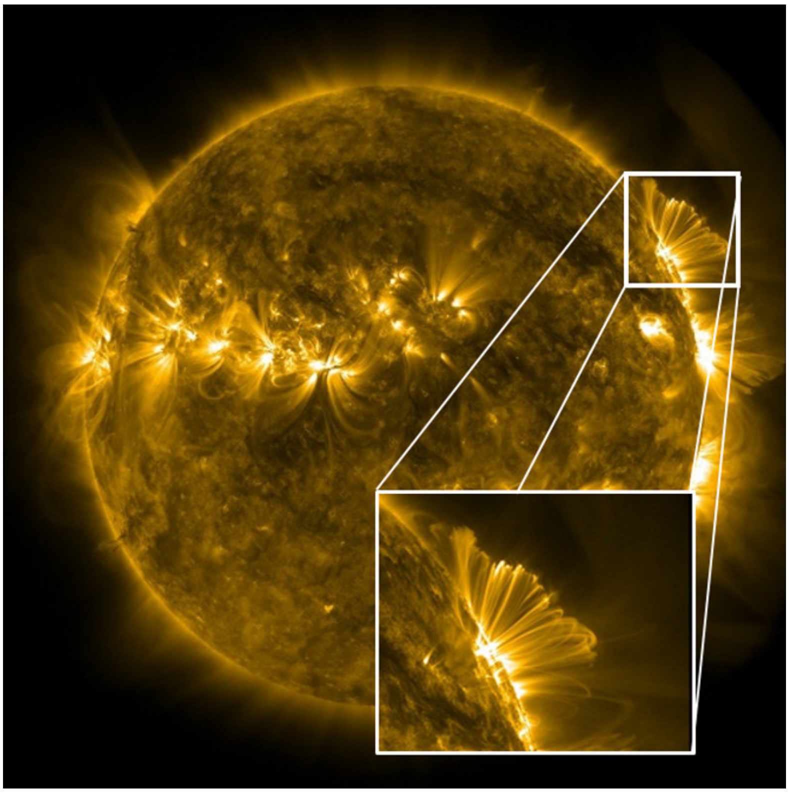

Figure 1.3: SDO/AIA image (171 Å) showing coronal loops in an active region (left) with a magnified view of a loop system (right).

stresses govern the large-scale evolution of the corona (Fletcher, 2024).

The total magnetic energy stored within an active region of characteristic size L can be approximated by:

$$E_{\mathrm{mag}} \approx \frac{B^2}{8\pi} L^3. \tag{1.2}$$

For typical coronal magnetic fields and active-region scales, the total stored magnetic energy can exceed 10^{33} erg (Shibata & Magara, 2011). However, only the excess energy above the minimum-energy potential field configuration can be released during eruptive events. This excess energy is commonly referred to as the free magnetic energy:

$$E_{\mathrm{free}} = E_{\mathrm{total}} - E_{\mathrm{potential}}. \tag{1.3}$$

The accumulation of free magnetic energy occurs through several coupled processes. Photospheric footpoint motions continuously shear and braid magnetic field lines, while emerging magnetic flux introduces new currents and magnetic complexity into the corona (Schrijver, 2009). Over time, these processes generate highly non-potential magnetic structures such as sheared arcades and twisted magnetic flux ropes.

An important quantity associated with magnetic complexity is magnetic helicity, defined as:

$$H = \int_V \mathbf{A} \cdot \mathbf{B} \, dV, \tag{1.4}$$

where $\mathbf{A}$ is the magnetic vector potential. Magnetic helicity is approximately conserved even under resistive conditions and therefore constrains the evolution of coronal magnetic structures (Shibata & Magara, 2011).

As magnetic energy and helicity accumulate, the coronal magnetic configuration may approach instability thresholds that eventually trigger eruptive phenomena (Schrijver, 2009).

1.3 Magnetohydrodynamics in the Solar Corona

1.3.1 The Magnetohydrodynamic Framework

The dynamics of the solar corona are well described within the framework of magnetohydrodynamics (MHD), which treats the plasma as an electrically conducting fluid interacting with electromagnetic fields (Shibata & Magara, 2011).

In highly conducting plasmas such as the solar corona, magnetic field lines are approximately frozen into the plasma flow. This frozen-in condition implies that plasma motions transport magnetic field structures, while magnetic tension and pressure simultaneously influence plasma dynamics (Fletcher, 2024).

The characteristic speed associated with magnetic disturbances in the plasma is the Alfvén speed:

$$v_A = \frac{B}{\sqrt{\mu_0 \rho}}, \tag{1.5}$$

where ρ represents the plasma density.

For typical coronal conditions, the Alfvén speed reaches values of order 10^3 km s^{-1}, significantly exceeding the coronal sound speed. This indicates that magnetic forces dominate many dynamical processes occurring in the corona (Shibata & Magara, 2011).

The characteristic dynamical timescale associated with magnetic structures is therefore given by the Alfvén transit time:

$$t_A = \frac{L}{v_A}. \tag{1.6}$$

For coronal loops with lengths of order 10^4–10^5 km, the resulting timescales range from several seconds to a few minutes. Interestingly, these timescales are comparable to those frequently observed in flare QPPs, suggesting that at least some forms of flare variability may be associated with MHD wave processes or resonant dynamics in coronal structures (Nakariakov & Melnikov, 2009).

1.3.2 Wave Modes and Oscillatory Dynamics

Magnetized plasmas support several classes of MHD wave modes, including Alfvén waves, slow magnetoacoustic waves, and fast magnetoacoustic waves (Shibata & Magara, 2011). In structured coronal loops, these waves may form standing oscillatory modes whose frequencies depend on loop geometry, plasma density, and magnetic field strength.

For example, the fundamental standing Alfvén mode in a loop of length L possesses a characteristic frequency:

$$\omega_A = \frac{\pi v_A}{L}. \tag{1.7}$$

Such oscillatory processes have frequently been proposed as possible explanations for quasi-periodic pulsations observed during solar flares (Nakariakov & Melnikov, 2009; Van Doorsselaere et al., 2016).

However, purely wave-based interpretations remain insufficient to explain all observed flare variability. Many flare light curves exhibit highly intermittent and broadband fluctuations inconsistent with coherent monochromatic oscillations. This suggests that flare variability may emerge from a combination of resonant MHD dynamics and nonlinear energy release processes (McLaughlin et al., 2018).

1.3.3 Multiscale Dynamics and Turbulent Energy Cascades

One of the fundamental challenges in solar physics concerns the transfer of energy across vastly separated spatial scales. Energy injection occurs primarily through large-scale photospheric motions at scales of 10^3–10^4 km, whereas dissipation ultimately occurs at microscopic kinetic scales (Shibata & Magara, 2011).

The enormous separation between injection and dissipation scales requires nonlinear transfer processes capable of redistributing energy across scales. Turbulence provides one possible mechanism for this transfer (McLaughlin et al., 2018).

Within turbulent systems, energy cascades from large scales toward progressively smaller structures through nonlinear interactions. The turbulent energy transfer rate may be approximated by:

$$\epsilon \sim \frac{v_\ell^3}{\ell}, \tag{1.8}$$

where v_ℓ represents the characteristic velocity fluctuation at scale ℓ (Shibata & Magara, 2011).

The role of turbulence in the corona has become increasingly important in modern flare models. Numerical simulations and theoretical studies suggest that reconnecting current sheets may fragment into complex plasmoid-dominated structures, generating turbulent environments capable of producing intermittent energy release (McLaughlin et al., 2018; Schrijver, 2009).

In this context, coronal loops may behave not only as resonant cavities for MHD waves but also as nonlinear systems supporting turbulent cascades and intermittent dissipation processes. Such dynamics may contribute directly to the observed multiscale variability in flare emission.

1.4 Magnetic Reconnection and Solar Flares

1.4.1 The Energy Release Problem

One of the central problems in solar flare physics concerns the rapid release of stored magnetic energy. Classical magnetic diffusion alone cannot explain the observed timescales of flares (Shibata & Magara, 2011).

The magnetic diffusion timescale is given by:

$$t_{\text{diff}} = \frac{L^2}{\eta}, \tag{1.9}$$

where η is the magnetic diffusivity.

For coronal conditions, this timescale may exceed 10^{14} s, far larger than the observed duration of solar flares (Shibata & Magara, 2011). Consequently, flare energy release requires processes capable of violating the ideal frozen-in condition and enabling rapid magnetic field reconfiguration.

1.4.2 Magnetic Reconnection

Magnetic reconnection provides the primary mechanism through which magnetic energy may be rapidly converted into plasma heating, kinetic energy, and non-thermal particle acceleration (Fletcher, 2024; Shibata & Magara, 2011). During reconnection, magnetic field lines of opposite polarity are brought together within narrow current sheets where magnetic topology changes occur. The resulting conversion of magnetic energy powers flare emission and plasma acceleration.

The standard CSHKP flare model (Carmichael, Sturrock, Hirayama, Kopp, and Pneuman) describes flare evolution through the eruption of magnetic flux ropes and the formation of reconnecting current sheets beneath erupting structures (Shibata & Magara, 2011). While the CSHKP model provides a robust phenomenological framework, the actual three-dimensional reconnection region is highly dynamic, often fragmenting into a hierarchy of plasmoids and turbulent structures (McLaughlin et al., 2018; Schrijver, 2009). Within this framework, reconnection produces:

- heating of coronal plasma,
- acceleration of non-thermal particles,
- formation of post-flare loop arcades,
- high-speed plasma outflows.

The primary mechanism for producing hard X-ray emission in solar flares is non-thermal bremsstrahlung, in which accelerated electrons interact with ambient ions and emit photons through Coulomb collisions. The bremsstrahlung spectrum from a power-law distribution of electrons with spectral index δ produces a photon spectrum following $I(E) \propto E^{-\gamma}$, where the photon spectral index γ is related to the electron spectral index by $\gamma = \delta + 1$ for a thick-target model (Brown, 1971; Kontar et al., 2011). The observed

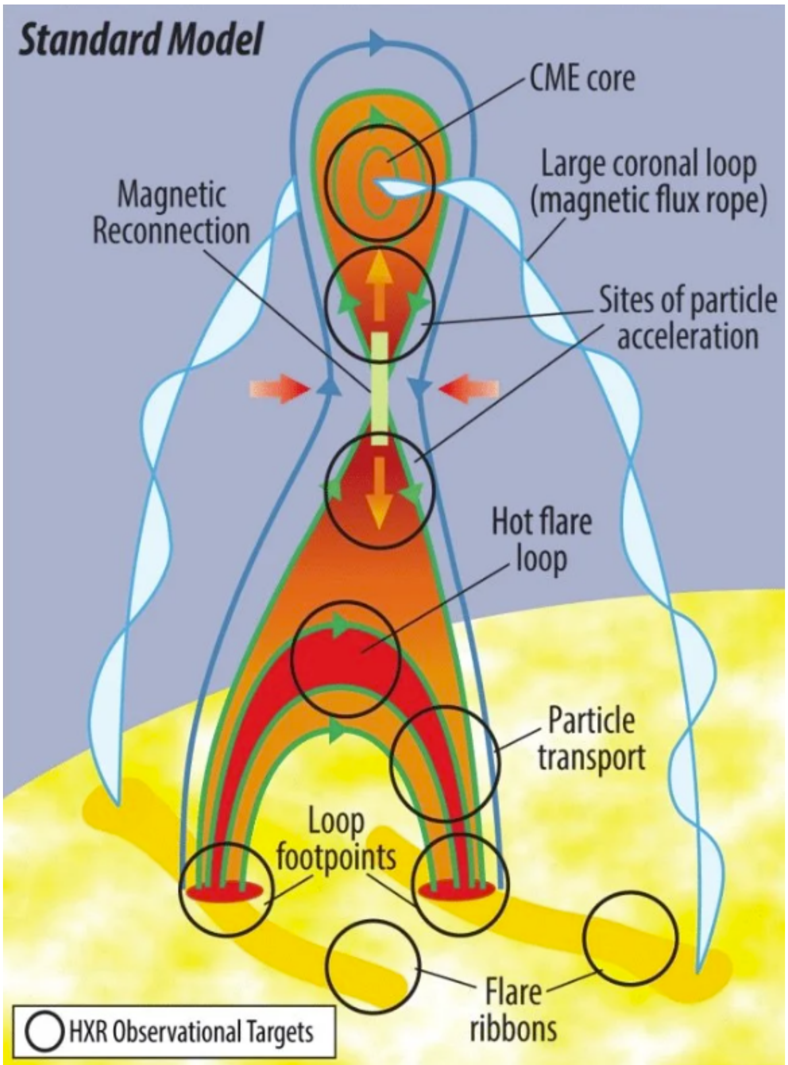

Figure 1.4: CSHKP model for solar flares that explains their observable features on the basis of magnetic reconnection. Circles mark the emission from all key points. (Adapted from Christe et al. (2017)).

hard X-ray spectrum therefore provides a direct diagnostic of the accelerated electron population and its evolution during the flare impulsive phase. Spectroscopic analysis of bremsstrahlung emission has been essential in constraining particle acceleration mechanisms and energy budgets in solar flares (Brown, 1971; Fletcher, 2024; Holman et al., 2011).High-energy electrons accelerated during reconnection propagate along magnetic field lines toward the chromosphere, where they generate hard X-ray emission through bremsstrahlung interactions (Fletcher, 2024).

1.4.3 Intermittent Reconnection and QPP Generation

Modern reconnection theories increasingly emphasize the fragmented and intermittent nature of reconnecting current sheets. Under sufficiently large Lundquist numbers ($S = \tau_{\rm diff}/\tau_A \gg 10^4$), current sheets may become unstable to tearing instabilities and fragment into multiple plasmoids (Bhattacharjee et al., 2009; Loureiro et al., 2007).

This plasmoid-dominated reconnection regime naturally produces bursty and quasi-periodic energy release episodes. Consequently, intermittent reconnection has emerged as a promising explanation for at least some forms of observed QPP behavior (McLaughlin et al., 2018; Nakariakov & Melnikov, 2009).A comprehensive discussion of the physical mechanisms proposed for QPP generation, including MHD wave oscillations, oscillatory reconnection, and turbulent cascade processes, is presented in Chapter 3.

At the same time, reconnection outflows may excite MHD waves within surrounding coronal loops, producing additional oscillatory signatures. These considerations suggest that flare variability may emerge from the interaction of multiple coupled physical processes rather than from a single isolated mechanism (Van Doorsselaere et al., 2016).

1.5 Solar Drivers of Space Weather

Solar magnetic activity strongly influences the heliospheric environment and constitutes the primary driver of space weather phenomena (Fletcher, 2024). Space weather refers to the variable conditions in the near-Earth space environment driven by solar activity, including plasma temperatures, particle densities and energies, solar wind parameters, and magnetic field orientations (Schrijver, 2009). Understanding these drivers is essential for predicting and mitigating the impacts of space weather on technological systems and human activities.

While the primary focus of this thesis is the study of quasi-periodic pulsations in flare X-ray emission, it is important to situate this work within the broader context of solar activity and its space weather impacts. Flares, CMEs, and the solar wind are all manifestations of the same underlying magnetic energy release processes. Understanding flare dynamics, including the temporal variability encoded in QPPs, provides essential diagnostics of magnetic reconnection and particle acceleration that are fundamental to all forms of solar eruptive activity. Moreover, the accelerated particles and enhanced radiation from flares contribute directly to the space weather environment, affecting Earth's magnetosphere, ionosphere, and upper atmosphere. The following sections briefly summarize these interconnected phenomena to provide the necessary context for the observational requirements of the SEE mission and the interpretation of flare variability.

1.5.1 Solar Flares

Solar flares are the most energetic electromagnetic events in the solar system, releasing up to 10^{32} erg of energy over timescales ranging from minutes to hours. Flares are classified according to their peak soft X-ray flux observed by GOES satellites, with classes A, B, C, M, and X representing increasing orders of magnitude, where each class represents a tenfold increase in flux relative to the preceding class (Shibata & Magara, 2011).

Flares exhibit several distinct phases: a pre-flare phase characterized by small-scale brightenings, filament activation, and line broadening (Fletcher, 2024; Švestka, 1976); an impulsive phase marked by rapid hard X-ray and microwave emission from non-thermal electrons (Holman et al., 2011; Kane & Donnelly, 1971); and a gradual (decay) phase during which soft X-ray emission from hot plasma (10–30 MK) fills post-flare loops (Shibata & Magara, 2011).

- **Pre-flare phase:** Signatures of impending eruption, including small-scale brightenings, filament activation, and line broadening in UV and X-ray spectra, occurring minutes to hours before the main energy release.(Fletcher, 2024)

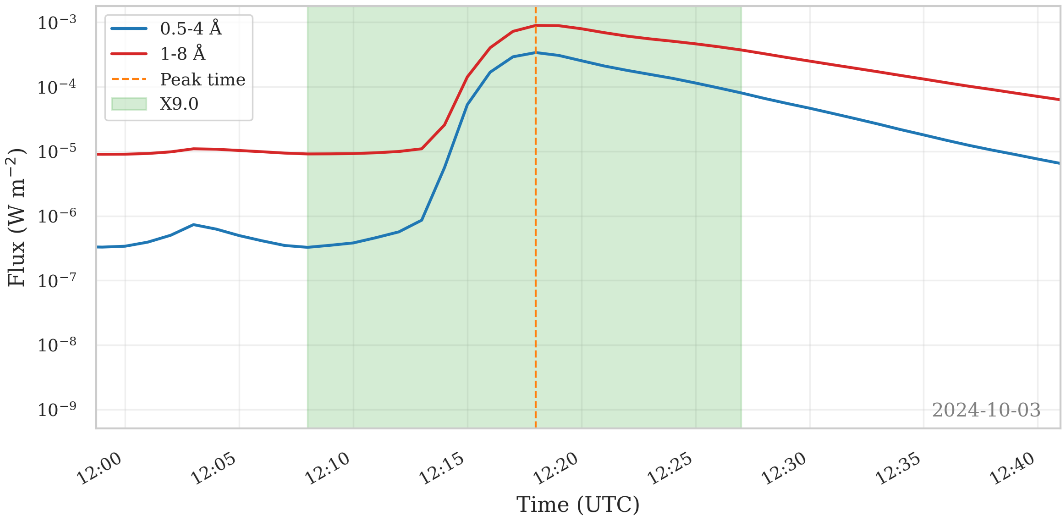

Figure 1.5: The GOES X-ray profile of SOL03102024 which was one of the flares used for the study. The area marked in green from the onset of the flare to the end. The yellow dotted line shows the peak of the flare. Data courtesy of NOAA/NCEI.

- **Impulsive phase:** The main energy release phase, marked by a rapid increase in hard X-ray (HXR) and microwave emission from non-thermal electrons accelerated to energies of tens to hundreds of keV. This phase is highly variable, with characteristic timescales ranging from milliseconds to seconds, and lasts from tens of seconds to tens of minutes.(Fletcher, 2024)

- **Gradual (decay) phase:** Following the impulsive phase, soft X-ray (SXR) emission from hot plasma (10–30 MK) fills post-flare loops and gradually decays over tens of minutes to hours as the plasma cools via radiation and thermal conduction.(Fletcher, 2024).Recent observations have identified an extended late-phase gamma-ray emission phenomenon following the impulsive phase. This emission can persist for tens of minutes to tens of hours and is well-described by pion decay emission from protons accelerated at CME-driven shocks (Share et al., 2018; Woods et al., 2014).

The Neupert effect describes the observed relationship between hard X-ray and soft X-ray emissions: the time derivative of the SXR light curve closely matches the HXR light curve, indicating that non-thermal electrons from the impulsive phase are the primary source of heating for the hot plasma observed in the gradual phase (Neupert, 1968; Shibata & Magara, 2011).

Flares are also associated with the acceleration of particles to very high energies. Non-thermal electrons (tens of keV to tens of MeV) are inferred from their HXR bremsstrahlung and microwave gyrosynchrotron emission. Protons and ions are accelerated to even higher energies (MeV to GeV), producing γ-ray line emission through nuclear de-excitation, neutron capture, and pion decay (Fletcher, 2024). These accelerated particles pose radiation hazards to astronauts and spacecraft systems.

Flares produce intense electromagnetic radiation that can ionize Earth's upper atmosphere, leading to high-frequency (HF) radio blackouts and navigation signal degradation. The Sudden Ionospheric Disturbance (SID) caused by flare X-ray and EUV radiation enhances D-layer ionization, absorbing HF radio waves and disrupting communications, particularly for aviation and maritime operations in polar regions (Fletcher, 2024). The most intense flares can also produce measurable enhancements in the optical continuum (white-light flares), representing energy deposition deep into the photosphere.

The study of quasi-periodic pulsations (QPPs) in flare emission provides a unique diagnostic window into the impulsive phase energy release processes. The rapid temporal variability encoded in QPPs reflects the intermittent and oscillatory nature of magnetic reconnection, particle acceleration, and wave activity in the flaring corona, making them a central focus of this thesis.

1.5.2 Coronal Mass Ejections

Coronal Mass Ejections (CMEs) are large-scale eruptions of magnetized plasma from the Sun into the heliosphere, carrying $10^{15} - 10^{16}$ grams of plasma at speeds of

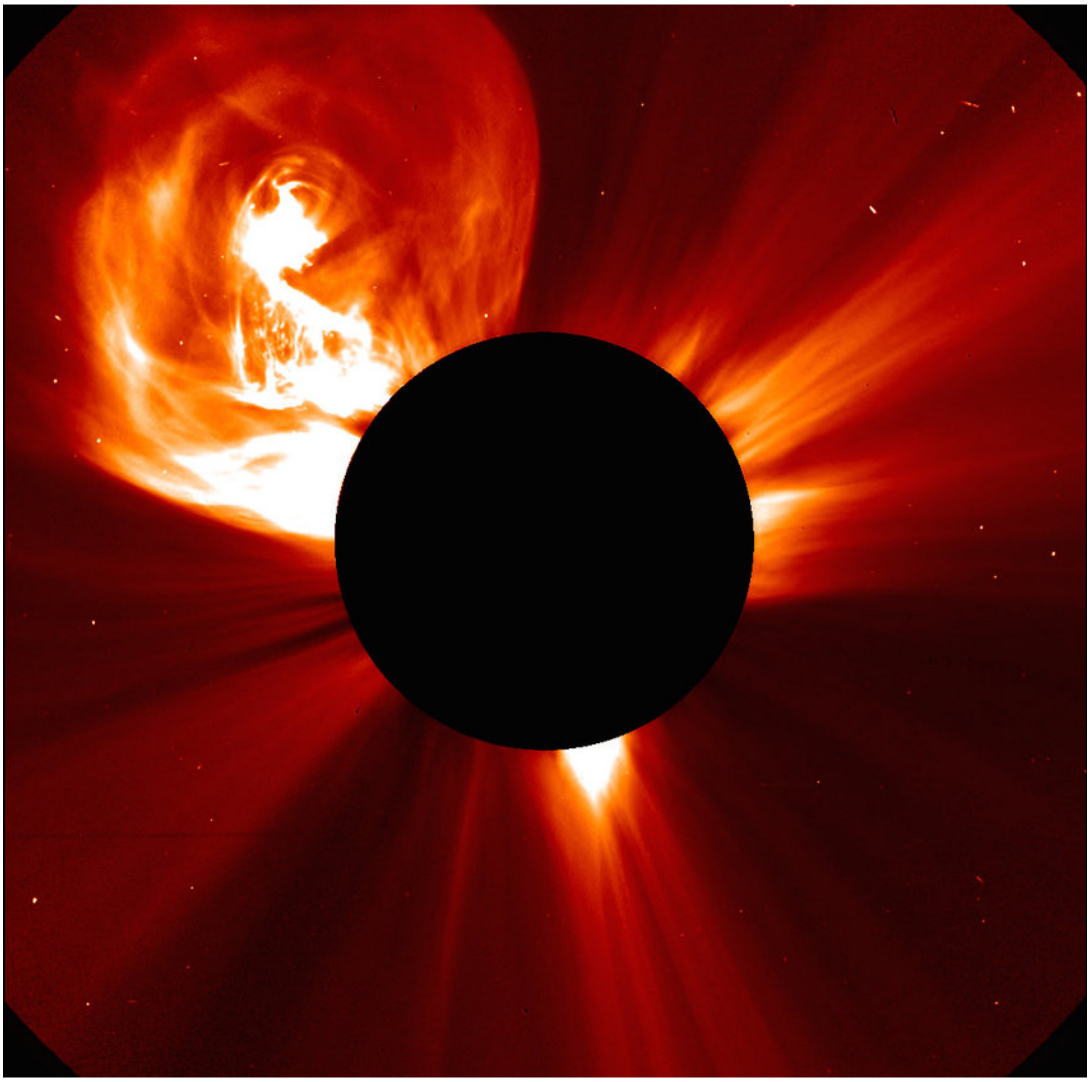

Figure 1.6: A Coronal Mass Ejection event happened on 4th January 2002 imaged by SOHO/LASCO C2 coronagraph.Data courtesy of ESA/NASA

$100 - 2500$ km s^{-1} (Shibata & Magara, 2011).While not all flares produce CMEs, the largest X-class flares are almost always associated with fast CMEs (Yashiro et al., 2006). When directed toward Earth, CMEs can trigger severe geomagnetic storms, impacting power grids, satellite operations, and astronaut safety. The shock front ahead of a fast CME can accelerate particles to high energies, producing Solar Energetic Particle events (Schrijver, 2009).

1.5.3 Solar Wind and Interplanetary Magnetic Field

The solar wind is a continuous, supersonic outflow of plasma from the Sun's corona. At Earth's orbit, the solar wind typically has a speed of $300-800$ km s^{-1} and carries the interplanetary magnetic field (IMF) (Fletcher, 2024). Fast wind streams originate from coronal holes, while slow wind emanates from the streamer belt. The IMF's north-south component (B_z) is particularly important: when B_z is southward, it reconnects with Earth's magnetic field, efficiently transferring energy into the magnetosphere and driving geomagnetic storms (Fletcher, 2024).

1.5.4 Geomagnetic Storms and Space Weather Impacts

Geomagnetic storms are prolonged periods of enhanced magnetospheric activity driven by high-speed solar wind streams or CMEs with sustained southward IMF (Schrijver, 2009). Key impacts include enhanced auroral activity, radiation belt intensification, ionospheric disturbances affecting GPS and communications, and geomagnetically induced currents that can damage power grid transformers. Solar Energetic Particle events pose radiation hazards to astronauts and spacecraft electronics, particularly during polar cap absorption events that disrupt high-latitude communications (Fletcher, 2024; Shibata & Magara, 2011).

Understanding flare dynamics therefore possesses importance not only for fundamental plasma physics but also for predicting and mitigating space weather impacts on technological systems. The study of quasi-periodic pulsations contributes to this understanding by providing diagnostics of the energy release and particle acceleration processes that ultimately drive space weather phenomena.

The physical processes governing flare variability evolve on short temporal scales and often involve highly intermittent high-energy emission (Fletcher, 2024). Observing these processes therefore requires instrumentation capable of high temporal resolution

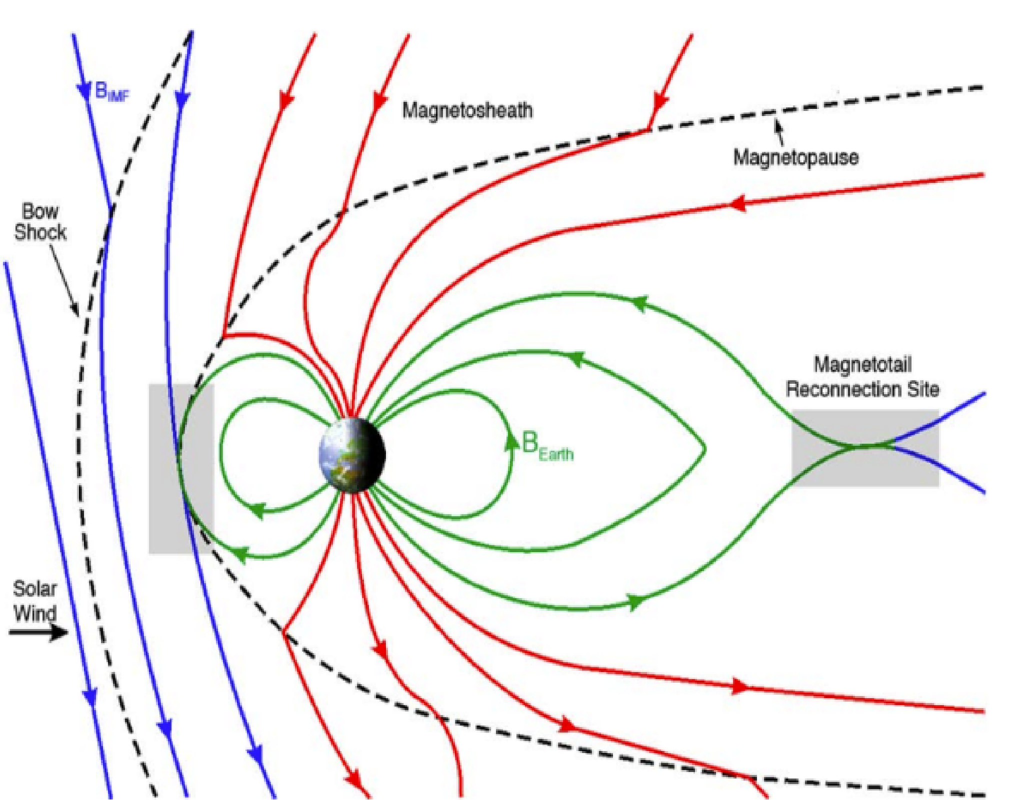

Figure 1.7: A schematic representation of Solar wind and Earth magnetosphere interaction.

and stable high-energy detection. Nanosatellite platforms, with their rapid development cycles and ability to host compact SiPM-based detectors, offer a compelling solution to this observational challenge (Shibata & Magara, 2011).

Traditional large-scale solar observatories have provided major advances in solar physics; however, continuous high-cadence observations remain technologically demanding. Recent advances in nanosatellite platforms and compact detector technologies have significantly expanded observational possibilities.

In particular, Silicon Photomultiplier (SiPM)-based detectors provide compact and highly sensitive systems suitable for high-time-resolution X-ray observations. Such technologies enable lightweight instrumentation capable of investigating rapid flare variability and quasi-periodic pulsations.

The development of nanosatellite-based solar observatories therefore represents an important step toward improving observational access to rapid high-energy solar dynamics.

1.6 Motivation and Scope of This Thesis

Solar flares are a primary manifestation of rapid magnetic energy release in the solar corona, yet the temporal structure of this process remains poorly understood. Observations reveal that flare emission is highly variable, often exhibiting quasi-periodic pulsations (QPPs) over timescales ranging from sub-seconds to minutes. Although significant progress has been made in understanding solar flares, the physical origin of quasi-periodic pulsations remains unresolved. A major challenge arises from the coexistence of multiple physical processes operating simultaneously within flaring regions (McLaughlin et al., 2018; Van Doorsselaere et al., 2016). Distinguishing between these requires analysis techniques capable of handling the nonlinear and non-stationary nature of flare light curves.

This thesis adopts the perspective that observed flare variability may emerge from the coupling between large-scale magnetic structuring and intermittent small-scale energy dissipation processes. Under this interpretation, QPPs may reflect the combined effects of resonant MHD dynamics, oscillatory reconnection, and turbulent dissipation processes occurring within evolving coronal magnetic structures (Nakariakov & Melnikov, 2009; Shibata & Magara, 2011). To investigate these possibilities, this work analyzes high-cadence X-ray observations of solar flares using advanced time-frequency analysis techniques designed to characterize non-stationary and multiscale variability. Empirical Mode Decomposition (EMD) (Huang et al., 1998) is used to extract multiscale oscillatory components from high-time-resolution X-ray observations of X-class flares obtained by STIX onboard Solar Orbiter. The aim is to determine whether the observed variability is consistent with discrete oscillatory modes or broadband, cascade-like behavior.

This study also supports the development of the Sun CubE OnE (SEE) mission by constraining key observational requirements, including temporal resolution and detector sensitivity needed to capture rapid flare variability. By linking observed QPP characteristics to underlying physical processes and instrumental design, this work contributes to both solar flare physics and the optimization of future nanosatellite missions.

The following chapter therefore focuses on the experimental and observational framework of this work, including the instrumentation, detector systems, observational datasets, and flare selection criteria used throughout the analysis.

Chapter 2

The Sun CubE OnE (SEE) Mission and High-Cadence Solar X-Ray Instrumentation

2.1 The Sun CubE OnE (SEE) Mission

The rapid and highly intermittent nature of solar flare energy release places stringent observational requirements on solar instrumentation. As discussed in Chapter 1, quasi-periodic pulsations (QPPs) and short-timescale variability signatures potentially provide important diagnostics of magnetic reconnection, magnetohydrodynamic (MHD) wave dynamics, and turbulent energy dissipation processes occurring within flaring coronal structures. Investigating such phenomena requires observational systems capable of high temporal resolution, stable detector response, and sufficient sensitivity in high-energy X-ray bands (Nakariakov & Melnikov, 2009; Van Doorsselaere et al., 2016).

Recent advances in nanosatellite technologies and compact detector systems have created new opportunities for performing high-cadence solar observations using lightweight and cost-effective platforms (Poghosyan & Golkar, 2017). Within this context, the Sun

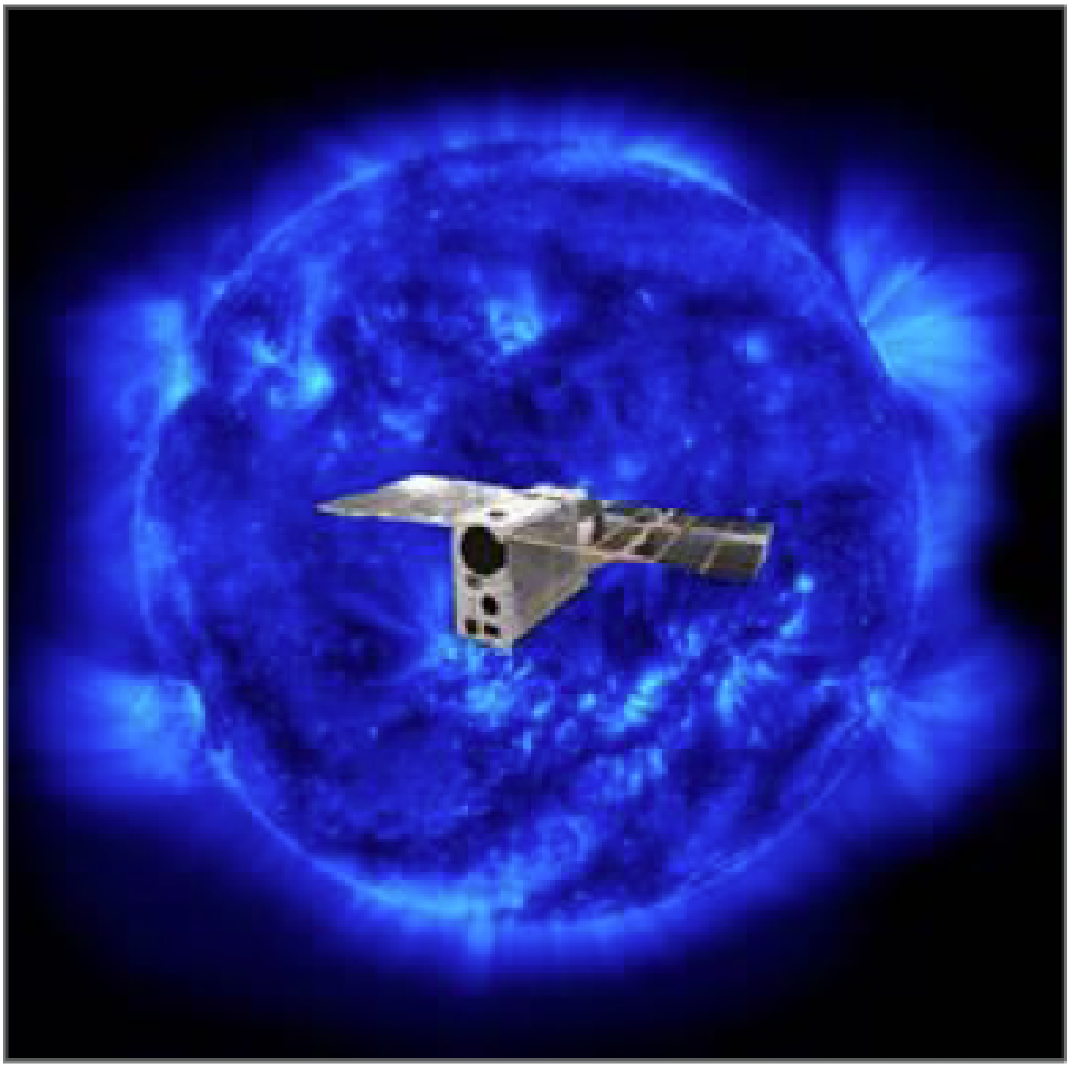

Figure 2.1: Artistic depiction of Sun CubE OnE (SEE) Cubesat

CubE OnE (SEE) mission is a proposed 12U CubeSat mission currently in Phase B study with the Italian Space Agency (ASI), conceived as a nanosatellite-based platform dedicated to the investigation of high-energy solar variability and space weather phenomena (Giovannelli et al., 2023).

The SEE mission combines compact instrumentation with high-time-resolution observational capability in order to investigate the temporal evolution of solar flare emission and contribute to the development of nanosatellite-based high-energy solar instrumentation.

2.1.1 Science Objectives

The primary scientific objective of the SEE mission is the investigation of rapid solar variability in high-energy emission associated with solar flares and eruptive activity. Particular emphasis is placed on observing short-timescale temporal fluctuations that may provide diagnostics of particle acceleration, magnetic reconnection, and quasi-periodic pulsation generation mechanisms.

A major scientific motivation underlying the mission concerns the growing recognition that flare energy release is intrinsically multiscale and highly dynamic (McLaughlin et al., 2018). Observations from previous missions such as RHESSI and STIX have demonstrated that hard X-ray flare emission frequently contains intermittent and oscillatory signatures occurring over timescales ranging from fractions of a second to several minutes (Collier et al., 2023; Ofman & Sui, 2006). However, the physical origin of these temporal structures remains poorly understood.

Several competing models have been proposed to explain the origin of QPPs, including standing MHD wave modes in coronal loops, oscillatory reconnection processes, and intermittent energy release associated with fragmented current sheets and turbulent reconnection (McLaughlin et al., 2018; Shibata & Magara, 2011). Distinguishing between these possibilities requires observational systems capable of resolving rapid temporal variability while maintaining sufficiently stable detector performance.

The SEE mission therefore aims to provide observational capabilities suitable for resolving rapid X-ray variability while simultaneously contributing to the development of compact high-energy instrumentation for nanosatellite applications. In addition to its scientific objectives, the mission also serves as a technological platform for evaluating detector systems and electronic architectures suitable for future nanosatellite-based solar monitoring missions (Giovannelli et al., 2023).

Figure 2.2: Argotec HAWK platform

2.1.2 Spacecraft Platform

The spacecraft architecture of the SEE mission was designed to support stable operation of compact high-energy instrumentation under the mass, power, and thermal constraints associated with nanosatellite platforms (Poghosyan & Golkar, 2017).

SEE is based on a 12U CubeSat bus (Argotec HAWK platform) customized for Earth observation missions. The selected bus provides all standard subsystems: structure, ADCS, OBC/DH, EPS, etc., capable of supporting high-bandwidth science payloads. The Argotec HAWK 12U is a modular design, roughly $20 \times 23 \times 30$ cm, able to host up to ~ 24 kg of total mass (including payload). In SEE's design, the bus supports spacecraft power from body-mounted solar panels, a downlink via S-band (for data) and UHF (for housekeeping), and a high-rate onboard computer with FPGA for data handling. Notably, SEE will operate in a sun-pointing mode most of the time to continuously view the Sun. This imposes requirements on ADCS and thermal design (e.g., pointing stability, radiative balance) that the HAWK platform is sized to meet.

A key aspect of the platform/payload interplay is accommodation: the 12U volume is partitioned into three 4U "slices." Preliminary design suggests using ~ 4U for the UV telescope and ~ 4U for the gamma/X-ray detectors, leaving ~ 4U for electronics, power, and spacecraft bus components. The Argotec HAWK platform, in its 12U form, has ample room for additional actuators or antenna if needed. The Argotec HAWK platform has flown on multiple successful missions, including the LICIACube mission (part of NASA's DART mission) and the ArgoMoon mission, both of which demonstrated the platform's reliability for deep-space operations. For LEO applications, the HAWK bus has been used for Earth observation and technology demonstration missions, with several currently operational on-orbit missions validating its pointing stability, thermal control, and data handling capabilities.

By using a standard CubeSat structure, SEE leverages established launch opportunities and interfaces. The bus avionics and ADCS have modest power ($\sim$ 20–30 W) requirements in operation, well within what 12U of solar panels can supply. The data system must handle real-time high-rate data (10 kHz photon counting), but interim storage and compression will ensure only flare events (or summary spectra) are downlinked, fitting within the S-band bandwidth budget.

Particular attention was given to thermal stability and power management because variations in detector temperature and electronic stability may significantly affect detector response during high-cadence observations. Thermal fluctuations are especially important for semiconductor-based detectors such as Silicon Photomultipliers (SiPMs), whose gain characteristics depend strongly on operating temperature (Garutti, 2022).

2.1.3 Scientific Payload

SEE's science payload consists of two major instruments: a UV imager and a Gamma/ X-ray spectrometer.

UV Imager

The UV telescope is an achromatic, all-reflective design optimized at 280 nm (Mg II band). According to preliminary optics work, it uses two concentric spherical mirrors

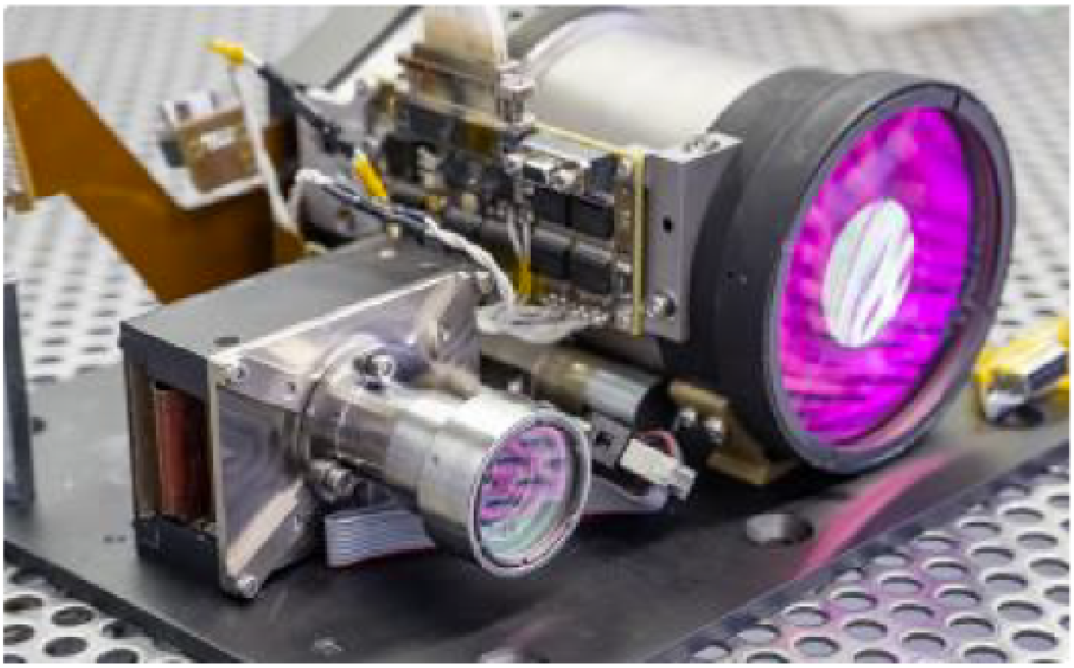

Figure 2.3: SEE UV payload

and three spherical lens elements, with an aperture of 90 mm. This configuration yields a full-disk field-of-view ($\sim 1.1°$) and F/7.6 optics (focal length $\sim$ 690 mm) as shown in Fig. 2.3. The telescope is coated and baffled for UV, and includes a narrow-band Mg II filter. Its compact design occupies $<$ 2U of volume. With a $\sim 1024 \times 1024$ CMOS UV-sensitive detector (baseline), the imager will take full-disk pictures at cadences of minutes to seconds, and burst-mode captures during flares (triggered by the X-ray detector). This instrument heritage comes from prior CubeSat and ISS UV payloads, ensuring technology readiness. Key characteristics (wavelength, MTF, field curvature) meet the science requirements.

Gamma/X-ray Spectrometer

The high-energy payload is split into two units: a gamma-ray channel and an X-ray channel. Each unit uses 4 identical detector modules arranged in a 2×2 array. Each module comprises a scintillator crystal coupled to Silicon Photomultipliers (SiPMs). In

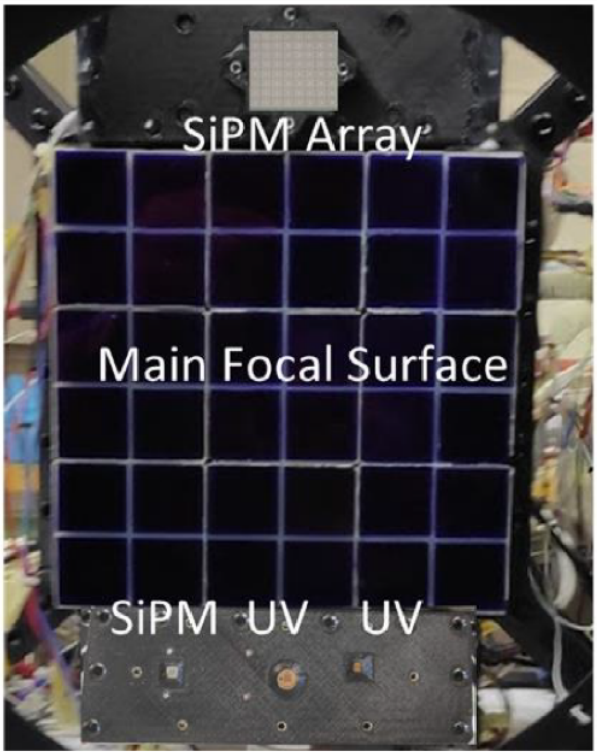

Figure 2.4: Silicon Photomultiplier (SiPM)-Scintillator detector. Schematic of the SiPM-scintillator detector module showing the scintillator crystal coupled to SiPM array.

the gamma channel, a high-Z scintillator (e.g., CsI(Tl) or LYSO) converts MeV photons, while in the X-ray channel a thinner scintillator (or a silicon photodiode) covers ∼keV energies. The readout for both channels is based on Hamamatsu Multi-Pixel Photon Counters (MPPCs, a type of SiPM). Each scintillator has 2–4 SiPMs to read it out (improving light collection uniformity and redundancy). All detectors are surrounded by an anticoincidence shield (plastic scintillator or similar) to reject charged particles and cosmic rays. Anti-Coincidence logic rejects charged particles (cosmic rays), significantly reducing background. While the shield cannot eliminate 100% of charged particle events, it reduces the background count rate by several orders of magnitude, enabling detection of weak flare signals. Residual background can be further subtracted during on-ground data processing using background models derived from quiescent periods. Collimators (tungsten) define the field-of-view to $\sim 6^{\circ}$–8°.

In normal mode, the SiPMs record incoming photons continuously at up to 10 kHz cadence, time-tagging individual photons (10^5–10^6 pulses/s during major flares). The detector electronics digitize pulse amplitudes (proportional to photon energy) via a dedicated ASIC (e.g., IDEAS SIPHRA), enabling on-board spectroscopy in real time. During quiescent times, a lower rate or trigger mode conserves power and data. The combined gamma+X instrument covers the full flare spectrum from ~ 10 keV to several MeV, overlapping the GOES bands and extending above. According to the design, each channel (X, γ) uses a 4-module, two-layer approach: the bottom layer modules have thicker scintillators for higher-energy gammas, while the top layer (X-ray) uses thinner or different scintillators.

Overall the payload mass is within $\sim$ 8–10 kg (4U), and power draw $\sim$ 10–15 W in science mode. Data rates are high (especially during flares), so an FPGA-based payload computer handles real-time histogramming and buffering, compressing data before passing to the bus for downlink. All scientific and housekeeping data are stored in a solid-state recorder for later transmission.

2.1.4 Orbit and Mission Planning

SEE is planned for a Low Earth, Sun-synchronous Orbit (SSO) at $\sim$ 550 km altitude. The orbit is chosen to maximize solar viewing time while ensuring compliance with debris re-entry rules. In analyses, a 550 km SSO with dawn–dusk ascending node (RAAN $\approx$ 06:00 h) was used as baseline. This orbit gives a period of $\sim$ 95.6 min, and minimizes eclipses (typically $\sim$ 20–22 min maxima, $\sim$ 17 min mean), allowing the satellite to keep its solar panels sunlit and point at the Sun almost continuously.

Mission operations assume a nominal 1+1-year timeline (1 year prime + 1 year extension), consistent with typical ASI CubeSat studies. Launch could be as a secondary payload on a Soyuz or Vega-C rideshare. Ground station support (for example, using

Sardinia or Arctic ground stations) would yield multiple daily passes of a few minutes, sufficient for downloading flare event data and housekeeping telemetry. SEE's data policy envisions near-real-time flare alerts: a simple flare "trigger flag" could be sent via low-rate channel immediately upon a large event detection, allowing ground networks to react quickly. Detailed mission planning (see CubeSat proposal Gantt chart) allocates $\sim$ 12 months Phase-A/B and $\sim$ 24–36 months Phase C/D/E including integration and tests. The SSO is a mature orbit (numerous CubeSats use it) and offers stable thermal conditions for the payload's sun-pointing orientation.

The orbital configuration was therefore selected to maximize useful solar observation intervals while maintaining compatibility with spacecraft power and telemetry constraints.

Mission operations also required consideration of telemetry limitations associated with high-cadence observations. Because rapid temporal sampling generates large volumes of observational data, strategies for onboard storage and efficient data transmission formed an important component of mission planning (Poghosyan & Golkar, 2017).

2.2 Instrumentation for Solar Flare Studies on Nanosatellites

The investigation of high-energy solar variability presents significant observational challenges, particularly within the limited mass, power, and telemetry constraints associated with nanosatellite platforms. Nevertheless, recent developments in compact detector technologies have significantly improved the feasibility of performing high-cadence solar X-ray observations using CubeSat-class missions (Garutti, 2022).

2.2.1 Overview of High-Energy Solar Instrumentation

High-energy observations have played a fundamental role in understanding solar flare physics and particle acceleration processes. Missions such as Yohkoh, RHESSI, and more recently STIX onboard Solar Orbiter have provided critical insights into the temporal and spectral evolution of flare emission (Inglis et al., 2011; Krucker et al., 2020).

Hard X-ray observations are particularly important because they provide direct diagnostics of energetic electrons accelerated during magnetic reconnection events. Unlike soft X-ray emission, which is often dominated by thermal plasma processes, hard X-ray emission reflects the behavior of non-thermal particle populations generated during impulsive flare energy release (Fletcher, 2024; Shibata & Magara, 2011).

Observations from RHESSI demonstrated that flare emission frequently contains complex temporal structures including bursts, intermittent fluctuations, and quasi-periodic pulsations (Inglis et al., 2011). Similarly, STIX observations have revealed highly structured hard X-ray variability associated with impulsive flare evolution (Krucker et al., 2020).

These observational advances demonstrated the importance of high-time-resolution X-ray observations for understanding flare dynamics and motivated the development of compact detector systems capable of performing similar measurements on nanosatellite platforms.

2.2.2 Constraints in CubeSat-Based X/Gamma Detectors

The detection of quasi-periodic pulsations imposes stringent constraints on detector performance (Nakariakov & Melnikov, 2009; Van Doorsselaere et al., 2016). Because many oscillatory signatures occur on short timescales and may possess relatively weak amplitudes, detector systems must simultaneously maintain high temporal resolution and adequate signal-to-noise conditions.

However, CubeSat-based instrumentation faces several important limitations including restricted detector volume, limited shielding capability, telemetry constraints, and thermal instability (Poghosyan & Golkar, 2017). Restricted detector size may reduce photon collection efficiency and therefore limit sensitivity to weak high-energy signals. Similarly, limited shielding capability may increase susceptibility to background noise and contamination from energetic particles (Garutti, 2022).

Telemetry limitations also become significant for high-cadence observations because rapid sampling produces large volumes of observational data. Efficient onboard data processing and storage strategies therefore become essential. Thermal stability represents another important challenge. Variations in detector temperature may affect gain stability and noise characteristics, potentially introducing artificial fluctuations into observational data (Garutti, 2022).

Consequently, detector optimization becomes essential for ensuring that observed variability signatures correspond to intrinsic solar processes rather than instrumental artifacts.

2.3 Design and Characterization of the SEE X/Gamma Detector

2.3.1 X/Gamma Detector

The SEE X/Gamma-ray instrument is the core of its flare measurement capability. As outlined earlier, it consists of two sub-instruments (X-ray and Gamma), each with four independent detector modules in a 2×2 configuration. Each module comprises:

- A scintillator crystal (e.g., a 4×4 cm Ce-doped GAGG or CsI block). The gamma modules use thicker crystals (~ 80 mm) to stop MeV photons; the X-ray modules use shorter (~ 40 mm) to optimize response at 10–50 keV.

- An array of SiPMs (Hamamatsu MPPC or similar) coupled to the crystal's output face. Typically 2–4 SiPM tiles are tiled to cover the scintillator, increasing light yield uniformity and redundancy.

- Front-end electronics: the SiPM signals go through a preamplifier/shaper ASIC (e.g., SIPHRA) that digitizes the pulse height (with ~ 0.1 ms time resolution). This yields an energy spectrum per module.

- Collimator and Shield: Each module has a tungsten collimator restricting the field-of-view to $\sim 6°$. Surrounding the scintillator assembly is an anticoincidence scintillator (plastic) read by its own photodiode; coincidence logic rejects charged particles (cosmic rays), reducing background.

All four modules of each channel are read out in parallel. The modules are designed so that any one can fail without losing science . Pre-amplifier gains are calibrated on-ground. The expected energy resolution is $\sim$ 7%–10% at 662 keV (scintillator intrinsic) and $\sim$ 20% at 59 keV, allowing spectral line detection. Lab tests (ongoing) of prototype modules involve illuminating the detector with known LED sources and measuring linearity and resolution. Initial tests show clear photopeaks and good low-energy sensitivity (see Fig. 2.6). Time-tagging of individual pulses demonstrates that the system can handle several kHz count rates without saturation. These bench results validate the module design for flight. The expected detector response function are to be derived from GEANT4 simulations accounting for the scintillator light yield, SiPM quantum efficiency, and electronic gain. Preliminary simulations and total characterization of the detector response is ongoing and will be presented in future publications.

2.3.2 Readout Electronics and Data Processing

The design of the readout electronics was strongly influenced by the temporal requirements associated with flare variability studies.

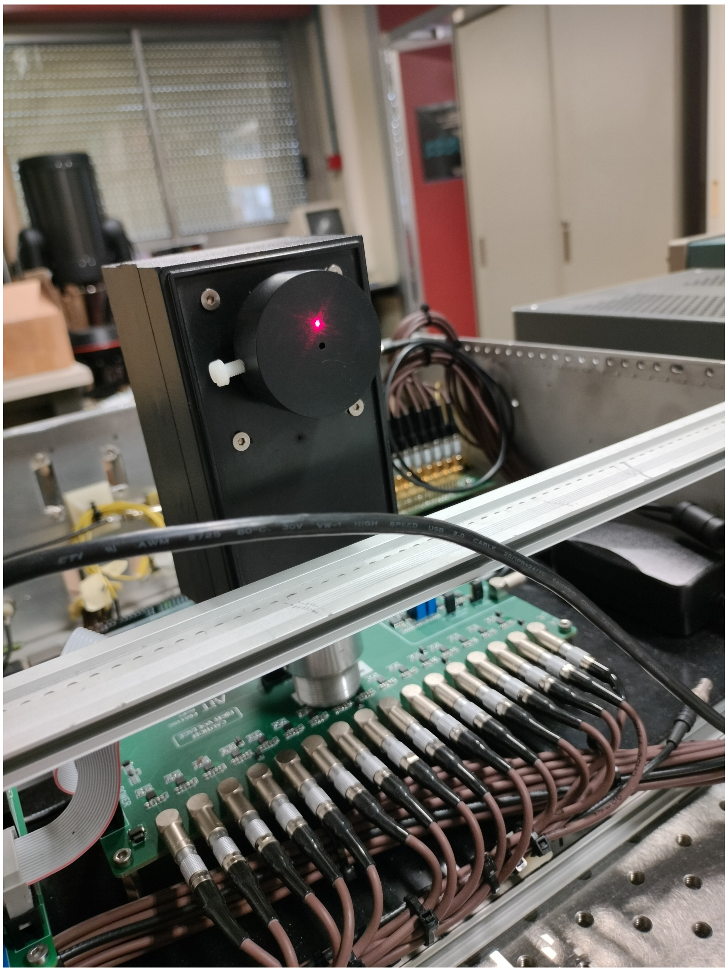

Figure 2.5: Testing of 4x4 pixel SiPM in the Solar Physics Lab of University of Rome Tor Vergata

Because rapid fluctuations in photon flux must be resolved without significant distortion, the electronic processing chain will be optimized to minimize dead time and preserve timing accuracy (Zhang et al., 1995). Dead time represents a particularly important issue in high-count-rate solar observations. During intense flare emission, detector systems may temporarily become unable to register additional incoming photons immediately following previous detection events. If not properly controlled, dead-time effects may distort observed temporal variability and suppress rapid fluctuations in reconstructed light curves (Zhang et al., 1995).

Signal processing procedures are additionally designed to reduce electronic noise

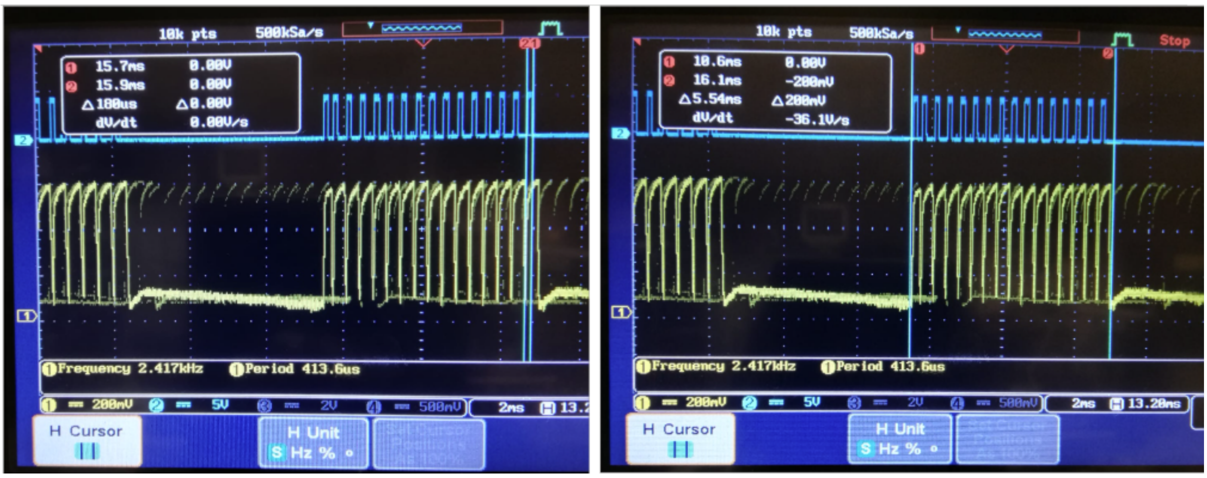

Figure 2.6: Preliminary testing of pulse duration and readout time

contributions that could interfere with temporal analysis techniques applied to flare observations. Data acquisition and pre-processing procedures will be implemented carefully in order to preserve short-timescale variability signatures potentially associated with quasi-periodic pulsations. Particular attention will be given to maintaining temporal continuity in observational sequences because interruptions or inconsistencies in timing may introduce artificial spectral structures during subsequent analysis.

2.4 Observational Motivation and Connection to QPP Studies

The observational and instrumental framework discussed throughout this chapter establishes the experimental foundation necessary for investigating quasi-periodic pulsations in solar flare emission.

The high-cadence observational capabilities enabled by compact X-ray instrumentation now permit increasingly detailed investigation of multiscale temporal variability in flare light curves (McLaughlin et al., 2018).If quasi-periodic pulsations originate primarily from coherent MHD wave modes, one would expect relatively discrete oscillatory signa-

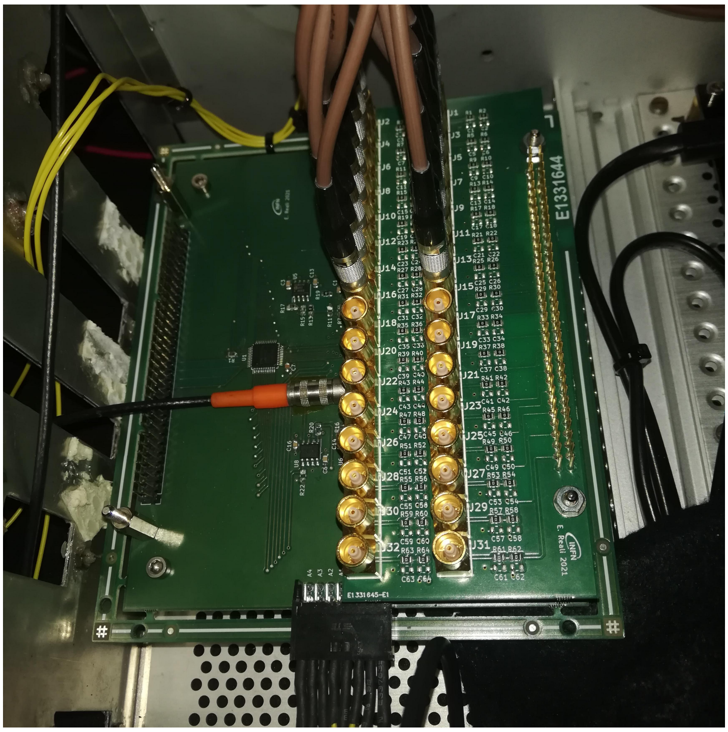

Figure 2.7: Readout Electronics

tures associated with characteristic resonant frequencies determined by coronal magnetic structures (Nakariakov & Melnikov, 2009).

Conversely, if flare variability emerges from fragmented reconnection dynamics and turbulent cascade processes, the resulting temporal behavior may instead exhibit broadband multiscale variability and intermittent oscillatory structures (McLaughlin et al., 2018; Shibata & Magara, 2011).Distinguishing between these competing interpretations requires observational systems capable of resolving rapid temporal variability while maintaining stable detector response and sufficiently high signal-to-noise conditions.

The SEE mission and the detector systems discussed throughout this chapter therefore will provide an important experimental framework for investigating the physical origin of flare variability and quasi-periodic pulsations.

2.5 Chapter Summary

This chapter presented the experimental and observational framework underlying the present thesis.

The scientific motivation and mission objectives of the Sun CubE OnE (SEE) nanosatellite mission were first discussed in the context of investigating rapid solar flare variability and high-energy solar emission. The chapter then examined the observational challenges associated with high-cadence X-ray measurements on nanosatellite platforms, emphasizing the constraints affecting CubeSat-based high-energy instrumentation. Particular emphasis was placed on the design and characterization of the SEE X/Gamma detector system together with the role of Silicon Photomultiplier technologies in compact solar instrumentation. The laboratory detector characterization work performed during this thesis was also discussed as an essential component for ensuring reliable temporal measurements suitable for variability analysis.

Finally, the chapter established the observational motivation for studying quasi-periodic pulsations using high-cadence X-ray observations. Interpreting these observational signatures, however, requires theoretical models capable of connecting observed temporal structures to physical processes occurring within flaring coronal environments. The following chapter therefore examines the principal theoretical models proposed for the generation of quasi-periodic pulsations, with particular emphasis on mechanisms directly testable using high-time-resolution solar X-ray observations.

Chapter 3

Theoretical Models for Quasi-Periodic Pulsations in Solar Flares

3.1 Introduction

As discussed in the previous chapters, solar flares exhibit highly structured temporal variability across multiple wavelength bands, particularly in high-energy X-ray emission associated with impulsive energy release and particle acceleration. Among the most intriguing manifestations of this variability are quasi-periodic pulsations (QPPs), which appear as oscillatory or intermittent intensity modulations spanning timescales from fractions of a second to several minutes (Nakariakov & Melnikov, 2009; Van Doorsselaere et al., 2016).

Despite extensive observational and theoretical investigations, the physical origin of QPPs remains unresolved. One of the principal difficulties arises from the fact that flare emission reflects the interaction of multiple physical processes occurring simultaneously across different spatial and temporal scales. Consequently, several competing theoretical frameworks have been proposed to explain the generation of QPPs (McLaughlin et al., 2018). Some models interpret QPPs as signatures of coherent magnetohydrodynamic (MHD) oscillations occurring within structured coronal loops. Under this interpretation, flare loops behave as resonant cavities capable of supporting standing wave modes whose characteristic frequencies depend on loop geometry, magnetic field strength, and plasma density (Nakariakov & Melnikov, 2009; Roberts et al., 1984).Other models instead attribute QPP generation to intermittent magnetic reconnection processes. In such models, fragmented current sheets and plasmoid instabilities naturally produce bursty and quasi-periodic energy release episodes capable of modulating high-energy flare emission (McLaughlin et al., 2018; Shibata & Magara, 2011).

A third perspective emphasizes the role of turbulence and nonlinear multiscale interactions in reconnecting coronal structures. Under this interpretation, flare variability may emerge from turbulent cascade processes and intermittent dissipation occurring across a broad range of spatial and temporal scales. Reduced magnetohydrodynamic (RMHD) models of coronal loops suggest that resonant structures and turbulent energy transfer may coexist within flaring magnetic systems (Nigro et al., 2008).

Under this framework, quasi-periodic pulsations are treated not exclusively as signatures of ideal standing oscillations, but as manifestations of coupled wave dynamics, fragmented reconnection, and turbulent cascade processes occurring within evolving coronal magnetic structures. The observational capabilities discussed in Chapter 2 now permit increasingly detailed investigation of these competing models using high-cadence X-ray observations. In particular, the combination of SEE-inspired detector concepts and STIX observations provides a framework for investigating whether flare variability is more consistent with coherent oscillatory modes, intermittent reconnection dynamics, or broadband turbulent processes. This chapter therefore examines the principal theoretical models proposed for QPP generation, with particular emphasis on mechanisms directly testable using high-time-resolution X-ray observations. The observational predictions of these competing models are summarized in Table 3.1, which provides a framework for distinguishing between the three theoretical frameworks using high-cadence X-ray observations.

3.2 MHD Oscillations of Coronal Loops

One of the earliest and most widely studied explanations for quasi-periodic pulsations involves magnetohydrodynamic oscillations occurring within structured coronal loops (Nakariakov & Melnikov, 2009; Roberts et al., 1984). Coronal loops represent magnetically confined plasma structures capable of supporting a wide variety of MHD wave modes. Since flare energy release frequently occurs within such magnetic structures, oscillatory processes occurring in loops may directly modulate plasma density, magnetic field strength, and energetic particle transport, thereby producing observable fluctuations in flare emission.

Within this framework, coronal loops behave as resonant cavities whose characteristic oscillation frequencies depend on magnetic field strength, loop geometry, and plasma density (Roberts et al., 1984).

3.2.1 Fundamental MHD Wave Modes

Magnetized plasma environments support several classes of wave modes including slow magnetoacoustic modes, fast magnetoacoustic modes, and Alfvénic modes, each characterized by distinct restoring forces and propagation properties (Roberts et al., 1984).

The characteristic propagation speed of Alfvénic disturbances is given by

$$v_A = \frac{B}{\sqrt{\mu_0 \rho}}, \tag{3.1}$$

where B represents magnetic field strength and ρ the plasma density (Shibata & Magara, 2011).

For typical coronal conditions, Alfvén speeds may reach values of order 10^3 km s^{-1}, producing characteristic oscillation timescales comparable to many observed QPP periods (Nakariakov & Melnikov, 2009).

The standing oscillation frequencies associated with coronal loops may be approximated as

$$\omega_n = \frac{n\pi v_A}{L}, \tag{3.2}$$

where L represents loop length and n the harmonic number. For the fundamental mode $n = 1$, the corresponding oscillation period is $P = 2L/v_A$, which is directly related to the Alfvén transit time (Roberts et al., 1984). This relationship provides a direct connection between observed oscillation periods and coronal loop properties.

3.2.2 Standing Kink Modes

Standing kink modes correspond to transverse oscillations in which the loop axis itself undergoes displacement (Nakariakov et al., 1999). In kink oscillations, the loop structure oscillates collectively while maintaining approximately constant cross-sectional geometry. These modes are weakly compressive and primarily involve transverse displacement of the magnetic structure.

The kink mode phase speed is approximately given by

$$C_k \approx \sqrt{\frac{2B^2}{\mu_0(\rho_i + \rho_e)}}, \tag{3.3}$$

where ρ_i and ρ_e denote internal and external plasma densities respectively (Nakariakov et al., 1999).

Kink oscillations have been widely observed in coronal loops following flare events and are frequently interpreted as standing MHD modes excited by impulsive disturbances (Nakariakov et al., 1999). In the context of QPPs, kink oscillations may modulate energetic particle transport or alter reconnection geometry, thereby producing oscillatory signatures in flare emission (Nakariakov & Melnikov, 2009). However, purely kink-driven models encounter difficulties in explaining strongly bursty and broadband flare variability frequently observed in hard X-ray light curves (McLaughlin et al., 2018).

3.2.3 Standing Sausage Modes

Sausage modes correspond to symmetric radial oscillations involving periodic expansion and contraction of the loop cross-section (Roberts et al., 1984). Unlike kink modes, sausage oscillations are strongly compressive and therefore capable of directly modulating plasma density and magnetic field strength within the loop structure.

Because hard X-ray emission depends strongly on plasma density and energetic particle populations, sausage modes have frequently been proposed as mechanisms capable of producing observable modulation in flare emission intensity (Nakariakov & Melnikov, 2009). The existence of trapped sausage modes depends strongly on loop geometry and density contrast conditions. Only sufficiently thick and dense loops can support trapped sausage oscillations under many coronal conditions (Roberts et al., 1984).

Sausage oscillations are particularly important in flare studies because they may naturally produce modulation of high-energy emission through periodic changes in plasma compression and magnetic trapping efficiency.

3.2.4 Alfvénic Modes

Alfvénic oscillations involve incompressible transverse perturbations propagating along magnetic field lines (Shibata & Magara, 2011). In torsional Alfvén modes, plasma elements undergo azimuthal oscillations around the loop axis without producing strong density perturbations.

Although incompressible modes may not directly modulate emission intensity through density variations, they may influence energetic particle transport and reconnection dynamics indirectly (Nakariakov & Melnikov, 2009). In addition, Alfvénic turbulence has been proposed as an important mechanism for transferring energy across scales within coronal loops (Nigro et al., 2008). Consequently, Alfvénic dynamics may contribute both to coherent oscillatory behavior and to broadband turbulent variability.

3.2.5 Observational Signatures and Predictions

MHD wave models produce several observational predictions that may be tested using high-cadence flare observations (Nakariakov & Melnikov, 2009; Van Doorsselaere et al., 2016). Coherent standing oscillations are generally expected to produce relatively narrow-band periodic signatures with characteristic frequencies determined by loop geometry and plasma conditions. Harmonic relationships between oscillation modes may additionally appear within power spectra (Roberts et al., 1984).

Wave-based models may also predict correlations between oscillation periods and loop lengths estimated from imaging observations (Aschwanden, 2004). However, many flare observations exhibit strongly evolving and intermittent temporal behavior inconsistent with purely stationary oscillatory processes (McLaughlin et al., 2018). This limitation has motivated alternative models involving intermittent reconnection and nonlinear turbulent dynamics.

3.3 Oscillatory Reconnection and Plasmoid Dynamics

An alternative explanation for quasi-periodic pulsations involves intermittent magnetic reconnection occurring within dynamically evolving current sheets (McLaughlin et al., 2018; Shibata & Magara, 2011).

Modern reconnection theories increasingly emphasize that reconnecting current sheets may become highly fragmented and unstable under coronal conditions (Bhattacharjee et al., 2009; Loureiro et al., 2007). Such fragmentation naturally produces bursty and intermittent energy release processes capable of generating quasi-periodic variability in flare emission.

3.3.1 Plasmoid Instability

Under sufficiently large Lundquist numbers, reconnecting current sheets become unstable to tearing instabilities that generate multiple plasmoids within the current sheet structure (Bhattacharjee et al., 2009; Loureiro et al., 2007; Shibata & Magara, 2011).

The Lundquist number is defined as

$$S = \frac{L v_A}{\eta}, \tag{3.4}$$

where L represents characteristic length scale and η the magnetic diffusivity (Priest & Forbes, 2001).

For coronal conditions, Lundquist numbers become extremely large (typically $S \sim 10^{12} - 10^{14}$), allowing rapid growth of plasmoid instabilities (Bhattacharjee et al., 2009). The resulting fragmentation of reconnecting current sheets produces multiple localized reconnection sites and intermittent energy release episodes capable of generating bursty temporal variability consistent with many observed QPP signatures (McLaughlin et al., 2018; Shibata & Magara, 2011).

3.3.2 Plasmoid Coalescence

As plasmoids evolve within reconnecting current sheets, interactions and mergers between neighboring plasmoids may occur (Tajima et al., 1982, 1987).

Plasmoid coalescence releases additional magnetic energy and may generate secondary particle acceleration episodes capable of producing repetitive bursts of high-energy emission (Shibata & Magara, 2011). Such interactions naturally generate intermittent temporal structures that may appear observationally as quasi-periodic intensity modulations in hard X-ray flare light curves (McLaughlin et al., 2018).

3.3.3 Plasmoid-Induced Reconnection

Plasmoid ejection may additionally enhance reconnection rates through feedback processes that increase plasma inflow toward reconnecting regions (Shibata, 1998). Under this interpretation, plasmoid dynamics and reconnection become mutually coupled processes capable of producing oscillatory or intermittent energy release cycles (Shibata & Magara, 2011). Such models naturally explain bursty flare behavior without requiring stable standing oscillations (McLaughlin et al., 2018).

3.3.4 Observational Signatures and Predictions

Reconnection-driven QPP models produce observational signatures significantly different from those expected in purely wave-based models (McLaughlin et al., 2018). Instead of narrow-band stationary oscillations, intermittent reconnection models often predict bursty temporal variability, evolving characteristic timescales, and strong temporal intermittency (Shibata & Magara, 2011). Power spectra associated with reconnection-driven variability may exhibit broadband structure rather than discrete spectral peaks (McLaughlin et al., 2018).

Although reconnection-based models naturally explain intermittent and bursty flare behavior, they often lack the stable periodic structure predicted by standing wave models. Conversely, purely wave-based interpretations encounter difficulties in explaining strongly evolving broadband variability frequently observed in high-energy flare emission (Van Doorsselaere et al., 2016). These limitations suggest that flare variability may emerge from the interaction between coherent magnetic structuring and nonlinear reconnection dynamics rather than from a single isolated process (McLaughlin et al., 2018).

3.4 RMHD Turbulence and Coronal Loop Models

Although wave-based and reconnection-based models explain many aspects of flare variability, neither framework alone fully captures the strongly multiscale nature of flare dynamics (McLaughlin et al., 2018).

An alternative perspective emphasizes the role of turbulence and nonlinear interactions occurring within magnetically structured coronal loops (Biskamp, 2003; Nigro et al., 2008). Within this framework, coronal loops behave as nonlinear dynamical systems capable of supporting both resonant wave behavior and turbulent cascade processes.

3.4.1 RMHD Turbulence Model

Nigro et al. (2008) investigated reduced magnetohydrodynamic turbulence in coronal loops subject to photospheric forcing (Nigro et al., 2008). This work built upon earlier theoretical developments in RMHD turbulence applied to coronal loops (Rappazzo et al., 2008).

In this model, coronal loops behave as resonant cavities in which energy injected at large scales undergoes nonlinear transfer toward smaller scales through turbulent interactions (Nigro et al., 2008).The characteristic resonant timescale of the loop is determined by the Alfvén crossing time

$$t_A = \frac{L}{v_A}. \tag{3.5}$$

Energy injected through boundary forcing excites resonant modes within the loop structure. However, nonlinear interactions between modes simultaneously generate turbulent energy cascades that redistribute energy across scales (Nigro et al., 2008; Rappazzo et al., 2008).

This model is particularly relevant to the present work because it predicts both resonant peaks associated with coherent oscillatory behavior and broadband spectral signatures associated with turbulent energy transfer. The Nigro model therefore provides an important conceptual bridge between coherent oscillatory dynamics and broadband turbulent variability in flare emission.

3.4.2 Turbulent Cascade and QPP Generation

Within turbulent reconnection environments, intermittent dissipation processes may generate burst-like variability across multiple timescales (Biskamp, 2003; McLaughlin et al., 2018). The turbulent energy cascade rate may be approximated using the Kolmogorov phenomenology as

$$\epsilon \sim \frac{v_\ell^3}{\ell}, \tag{3.6}$$

where v_ℓ represents velocity fluctuations at scale ℓ (Biskamp, 2003; Frisch, 1995; Kolmogorov, 1941).

Because turbulence transfers energy across a broad range of scales, the resulting temporal variability may exhibit broadband spectral behavior rather than isolated periodic oscillations (Kolmogorov, 1995). In turbulence-driven systems, power spectral densities frequently exhibit power-law behavior associated with scale-invariant energy transfer processes (Kolmogorov, 1941; Kolmogorov, 1995). Consequently, the spectral slope of flare variability may provide important diagnostics regarding the presence of turbulent cascade dynamics within reconnecting coronal structures (McLaughlin et al., 2018). Under such conditions, spectral distributions may follow scaling relations of the form

$$P(f) \propto f^{-\beta}, \tag{3.7}$$

where β represents the spectral index associated with the underlying cascade process (Biskamp, 2003; Kolmogorov, 1995). If flare variability is dominated by turbulent energy transfer rather than discrete resonant oscillations, one therefore expects broadband spectral distributions characterized by evolving power-law behavior rather than isolated stationary peaks (Nigro et al., 2008).

3.4.3 Spectral Evolution of Flare Emission

Turbulence-based models naturally predict evolving spectral structure in flare observations (McLaughlin et al., 2018). Instead of fixed oscillation frequencies, one expects evolving broadband variability and power-law spectral behavior associated with cascade processes (Rappazzo et al., 2008). Observed spectral slopes may therefore provide diagnostics of changing flare dynamics during different stages of flare evolution (Nigro et al., 2008).

This prediction is particularly important for the present work because both Fourier and Hilbert-Huang analyses provide access to the spectral evolution of flare variability over time.

3.4.4 Observational Signatures

Turbulence-driven models predict observational behavior significantly different from purely coherent wave processes (McLaughlin et al., 2018; Nigro et al., 2008). Instead of stable monochromatic oscillations, one expects broadband power spectra, evolving spectral slopes, intermittent burst-like variability, and multiscale temporal structure associated with nonlinear energy transfer across scales (Biskamp, 2003; Kolmogorov, 1995).

Such signatures are particularly relevant for interpreting flare observations exhibiting strongly non-stationary temporal behavior (Van Doorsselaere et al., 2016).

3.4.5 Testing MHD Wave Models

If flare variability is dominated by coherent MHD oscillations, observational data should exhibit relatively discrete oscillatory signatures associated with characteristic loop resonances (Roberts et al., 1984). One therefore expects relatively stable periodicities, narrow-band spectral peaks, and possible harmonic relationships between oscillation modes (Nakariakov & Melnikov, 2009). Observed oscillation periods may additionally correlate with estimated coronal loop lengths and plasma parameters (Aschwanden, 2004).

3.4.6 Testing Reconnection Models

Reconnection-driven models predict intermittent and bursty temporal behavior associated with fragmented energy release processes (Shibata & Magara, 2011). Under this interpretation, flare observations should exhibit evolving temporal structure and broadband variability rather than stable monochromatic oscillations (McLaughlin et al., 2018). Rapid transitions in oscillatory behavior during flare evolution may additionally indicate reconnection-driven variability (Shibata & Magara, 2011).

3.4.7 Testing Turbulence Models

Turbulence-based models predict multiscale variability and broadband spectral structure associated with nonlinear energy cascades (Biskamp, 2003; Nigro et al., 2008).

In the context of the present work, turbulence models may be investigated through the spectral properties of flare light curves obtained from Fourier and Hilbert-Huang analyses. Specifically, the Hilbert-Huang transform's ability to extract instantaneous frequency distributions allows direct measurement of the spectral slope β and its temporal evolution, providing a key test of turbulent cascade models (Huang et al., 1998). Broadband spectral structure, evolving power-law slopes, and multiscale frequency distributions would favor turbulence-dominated interpretations over purely coherent oscillatory models.

Similarly, temporal evolution of the spectral index during different flare phases may provide insight into changing energy transfer dynamics within reconnecting coronal structures (Nigro et al., 2008). The combination of high-cadence STIX observations and adaptive temporal decomposition techniques therefore provides an opportunity to investigate whether observed flare variability is more consistent with coherent oscillatory modes or broadband turbulent dynamics.

Table 3.1: Observational predictions of competing QPP models

Model	**Temporal Signature**	**Spectral Signature**	**Expected Behavior**
MHD Wave Models	Stable periodic oscillations; possible harmonic structure	Narrow-band spectral peaks	Resonant frequencies linked to loop geometry
Oscillatory Reconnection Models	Bursty and intermittent variability	Broadband evolving spectra	Fragmented reconnection and plasmoid-driven modulation
RMHD Turbulence Models	Multiscale variability and intermittent bursts	Power-law spectra $P(f) \propto f^{-\beta}$	Broadband cascade dynamics with $P(f) \propto f^{-\beta}$ and evolving spectral slopes

Table 3.1 summarizes the principal observational predictions associated with the three theoretical frameworks discussed throughout this chapter. Distinguishing between these signatures using high-cadence X-ray observations constitutes one of the central objectives of the present work.

3.5 Summary

This chapter examined the principal theoretical models proposed for the generation of quasi-periodic pulsations in solar flares. The discussion first considered magnetohydrodynamic wave models involving standing oscillations within coronal loops, including kink, sausage, and Alfvénic modes (Nakariakov & Melnikov, 2009; Roberts et al., 1984). The chapter then examined reconnection-driven models involving plasmoid instability and intermittent magnetic energy release within fragmented current sheets (Bhattacharjee et al., 2009; McLaughlin et al., 2018; Shibata & Magara, 2011).

Finally, turbulence-based models and reduced magnetohydrodynamic loop models were discussed in the context of multiscale flare variability and broadband spectral evolution (Biskamp, 2003; Nigro et al., 2008). Particular emphasis was placed on identifying observational signatures capable of distinguishing between competing physical mechanisms using high-cadence solar X-ray observations (Van Doorsselaere et al., 2016). The following chapter applies these theoretical concepts to the analysis of flare observations in order to investigate whether the observed temporal and spectral properties of solar flare variability are more consistent with coherent oscillatory dynamics, intermittent reconnection processes, or turbulence-driven multiscale energy transfer.

Chapter 4

Results - I

4.1 Empirical Mode Decomposition of Stix X-ray signal

This chapter presents a detailed analysis of quasi-periodic pulsations (QPPs) observed in X-class solar flares using the Empirical Mode Decomposition (EMD) technique applied to high-energy X-ray light curves. Solar flares are among the most energetic phenomena in the heliosphere, characterized by rapid and complex temporal variations in emitted radiation. These variations often exhibit signatures of quasi-periodic behavior, which are believed to arise from magnetohydrodynamic (MHD) processes occurring within magnetically structured plasma in the solar corona. Understanding these oscillatory signatures provides valuable insight into the mechanisms of energy release, transport, and dissipation in flare environments.

The primary objective of this analysis is to identify and characterize QPPs embedded within the flare emission and to investigate their temporal evolution across different phases of the flare. To achieve this, the Hilbert–Huang Transform (HHT), consisting of Empirical Mode Decomposition followed by Hilbert spectral analysis, is employed. This method is particularly well-suited for analyzing solar flare time series, which are inherently nonlinear and non-stationary, and therefore not adequately described by traditional Fourier-based techniques.

The EMD method decomposes the observed X-ray light curves into a finite set of intrinsic mode functions (IMFs), each representing an oscillatory component with locally defined amplitude and frequency. Unlike fixed-basis methods, EMD is adaptive and data-driven, allowing it to capture transient oscillations and frequency drifts that are characteristic of flare dynamics. Each IMF corresponds to a specific temporal scale, thereby enabling a multiscale analysis of the flare emission.

The EMD decomposition was performed using the standard sifting algorithm implemented in the EMD Python package (emd 0.4.0). [1]The sifting process was iterated until the standard deviation between consecutive siftings fell below 0.2, ensuring that each extracted IMF satisfied the two required conditions: (i) the number of extrema and zero-crossings differ by at most one, and (ii) the mean of the upper and lower envelopes is approximately zero. A maximum of 20 IMFs was allowed, though the actual number extracted varied between 7 and 12 depending on the complexity of each flare light curve. Standard EMD was used throughout the analysis. Following the decomposition, the Hilbert transform was applied to each IMF using the normalized Hilbert transform method (emd.spectra.frequency_transform with method='nht'), which computes instantaneous frequency and amplitude from the analytic signal. For Kernel Density Estimation (KDE), we used a Gaussian kernel with bandwidth determined by Scott's rule (Terrell & Scott, 1992), implemented in scipy.stats.gaussian_kde. The KDE was evaluated on a grid of 500 points spanning the full range of instantaneous frequencies for each IMF.

The dataset analyzed in this study consists of five X-class solar flare events observed between 2023 and 2024 by the Spectrometer/Telescope for Imaging X-rays (STIX)

[1] The analysis codes developed for this work will be made publicly available upon publication of the results. Code may also be requested from the author.

Table 4.1: Summary of solar flare events analyzed in this study. STIX light curves were obtained in the 16-28 keV energy band.

Flare Event	Flare class	Date	Flare Time (UT)	Active Region
SOL2023-01-06	X1.2	06 Jan 2023	00:51 – 02:33	AR 13182
SOL2023-03-03	X2.1	03 Mar 2023	17:39 – 18:55	AR 13234
SOL2023-07-02	X1.1	02 Jul 2023	22:53 – 23:58	AR13354
SOL2024-05-11	X5.9	11 May 2024	01:10 – 03:15	AR13664
SOL2024-10-03	X9.0	03 Oct 2024	12:08 – 12:27	AR13842

instrument onboard the Solar Orbiter mission. The STIX instrument provides high temporal resolution X-ray observations in the 16–28 keV energy range, which is particularly sensitive to non-thermal electron populations and energetic processes occurring during flares. The 16–28 keV energy range was selected for this analysis for several reasons. First, this range is sensitive to non-thermal electron populations while maintaining sufficient count rates for temporal analysis. Second, it is above the thermal bremsstrahlung cutoff typically observed in soft X-ray flares, ensuring that the signal is dominated by non-thermal emission. Third, the count rates in this range are high enough to resolve subsecond variability, unlike higher energy bands where photon statistics are limited. The 16–28 keV range also avoids the instrumental background features present at lower energies, providing a cleaner signal for QPP analysis. The selected events span a range of flare magnitudes (X1.1 to X9.0) and originate from different active regions, thereby allowing a comparative investigation of oscillatory behavior across varying magnetic and plasma conditions. While this study focuses on X-class flares to ensure sufficient count statistics, future work will investigate whether M-class flares exhibit similar QPP characteristics. Lower-intensity flares may have lower signal-to-noise ratios, potentially masking weaker oscillatory signatures. However, if QPPs are intrinsic to the flare energy release process, similar frequency bands may be observed in M-class flares with appropriate exposure times.

To provide a comprehensive physical context for the analysis, supplementary ob-

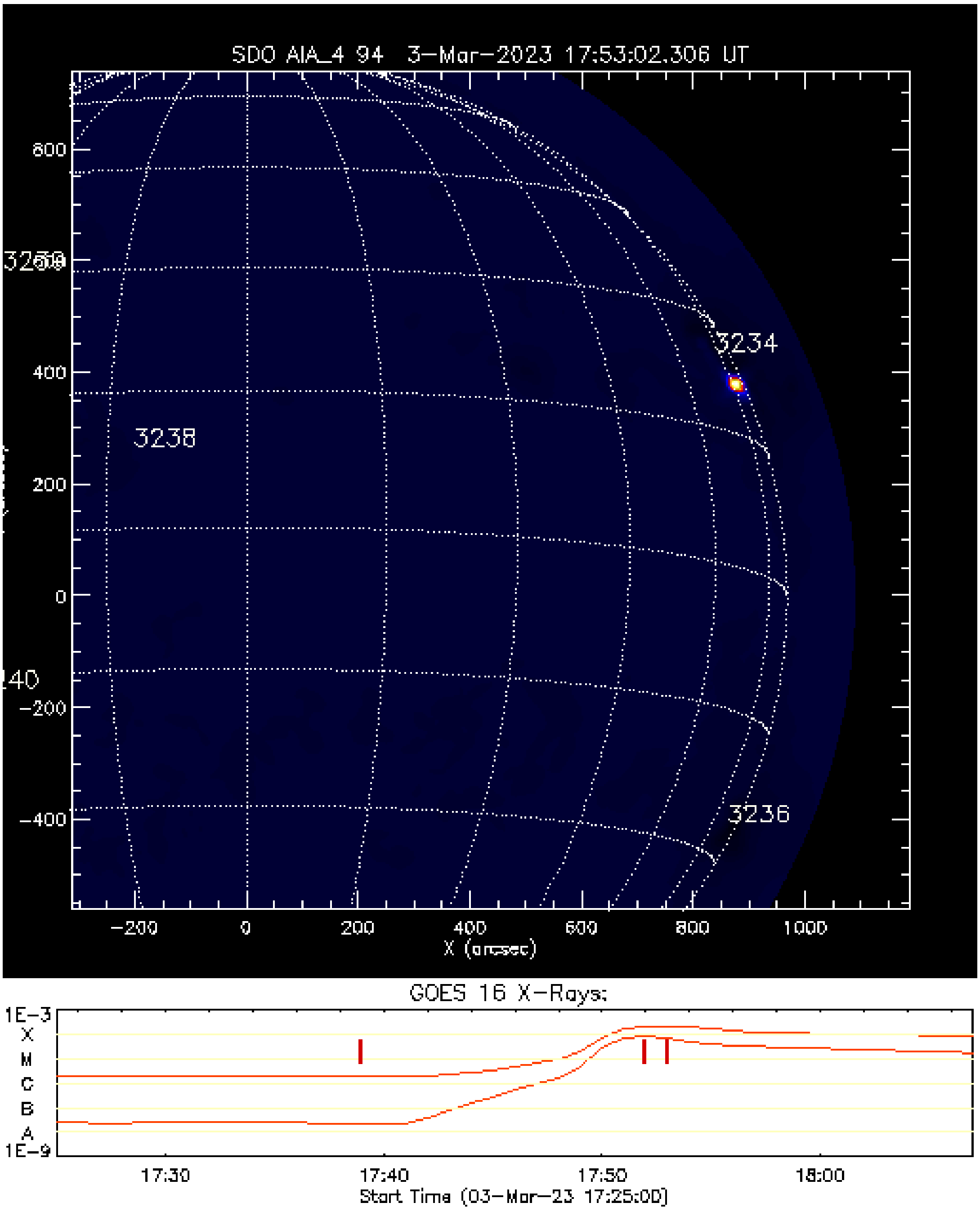

Figure 4.1: The figure on the top shows the Location of the flare SOL03032023 and the below is the GOES X-ray profile of the flare

servations from multiple instruments are incorporated. GOES/XRS data are used to characterize the overall flare evolution and identify distinct flare phases, including pre-flare, impulsive, and decay stages. Imaging data from the Atmospheric Imaging Assembly

(AIA) onboard the Solar Dynamics Observatory (SDO) provide high-resolution observations of coronal loop structures and their temporal evolution. Magnetic field information from SDO/HMI magnetograms is used to infer the magnetic configuration of the active regions, while Extreme Ultraviolet Imager (EUI/FSI) data offer additional constraints on plasma morphology and dynamics. The combination of these datasets enables a more complete interpretation of the oscillatory signatures identified in the STIX light curves.

Table 4.2: Parameters used in the EMD/Hilbert analysis pipeline.

Parameter	**Value**	**Description**
EMD sifting iterations	Adaptive	Standard sifting until IMF criteria met
Sifting stopping criterion	SD = 0.2–0.3	Standard deviation threshold between consecutive siftings
Maximum IMFs	20	Upper limit on number of extracted IMFs
Ensemble EMD	No	Standard EMD (not ensemble) used
KDE bandwidth	Silverman's rule	Automatic bandwidth selection via Scott's rule
Hilbert transform	Standard	Complex analytic signal for instantaneous frequency
Resampling (STIX data)	None	Original 1–4 sec cadence used
Frequency range	1–50 mHz	Range of instantaneous frequencies analyzed
KDE grid points	500	Number of points for KDE evaluation

The analysis proceeds by first decomposing the X-ray light curves into IMFs using EMD. Each IMF is then subjected to Hilbert spectral analysis to compute instantaneous amplitude and frequency, allowing the construction of a time-frequency-energy representation of the signal. This approach makes it possible to track the evolution of oscillatory modes throughout the flare duration and to identify phase-dependent changes in frequency content.

Particular emphasis is placed on comparing the oscillatory characteristics between different stages of the flare. The impulsive phase is typically associated with rapid energy release and strong particle acceleration, while the decay phase is dominated by plasma cooling and magnetic relaxation processes. By examining the variation of instantaneous frequencies and energy distributions across these phases, it is possible to infer the underlying physical mechanisms responsible for the observed QPPs.

In addition to identifying dominant frequencies and corresponding time periods, the analysis also investigates the distribution of oscillatory energy among different IMFs. The temporal evolution of IMF energy provides insight into how energy is partitioned and redistributed among different scales during the flare. This is particularly relevant for understanding whether energy is primarily stored in large-scale structures or cascades toward smaller scales through nonlinear interactions.

The reliability of the EMD-Hilbert analysis pipeline was assessed using synthetic signals with known oscillatory components embedded in a flare-like envelope and correlated noise (Appendix B). The validation demonstrates that the pipeline can recover low- and intermediate-frequency components (6–60 mHz) with typical errors of less than 1 mHz under moderate noise conditions (SNR 24 dB). This provides confidence in the application of the method to the STIX flare observations.

Overall, this chapter aims to establish a comprehensive observational framework for the study of QPPs in solar flares, combining advanced time-frequency analysis techniques with multi-instrument observations. The results obtained provide a foundation for interpreting flare oscillations in terms of magnetohydrodynamic wave processes, coronal loop resonances, and nonlinear energy transfer mechanisms operating in the solar corona.

4.2 Identification of Intrinsic Mode Functions

The STIX X-ray light curves were decomposed into intrinsic mode functions (IMFs) using the EMD algorithm.In EMD, the IMFs are generated through an iterative sifting process: the local maxima and minima of the signal are identified and interpolated

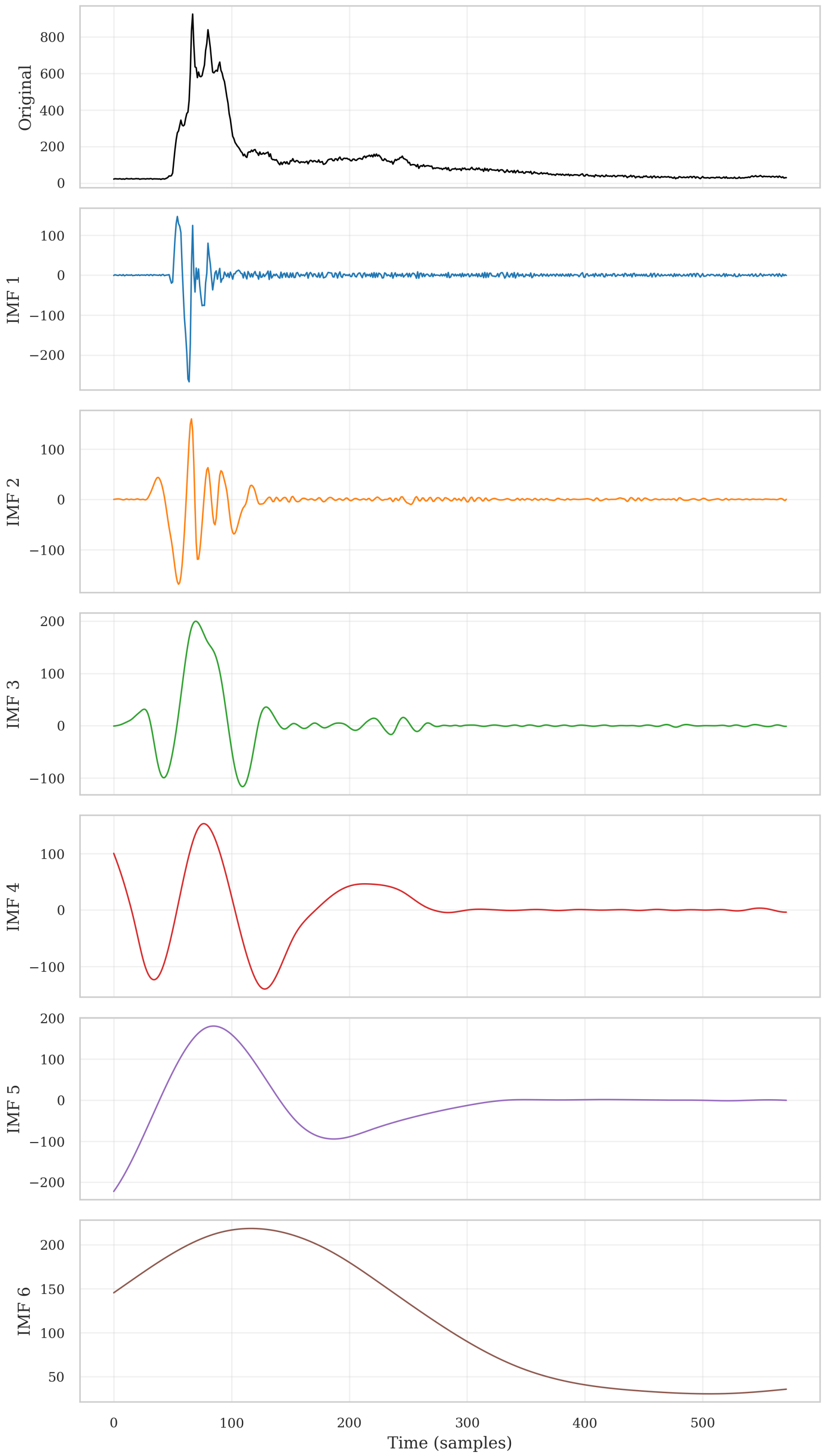

Figure 4.2: The Intrinsic Mode Functions (IMFs) of SOL03032023

to form upper and lower envelopes; the mean of these envelopes is subtracted from the signal, and the process is repeated until a well-behaved oscillatory component (an IMF) is obtained. Each IMF is characterized by two properties: (1) the number of extrema and zero-crossings differ by at most one, and (2) the mean of the envelopes defined by the local maxima and minima is zero. These properties ensure that each IMF represents a purely oscillatory component with physically meaningful instantaneous frequency and amplitude. The IMFs are ordered from high-frequency (IMF1) to low-frequency (IMF8), with the highest-order IMF representing the overall trend.

Lower-order IMFs correspond to high-frequency oscillations, while higher-order IMFs capture long-period variations associated with large-scale processes. This confirms that flare emission is inherently multiscale and cannot be described by a single periodic process.

The extracted IMFs reveal complex temporal variability consistent with quasi-periodic pulsations (QPPs), which are signatures of dynamic plasma processes in coronal loops.

4.3 Instantaneous Frequency Distribution

Following the extraction of intrinsic mode functions (IMFs) through Empirical Mode Decomposition, the Hilbert transform was applied to each IMF to obtain a local time–frequency representation of the signal (Huang et al., 1998). For a given IMF, $c(t)$, the Hilbert transform $\tilde{c}(t)$ is defined as:

$$\tilde{c}(t) = \frac{1}{\pi} \, \text{P.V.} \int_{-\infty}^{\infty} \frac{c(\tau)}{t - \tau} \, d\tau \tag{4.1}$$

where P.V. denotes the Cauchy principal value. The combination of $c(t)$ and $\tilde{c}(t)$ allows the construction of the analytic signal:

$$z(t) = c(t) + i\tilde{c}(t) = A(t)e^{i\phi(t)} \tag{4.2}$$

from which the instantaneous amplitude $A(t)$ and phase $\phi(t)$ are obtained. The instantaneous frequency is then defined as:

$$\omega(t) = \frac{d\phi(t)}{dt} \tag{4.3}$$

This formulation provides a physically meaningful measure of local frequency content, in contrast to traditional Fourier-based approaches where frequency is globally defined and assumes stationarity. The Hilbert-based instantaneous frequency is particularly well-suited for analyzing solar flare light curves, which are inherently nonlinear and non-stationary (Huang et al., 1998).

4.3.1 Characteristics of the Frequency Distribution

The instantaneous frequency distributions derived for the analyzed X-class flares exhibit a broad and continuous spectrum spanning approximately 1–50 mHz. This corresponds to oscillation periods ranging from $\sim$ 20 s to $\sim$ 1000 s, indicating that flare-associated oscillations are distributed across multiple temporal scales.

Unlike discrete spectral peaks typically observed in stationary signals, the frequency distributions obtained here show significant temporal variability, including frequency drifts and intermittent enhancements. This behavior reflects the evolving physical conditions within the flare region, such as changes in plasma density, magnetic field configuration, and energy release rate.

Kernel Density Estimation (KDE) is a non-parametric method for estimating the probability density function of a random variable. KDE applied to the instantaneous frequency distributions reveals that certain frequency bands occur more frequently, indicating the presence of dominant oscillatory modes.In this analysis, KDE is applied to the

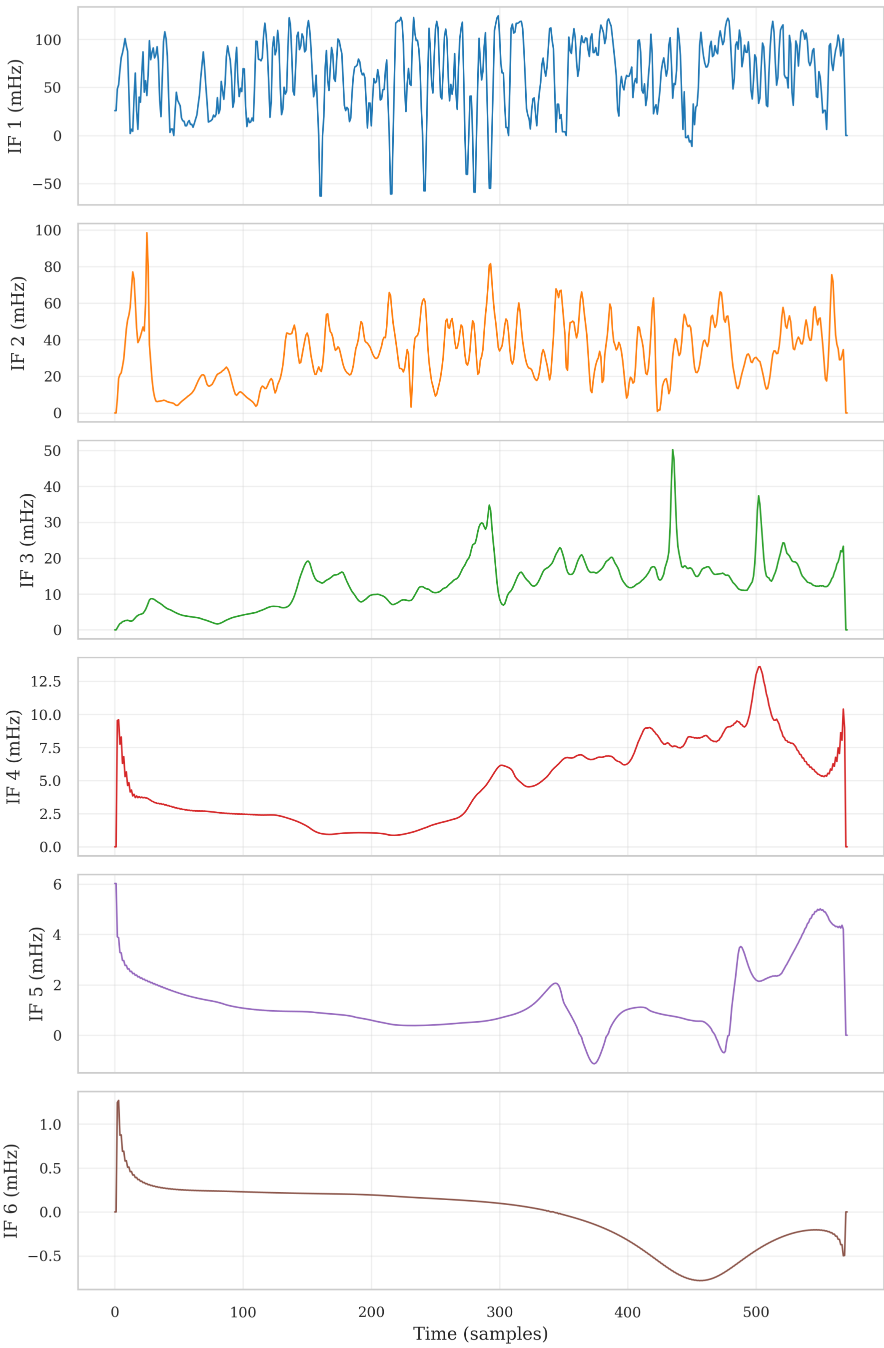

Figure 4.3: The Instantaneous frequency (IFs) of SOL03032023

instantaneous frequency values extracted from each IMF to identify the most probable frequencies present in the signal. The KDE plot 4.5 shows the frequency distribution, where peaks correspond to dominant oscillatory frequencies. The width of each peak indicates the variability of that frequency over time; narrow peaks suggest stable periodic oscillations, while broad peaks indicate evolving frequencies. The y-axis represents the probability density, normalized so that the area under the curve integrates to unity. However, these dominant frequencies are not fixed in time and may shift as the flare evolves, particularly during the transition from the impulsive to the decay phase.

To assess the robustness of the dominant frequency peaks identified from the KDE distributions, we performed a bootstrap resampling analysis. For each flare and each IMF, we resampled the instantaneous frequency values with replacement 500 times, recomputed the KDE for each resampled dataset, and recorded the peak frequency of the resulting distribution. The 2.5th and 97.5th percentiles of the bootstrapped peak frequencies define the 95% confidence interval for each dominant frequency band. The resulting confidence intervals, shown in Tables 4.3 and 4.4, demonstrate that the identified frequency bands are statistically robust, with the width of each interval typically less than 10% of the median peak frequency. The narrow confidence intervals confirm that the KDE peaks are not artifacts of the specific data realization but represent stable features of the flare emission. The bootstrap results are consistent with the synthetic validation (Appendix B), which demonstrated that KDE peaks are statistically stable under resampling even when the true frequency is not perfectly recovered.

4.3.2 Phase-Dependent Frequency Evolution

A systematic difference in frequency characteristics is observed between different phases of the flare. During the impulsive phase, the frequency distribution is generally concentrated within moderate ranges (typically $\sim$4–$\sim$ 30mHz), whereas the decay phase

Table 4.3: Dominant frequency peaks derived from KDE distributions during the impulsive phase of analyzed flares. Values represent median peak frequencies from 500 bootstrap resamples with 95% confidence intervals in parentheses.

Flare Event	**Low (mHz)**	**Mid (mHz)**	**High (mHz)**
SOL2023-07-02 (X1.1)	16.5 (14.2–18.8)	29.1 (27.0–31.3)	60.2 (54.8–65.6)
SOL2023-03-03 (X2.1)	10.1 (8.4–11.8)	21.0 (19.1–23.0)	47.5 (43.5–51.5)
SOL2024-10-03 (X9.0)	11.0 (9.5–12.5)	32.5 (29.6–35.4)	65.1 (60.2–70.0)
SOL2023-01-06 (X1.2)	9.0 (7.6–10.4)	25.0 (22.5–27.5)	55.2 (50.9–59.5)
SOL2024-05-11 (X5.9)	7.5 (6.0–9.0)	40.0 (36.1–43.9)	70.1 (64.3–75.9)

Table 4.4: Dominant frequency peaks derived from KDE distributions during the decay phase of analyzed flares. Values represent median peak frequencies from 500 bootstrap resamples with 95% confidence intervals in parentheses.

Flare Event	**Low (mHz)**	**Mid (mHz)**	**High (mHz)**
SOL2023-07-02 (X1.1)	—	27.5 (25.0–30.0)	72.5 (67.6–77.4)
SOL2023-03-03 (X2.1)	—	35.0 (31.5–38.5)	75.0 (69.5–80.5)
SOL2024-10-03 (X9.0)	20.0 (17.6–22.4)	—	95.0 (88.7–101.3)
SOL2023-01-06 (X1.2)	3.5 (2.5–4.5)	27.5 (24.6–30.4)	70.0 (65.1–74.9)
SOL2024-05-11 (X5.9)	—	22.5 (20.2–24.8)	80.0 (74.1–85.9)

exhibits a broader distribution extending to higher frequencies (up to $\sim$ 50mHz). The conclusions regarding phase-dependent frequency evolution are derived from the KDE distributions shown in Fig. 4.5 and Fig. 4.7. During the impulsive phase (Fig. 4.5), the KDE distribution of IMF2 shows a dominant peak between $\sim$4 and $\sim$ 30 mHz, with minimal power above $\sim$ 30 mHz. In contrast, during the decay phase (Fig. 4.7), the KDE distribution exhibits a broader shape extending to $\sim$ 50 mHz, with a shift in the dominant peak toward higher frequencies. The quantitative peak frequencies are listed in Tables 4.3 and 4.4. This shift from low-to-high frequency dominance across the two phases is a key observational result of this study.

This phase-dependent evolution suggests that the underlying physical mechanisms responsible for the observed oscillations are not stationary. In particular, the increase in high-frequency components during the decay phase indicates the emergence of smaller-scale dynamical processes. This may be associated with the fragmentation of magnetic structures, enhanced turbulence, or repeated small-scale reconnection events within post-flare loops.

In addition, certain events exhibit extremely low-frequency components ($\sim$ 1–5 mHz) during the decay phase, corresponding to long-period oscillations. These may be indicative of global loop oscillations or prolonged magnetic relaxation processes following the main energy release.

4.3.3 Physical Interpretation of Frequency Components

The broad frequency spectrum observed in the instantaneous frequency analysis can be interpreted in terms of magnetohydrodynamic (MHD) processes occurring in the solar corona. In low-β plasma conditions, typical of coronal loops, magnetic forces dominate the dynamics, and oscillations are primarily governed by MHD wave modes (Roberts et al., 1984).

Low-frequency components (1–8 mHz) are generally associated with large-scale structures and global oscillations of coronal loops. These may correspond to standing kink or slow magnetoacoustic modes, whose periods are determined by the loop length and characteristic wave speeds (Nakariakov et al., 1999). The persistence of these low-frequency modes throughout the flare suggests that large-scale magnetic structures continue to influence the dynamics even during the decay phase.

Intermediate frequency ranges (10–20 mHz) are often linked to localized reconnection processes and plasmoid dynamics. These oscillations may arise from periodic or quasi-periodic energy release during magnetic reconnection, leading to modulation of the X-ray emission (McLaughlin et al., 2018; Shibata & Magara, 2011).

High-frequency components (>20 mHz) observed predominantly during the decay phase are likely associated with small-scale processes such as turbulence, shock formation, and fine-scale reconnection within post-flare loops (Biskamp, 2003; Nigro et al., 2008).

These processes can generate rapid fluctuations in plasma parameters, producing short-period oscillations in the observed emission.

4.3.4 Nonlinear Nature of the Frequency Evolution

The observed frequency distributions provide strong evidence for nonlinear dynamics in solar flares. The coexistence of multiple frequency components, along with their temporal variability, suggests that the oscillatory modes are not independent but interact with each other.

Such interactions can lead to energy transfer across scales through nonlinear coupling mechanisms. In magnetized plasmas, this is typically described in terms of wave–wave interactions or turbulent cascades, where energy is transferred from large-scale, low-frequency modes to smaller-scale, high-frequency modes (Kolmogorov, 1941).

The progressive enhancement of higher-frequency components during the decay phase can therefore be interpreted as a manifestation of such nonlinear energy transfer processes. This interpretation is consistent with theoretical models of reduced magnetohydrodynamics, where perpendicular nonlinear interactions drive the cascade of energy toward smaller spatial scales (Nigro et al., 2008).

4.3.5 Implications for Quasi-Periodic Pulsations

The instantaneous frequency analysis provides critical insight into the nature of quasi-periodic pulsations observed in solar flares. Rather than being strictly periodic phenomena, QPPs appear as dynamically evolving oscillatory patterns with time-dependent frequencies.

This challenges the interpretation of QPPs as single-mode oscillations and instead supports a picture in which multiple modes coexist and evolve under changing physical conditions. The ability of the Hilbert–Huang Transform to resolve these temporal variations makes it a particularly powerful tool for studying QPPs in flare emissions.

Overall, the instantaneous frequency distributions reveal that solar flare oscillations are inherently multiscale, nonlinear, and temporally evolving, reflecting the complex interplay of magnetic, plasma, and wave processes in the solar corona.

4.4 Oscillatory Behavior During the Impulsive Phase

The impulsive phase of a solar flare is characterized by a rapid and intense release of magnetic energy, accompanied by strong particle acceleration, plasma heating, and enhanced X-ray emission. The EMD analysis reveals that this phase is dominated by oscillatory components in the frequency range of 4–70 mHz, corresponding to characteristic periods of approximately 14–250 seconds.

These oscillations arise as a direct consequence of the sudden restructuring of the coronal magnetic field during magnetic reconnection. The rapid conversion of magnetic energy into kinetic and thermal energy generates perturbations that propagate through the surrounding plasma in the form of magnetohydrodynamic (MHD) waves. The observed quasi-periodic pulsations (QPPs) can therefore be interpreted as signatures of these wave modes.

In a low-β coronal plasma, where magnetic pressure dominates over thermal pressure, the dynamics are primarily governed by MHD wave modes. The relevant wave speeds are given by:

$$v_A = \frac{B}{\sqrt{\mu_0 \rho}}, \quad c_s = \sqrt{\frac{\gamma k_B T}{m_p}}, \quad v_f = \sqrt{v_A^2 + c_s^2} \tag{4.4}$$

where v_A is the Alfvén speed, c_s is the sound speed, and v_f is the fast magnetoacoustic speed. Under typical coronal conditions, $v_A \gg c_s$, implying that Alfvénic and fast-mode dynamics dominate the evolution of perturbations.

The oscillatory signatures observed in the impulsive phase can be attributed to a combination of:

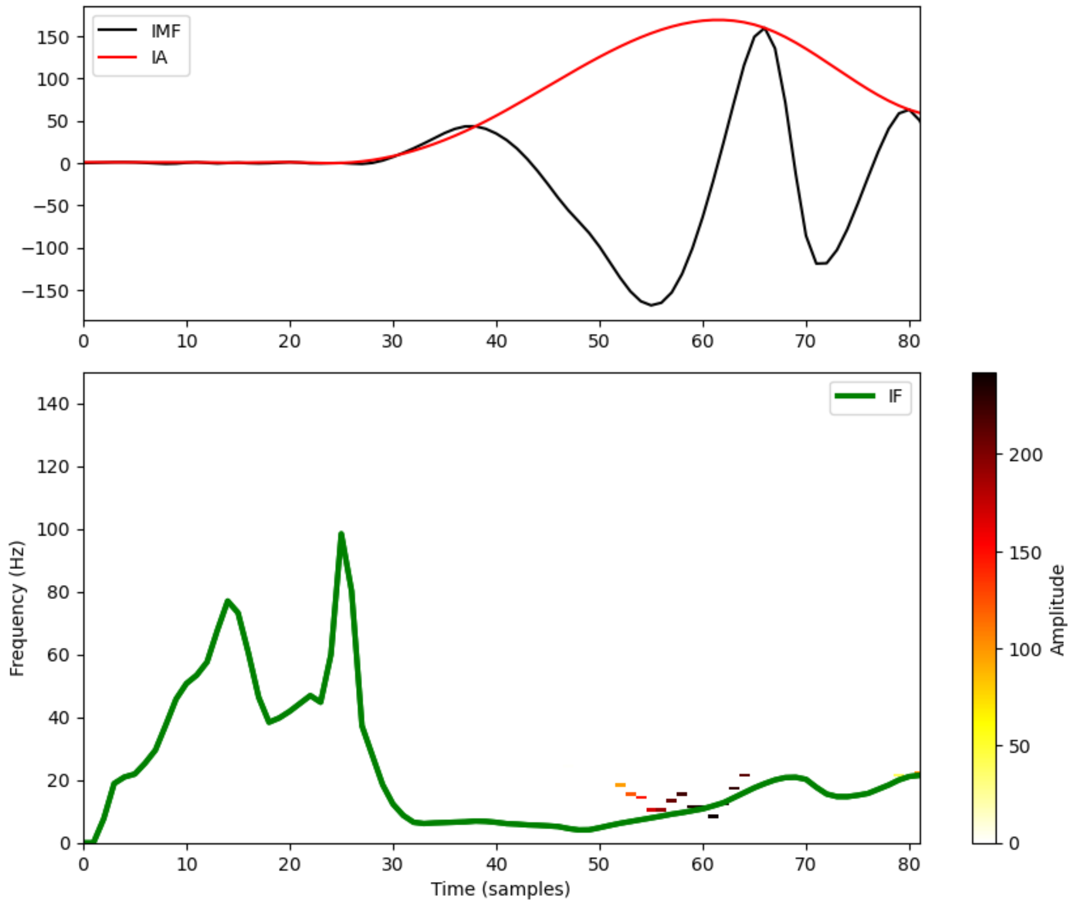

Figure 4.4: Instantaneous frequency profile during the impulsive phase of IMF2 of SOL03032023

- **Standing Alfvén waves:** Generated by reflections at loop footpoints, these waves can form resonant structures within coronal loops, leading to quasi-periodic modulation of plasma parameters.

- **Slow magnetoacoustic waves:** These compressive modes propagate along magnetic field lines and can modulate density and temperature, thereby affecting the emitted X-ray intensity.

- **Fast magnetoacoustic modes:** These waves can propagate across field lines and are capable of producing global oscillations of the loop system.

The characteristic periods observed in the impulsive phase can be related to the

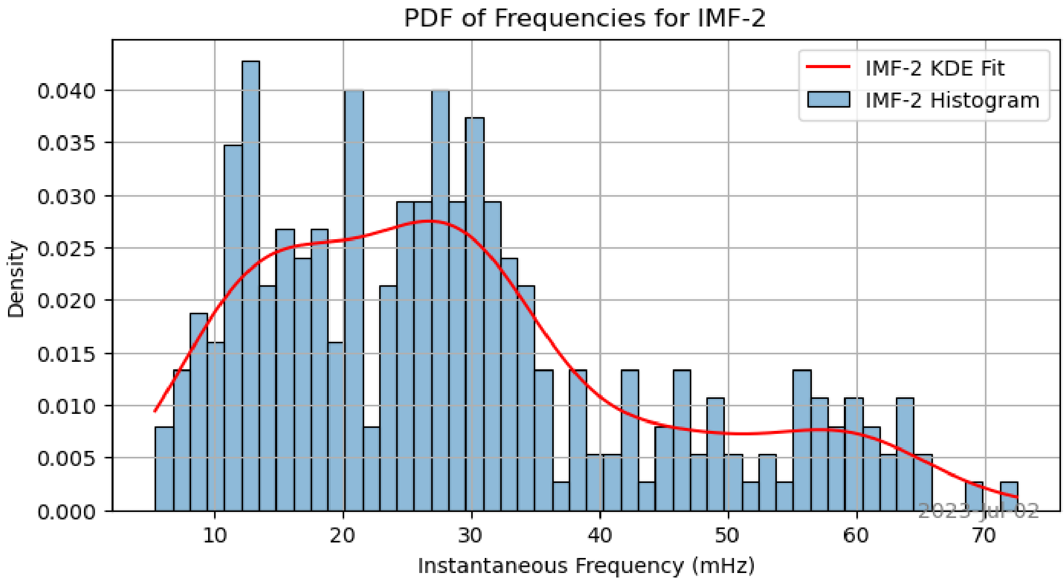

Figure 4.5: KDE fit of the frequency distribution of IMF2 of SOL03032023 during the impulsive phase

fundamental standing modes of coronal loops. For a loop of length L, the fundamental Alfvénic period is given by:

$$P \sim \frac{2L}{v_A} \tag{4.5}$$

For typical coronal loop lengths ($L \sim 10^8$ m) and Alfvén speeds ($v_A \sim 10^3$ km s^{-1}), this yields periods on the order of tens to hundreds of seconds, consistent with the observed frequency range.

In addition to wave excitation, the impulsive phase is characterized by highly intermittent reconnection processes. Plasmoid formation and bursty reconnection can introduce quasi-periodic modulation in energy release, leading to oscillatory signatures in the emitted radiation. These processes can act as drivers for MHD waves, further reinforcing the observed QPPs.

The coexistence of multiple IMFs within this frequency range suggests that the impulsive phase is not governed by a single dominant oscillatory mechanism but rather by the superposition of several wave modes and reconnection-driven processes. This multicomponent behavior reflects the inherently nonlinear and dynamic nature of the flare onset.

Overall, the presence of moderate-frequency oscillations during the impulsive phase indicates that wave processes play a crucial role in the initial redistribution of energy following magnetic reconnection. These oscillations provide important diagnostics of the plasma conditions and magnetic field configuration in the flaring region.

4.5 Long-Period Oscillations and Loop Dynamics

A subset of the analyzed flare events exhibits very low-frequency oscillations in the range of 1–5 mHz, corresponding to long periods of approximately 200–1000 seconds. The presence of such long-period quasi-periodic pulsations (QPPs) is a significant diagnostic of large-scale coronal loop dynamics and provides constraints on the physical properties of the flaring magnetic structures.Long-period oscillations (with periods $>$ 100 s) have been previously reported in solar flares, including the detection of 100–300 s QPPs in the soft X-ray emission of X-class flares (Simoes et al., 2015; Hayes et al., 2020). The present study extends these observations by showing that such long-period components persist throughout both the impulsive and decay phases, suggesting a continuous presence of large-scale loop oscillations. The frequency range of 1–5 mHz identified here is consistent with the fundamental standing modes of coronal loops with lengths of 100–200 Mm, in agreement with the Alfvén transit time scaling (Roberts et al., 1984).

These low-frequency oscillations are most naturally interpreted as signatures of standing magnetohydrodynamic (MHD) modes supported by coronal loops, which act as resonant cavities for wave propagation. The fundamental standing mode period for a loop of length L is given by:

$$P \approx \frac{2L}{C_{\text{ph}}}, \tag{4.6}$$

where C_{ph} is the phase speed of the relevant MHD wave mode. Depending on the dominant restoring force, this phase speed may correspond to the Alfvén speed, sound speed, or fast magnetoacoustic speed.

For typical coronal conditions, the Alfvén speed is given by:

$$v_A = \frac{B}{\sqrt{\mu_0 \rho}}, \tag{4.7}$$

and the sound speed by:

$$c_s = \sqrt{\frac{\gamma k_B T}{m_p}}, \tag{4.8}$$

where B is the magnetic field strength, ρ is the plasma density, T is the temperature, and γ is the adiabatic index.

Using typical coronal parameters ($L \sim 10^8$ m, $v_A \sim 10^3$ km/s), the resulting periods are of the order of several hundred seconds, which is consistent with the observed low-frequency IMFs in the analyzed flare events.

The observed long-period oscillations can therefore be attributed to several candidate MHD modes:

- **Alfvén (torsional or standing) modes**: These are incompressible transverse oscillations that primarily perturb the magnetic field direction. While they do not directly modulate density, they can influence emission through coupling with compressive modes or via line-of-sight effects.

- **Slow magnetoacoustic modes**: These are compressive longitudinal oscillations that propagate along magnetic field lines with speeds comparable to the sound speed. They are efficient at modulating plasma density and temperature, making them strong candidates for producing observable QPPs in X-ray emission.

- **Fast magnetoacoustic (kink) modes**: These involve transverse displacement of the loop axis and can modulate emission through geometric effects and variations in plasma column depth along the line of sight.

Among these, slow-mode oscillations and kink modes are particularly relevant for explaining long-period QPPs, as they can produce observable intensity variations consistent with the modulation seen in X-ray light curves.

The persistence of these low-frequency components during both impulsive and decay phases suggests that large-scale magnetic structures remain dynamically active throughout the flare evolution. These oscillations may be excited impulsively during magnetic reconnection and subsequently evolve as standing modes within the loop system.

Furthermore, the presence of very long-period oscillations (approaching ~ 1000 s in certain events) indicates the involvement of extended loop systems or arcade structures, implying that the energy release process is not confined to a single loop but involves a complex magnetic topology.

In addition to providing information about loop geometry, these oscillations serve as diagnostics for coronal seismology. By combining observed periods with estimates of loop length from imaging data, it is possible to infer magnetic field strengths and plasma densities within the flaring region.

4.6 Oscillatory Behavior During the Decay Phase

A key result of this study is the systematic evolution of oscillatory behavior during the decay phase of the flare. The instantaneous frequency analysis reveals a clear shift toward higher frequencies, with dominant oscillations extending into the range of 3.5–95 mHz, corresponding to periods of approximately 10.5–400 seconds. While previous studies

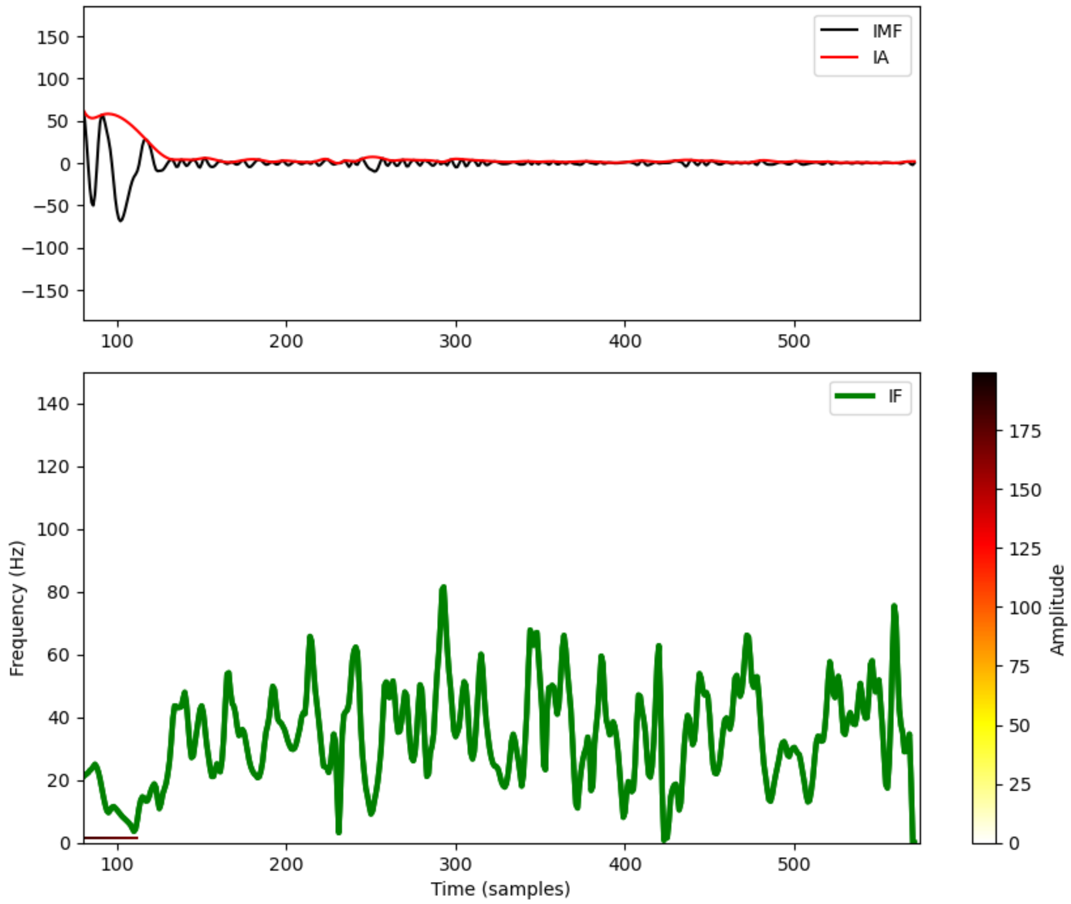

Figure 4.6: Instantaneous frequency profile during the decay phase of IMF2 of SOL03032023

have reported high-frequency QPPs (> 20 mHz) in flare observations (Inglis et al., 2011; Nakariakov & Melnikov, 2009), the systematic shift from lower to higher frequencies from the impulsive to the decay phase has not been quantitatively established. The present study provides the first quantitative evidence for this frequency shift using instantaneous frequency analysis, demonstrating that the transition is robust across multiple flares and is consistent with the development of a turbulent cascade (McLaughlin et al., 2018; Nigro et al., 2008).

This transition from low-frequency to high-frequency dominance reflects a fundamental change in the underlying physical processes governing the flare dynamics. While the impulsive phase is characterized by large-scale energy release and global loop oscillations, the decay phase is dominated by smaller-scale, more localized processes.

The emergence of higher-frequency oscillations can be understood in terms of nonlinear energy transfer mechanisms in a magnetized plasma. In the framework of reduced magnetohydrodynamics (RMHD), the dynamics of strongly magnetized coronal loops are governed by nonlinear interactions between transverse velocity and magnetic field fluctuations. The dominant nonlinear terms can be expressed as:

$$(\mathbf{v}_\perp \cdot \nabla_\perp)\mathbf{v}_\perp, \quad (\mathbf{b}_\perp \cdot \nabla_\perp)\mathbf{v}_\perp, \tag{4.9}$$

which describe the coupling between different spatial scales in the perpendicular direction to the mean magnetic field.

These nonlinear interactions give rise to a turbulent cascade, in which energy injected at large spatial scales is progressively transferred to smaller scales. In spectral terms, this corresponds to an increase in wavenumber $k_\perp$, which is directly associated with higher-frequency oscillations.

The cascade process can also be described in terms of three-wave interactions satisfying the resonance conditions:

$$\mathbf{k}_1 + \mathbf{k}_2 = \mathbf{k}_3, \quad \omega_1 + \omega_2 \approx \omega_3, \tag{4.10}$$

allowing energy transfer between different modes. As energy cascades to smaller scales, it generates higher-frequency fluctuations, consistent with the observed shift in the IMF frequency distributions during the decay phase.

Physically, this process corresponds to the fragmentation of large-scale magnetic structures into smaller, dynamically evolving elements such as current sheets, plasmoids, and turbulent eddies. These structures support rapid oscillations and contribute to the enhanced high-frequency power observed in the decay phase.

The persistence of high-frequency oscillations during this stage also suggests that

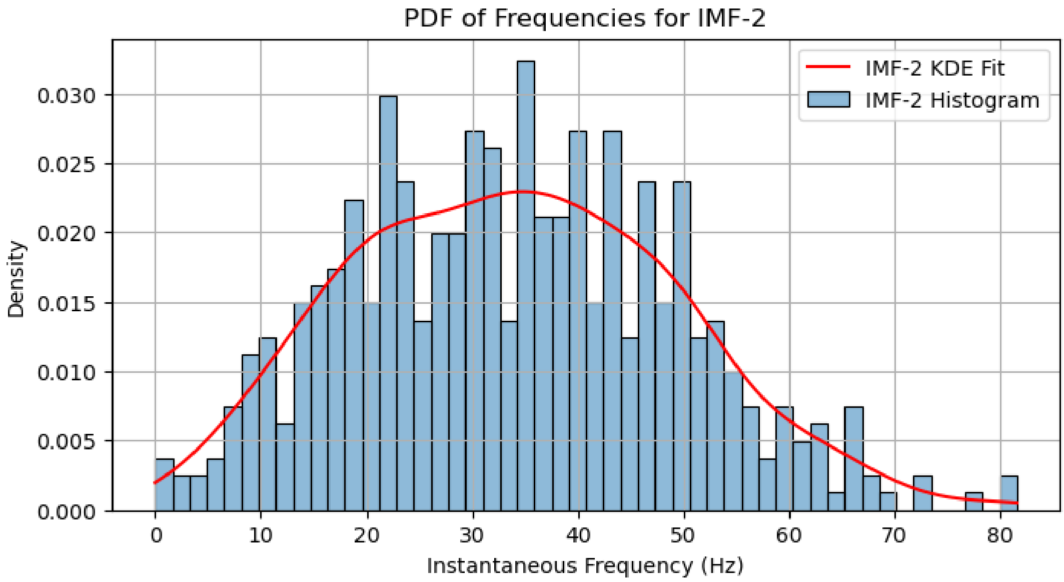

Figure 4.7: KDE fit of the frequency distribution of IMF2 of SOL03032023 during the decay phase.

energy dissipation is not instantaneous but occurs through a prolonged cascade process. This is consistent with the continued presence of energy in the IMF components even after the peak of the flare emission.

An additional contributing mechanism is phase mixing, whereby neighboring magnetic field lines oscillate at slightly different frequencies due to spatial inhomogeneities in plasma parameters. This leads to the development of sharp transverse gradients, enhancing dissipation and generating small-scale structures.

The observed frequency evolution therefore provides strong evidence for a transition from coherent, large-scale oscillatory behavior to a more complex, turbulent regime in the post-flare phase. This transition represents a key aspect of energy transport in solar flares, linking large-scale magnetic energy storage to small-scale dissipation processes responsible for plasma heating and radiation.

In summary, the decay phase is characterized by:

- A shift toward higher-frequency oscillations

- Enhanced small-scale structuring of the plasma
- Nonlinear coupling and turbulent energy cascade
- Continued energy redistribution and dissipation

These observations provide strong support for models in which solar flare evolution involves multiscale interactions governed by nonlinear MHD processes.

4.7 Energy Evolution of Oscillatory Components

The instantaneous energy associated with each intrinsic mode function (IMF) is derived from the Hilbert spectral analysis and is expressed as:

$$E(t) = A^2(t) \tag{4.11}$$

where $A(t)$ represents the instantaneous amplitude of the analytic signal corresponding to a given IMF. This formulation provides a time-resolved measure of the energy content of individual oscillatory modes, enabling the investigation of energy partitioning across different temporal scales.

A key observational result is that peaks in the IMF energy profiles exhibit strong temporal correspondence with enhancements in the X-ray flux. This correlation indicates that the extracted oscillatory modes are not merely mathematical constructs of the decomposition process but are physically meaningful components directly associated with flare energy release. The alignment of IMF energy maxima with flare intensity peaks suggests that these oscillations are either driven by, or actively participate in, the energy release mechanisms during magnetic reconnection. The energy profiles 4.8 show that the amplitude of IMF2 peaks during the impulsive phase and decays gradually during the decay phase. As the flare evolves, the energy shifts from low-frequency IMFs (which decay) to higher-frequency IMFs (which grow or persist), indicating a redistribution of oscillatory

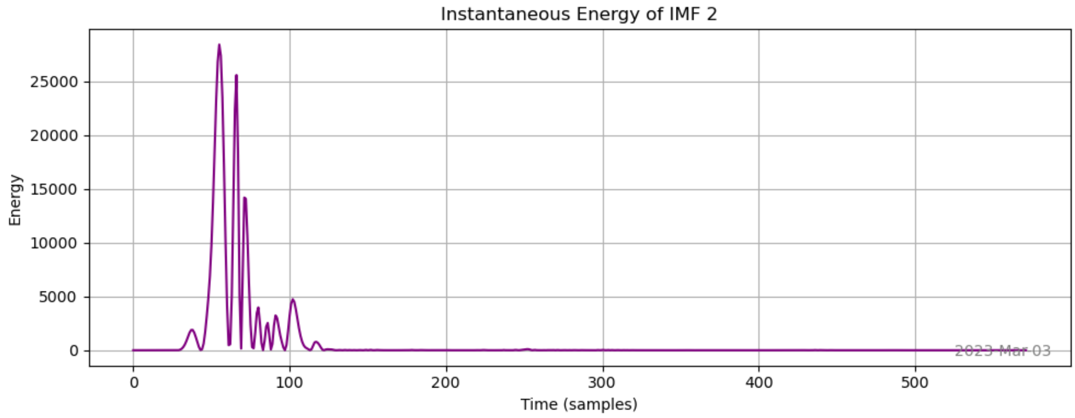

Figure 4.8: Energy profile of IMF2 of SOL03032023

energy from large-scale to small-scale modes. This behavior is consistent with a nonlinear cascade process in which energy injected at large scales transfers to smaller scales without a corresponding increase in total energy, which gradually dissipates through heating and radiation.

From a physical standpoint, the energy evolution of IMFs reflects the redistribution of magnetic energy within the flaring plasma. During the impulsive phase, energy is rapidly injected into the system through reconnection-driven processes, leading to a simultaneous amplification of multiple IMFs across a broad frequency range. This phase is characterized by the presence of both low-frequency (large-scale) and intermediate-frequency oscillatory components, indicating that energy is initially distributed across multiple spatial scales.

As the flare evolves into the decay phase, a systematic redistribution of energy among IMFs is observed. In particular, there is a relative enhancement of higher-frequency modes, accompanied by a gradual attenuation of low-frequency components. This behavior suggests a transfer of energy from large-scale coherent structures to smaller-scale fluctuations.

Within the framework of magnetohydrodynamic turbulence, such behavior can be interpreted as a nonlinear cascade process. In a strongly magnetized, low-β plasma, the dominant nonlinear interactions arise from the coupling between perpendicular velocity and magnetic field fluctuations, described by terms of the form:

$$(\mathbf{v}_\perp \cdot \nabla_\perp)\mathbf{v}_\perp, \quad (\mathbf{b}_\perp \cdot \nabla_\perp)\mathbf{v}_\perp \tag{4.12}$$

These interactions facilitate the transfer of energy across spatial scales without requiring significant compressibility. The increase in high-frequency IMF energy during the decay phase is therefore consistent with a perpendicular turbulent cascade, in which energy injected at large scales is progressively transferred to smaller scales where dissipation becomes efficient.

Furthermore, the persistence of low-frequency IMFs throughout the decay phase suggests the presence of a long-lived energy reservoir associated with large-scale magnetic structures. These components may correspond to standing Alfvénic or magnetoacoustic modes in coronal loops, which act as resonant cavities capable of storing energy over extended timescales.

The coexistence of persistent low-frequency modes and enhanced high-frequency fluctuations indicates that the system does not undergo a simple linear decay. Instead, it exhibits continuous energy exchange between scales, mediated by nonlinear interactions. This dynamic interplay between energy storage and dissipation is a defining characteristic of flare evolution.

In addition, the temporal intermittency observed in the IMF energy profiles points toward bursty energy release processes, potentially associated with fragmented reconnection or plasmoid-mediated energy release. Such intermittency further supports the interpretation of the flare region as a dynamically evolving, weakly turbulent system.

4.8 Multiscale Nature of Flare Dynamics

The results of the EMD and Hilbert spectral analysis clearly demonstrate that solar flare emission is inherently multiscale, involving a broad spectrum of oscillatory components that coexist and evolve throughout the duration of the flare.

At the largest scales, the observed low-frequency oscillations are indicative of global coronal loop dynamics. These include standing magnetohydrodynamic wave modes, such as kink and slow magnetoacoustic oscillations, which are supported by the magnetic structure of the loop. The characteristic timescales of these oscillations are determined by the loop length, magnetic field strength, and plasma density, and typically correspond to frequencies in the range of a few millihertz.

Large-scale magnetic restructuring during the flare, driven by reconnection and magnetic energy release, can excite these global modes. The resulting oscillations can persist over multiple cycles and serve as reservoirs of stored energy, which can subsequently interact with smaller-scale processes.

At smaller scales, the presence of higher-frequency oscillations points to localized and transient phenomena within the flare region. These include:

- **Magnetic reconnection:** The formation and evolution of current sheets can lead to rapid energy release and the generation of oscillatory signatures through repetitive reconnection or plasmoid instability.
- **Turbulence:** Nonlinear interactions between wave modes can produce a cascade of energy to smaller spatial scales, resulting in broadband high-frequency fluctuations.
- **Shock formation:** Fast-mode shocks generated by reconnection outflows or loop contraction can produce short-period oscillations in the plasma.

The simultaneous presence of these processes indicates that flare dynamics cannot be described by a single characteristic scale. Instead, the system exhibits a hierarchical structure in which energy is continuously exchanged between large-scale coherent modes and small-scale dissipative processes.

This multiscale behavior can be understood within the framework of reduced magnetohydrodynamics (RMHD), which describes anisotropic turbulence in strongly magnetized plasmas. In this framework, energy transfer is predominantly perpendicular to the background magnetic field, leading to the development of small-scale structures while maintaining coherence along the field lines.

The observed shift toward higher frequencies during the decay phase provides strong evidence for such a cascade process. As energy is transferred to smaller scales, the corresponding temporal signatures appear as higher-frequency IMFs in the Hilbert spectrum.

Importantly, the multiscale nature of the observed oscillations implies that quasi-periodic pulsations are not generated by a single mechanism. Instead, they likely arise from the superposition of multiple processes operating simultaneously at different scales. This explains the complex and often nonstationary nature of QPP signals observed in solar flare light curves.

Overall, the results highlight the necessity of using adaptive analysis techniques such as EMD and Hilbert spectral analysis, which are capable of resolving nonlinear and nonstationary signals. Traditional Fourier-based methods, which assume stationarity, would not be able to capture the full complexity of the observed multiscale dynamics.

The identification of multiscale oscillatory behavior in solar flares provides important constraints on theoretical models of flare energy release and transport, emphasizing the role of nonlinear interactions and turbulent processes in shaping the temporal evolution of flare emissions.

4.9 Wavelet Analysis and Comparison with Empirical Mode Decomposition

4.9.1 Wavelet Transform Results

Continuous wavelet transform (CWT) with a complex Morlet mother wavelet (wavenumber 6) was applied to the STIX 16–28 keV light curves. The resulting wavelet power spectra (Fig. 4.9) reveal several general trends across the five X-class flares. Significant power above the 95% red-noise level is predominantly confined to periods between approximately 50 s and 200 s, indicating that quasi-periodic pulsations (QPPs) at these timescales are a common feature. The strongest and most persistent wavelet power is observed for the largest flare (X9.0), where a well-defined ridge around 100 s is present. For two of the flares, no statistically significant wavelet power is detected at any period, suggesting an absence of detectable QPPs or insufficient signal-to-noise ratio for the wavelet method. In another flare, the wavelet spectrum exhibits a broad, continuous enhancement extending from about 40 s to 250 s, without resolving multiple distinct periodicities. Overall, wavelet analysis confirms the existence of QPPs in a subset of flares but shows limited ability to separate coexisting periodic components.

4.9.2 Comparison with EMD Results

Table 4.5 summarises the methodological differences between wavelet and empirical mode decomposition (EMD) + Hilbert analysis. The key advantages of EMD for our dataset are: (i) it requires no detrending because the flare envelope is naturally extracted as the highest-order intrinsic mode function (IMF); (ii) it cleanly separates coexisting periods (e.g., the 50 s and 200 s QPPs in one of the flares into distinct IMFs); (iii) it provides instantaneous frequency and amplitude via the Hilbert transform, allowing us to track period drift and amplitude modulation over the flare evolution. Wavelet, on the

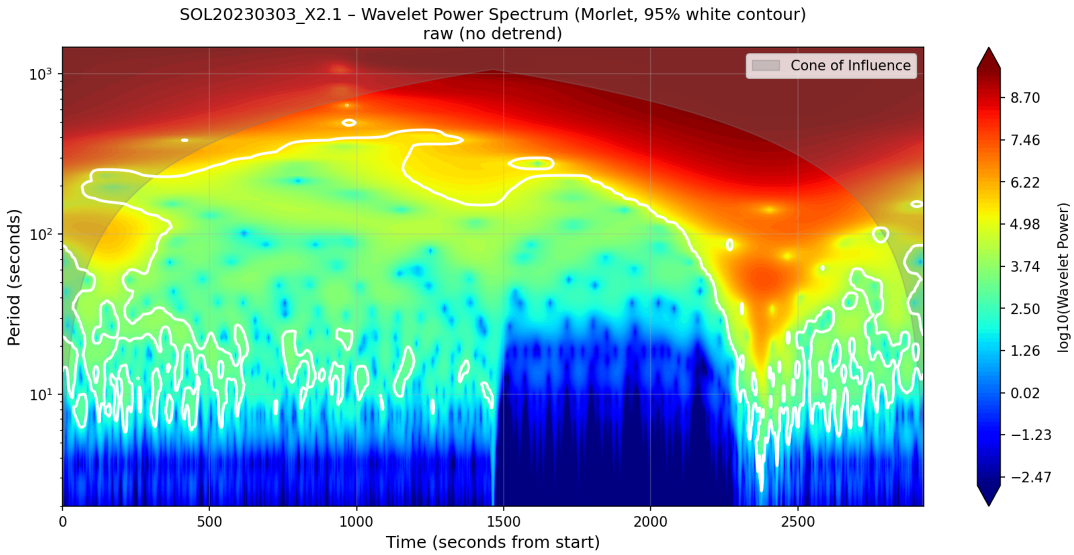

Figure 4.9: Wavelet transform of SOL20230303

other hand, offers a mature statistical significance test (red-noise + cone of influence) and is computationally faster. For the largest flare, the dominant 100 s period is significant in both methods, lending confidence to the EMD result. For the flare with coexisting periods, only EMD is able to separate them, making it the essential tool for studying multi-component QPPs. Consequently, we adopt EMD + Hilbert as the primary analysis method, using wavelet as a validation tool for significance. The multiscale evolution of QPPs presented in the following sections is therefore based on the EMD decomposition.

4.10 Summary of Results

The main findings of this study are:

- All flares exhibit quasi-periodic pulsations across multiple frequency ranges
- Low-frequency oscillations correspond to large-scale loop dynamics
- High-frequency oscillations dominate during the decay phase
- Energy redistribution occurs among oscillatory modes

Table 4.5: Comparison of wavelet (Morlet) and EMD+Hilbert methods for QPP analysis.

Criterion	**Wavelet (Morlet)**	**EMD + Hilbert**
Needs detrending	Yes (otherwise envelope dominates)	No (trend becomes highest IMF)
Separates multiple coexisting periods (e.g., 50 s and 200 s)	Poor (they merge in time–frequency)	Excellent (different IMFs)
Provides instantaneous frequency vs. time	No (only time–frequency map with limited resolution)	Yes (via Hilbert transform)
Quantifies amplitude modulation	Indirect (power colour)	Direct (instantaneous amplitude)
Handles non-stationary frequency drift	Fair (visible as tilted ridge)	Excellent (IMF frequency trace)
Statistical significance testing	Mature (red noise, cone of influence)	Less developed (surrogate tests exist)
Computational speed	Fast	Moderate

- Observations are consistent with nonlinear energy cascade processes

These results highlight the importance of multiscale analysis in understanding solar flare dynamics and demonstrate the effectiveness of the Hilbert–Huang Transform in studying nonlinear plasma processes.

Chapter 5

Results - II

5.1 Multiscale Frequency Structure of QPPs

The instantaneous frequency distributions obtained from the Hilbert–Huang Transform reveal that quasi-periodic pulsations (QPPs) in solar flare light curves exhibit a distinctly multiscale structure. Across all analyzed flare events, the frequency spectra are not continuous or random, but instead show clustering into three characteristic bands:

- Low-frequency band: $f \sim 6$–10 mHz
- Intermediate band: $f \sim 18$–30 mHz
- High-frequency band: $f \sim 45$–70 mHz

These bands are consistently observed across multiple events and phases, indicating that they correspond to physically distinct processes rather than statistical fluctuations. During the impulsive phase, the frequency distributions are characterized by relatively sharp peaks, suggesting the presence of coherent oscillatory modes. These modes likely arise from the excitation of standing magnetohydrodynamic waves within coronal loops.

The persistence of these frequency bands across different flares implies that the underlying mechanisms are robust and intrinsic to flare dynamics, rather than being dependent on specific event conditions. While the results are based on five X-class flares, the consistent appearance of the three frequency bands across events with different magnitudes, active regions, and magnetic configurations suggests that these bands are intrinsic to flare dynamics rather than statistical fluctuations. However, the sample size is limited to X-class flares; future studies with larger datasets, including M-class and C-class flares, are needed to determine whether these bands are universal across all flare classes. The present results should therefore be interpreted as a robust finding for X-class flares, with extrapolation to other flare classes requiring further investigation.

5.2 Alfvén Timescale Constraints and Loop Resonance

The natural timescale for oscillatory processes in magnetized coronal loops is set by the Alfvén transit time. For a loop of length L, the fundamental oscillation period is given by:

$$P_1 = \frac{2L}{v_A} \tag{5.1}$$

where the Alfvén speed is:

$$v_A = \frac{B}{\sqrt{\mu_0 \rho}} \tag{5.2}$$

Using typical parameters for flaring coronal loops, namely $L \sim 50$–200 Mm, $B \sim 50$–150 G, and $n \sim 10^9$–10^{10} cm^{-3}, the resulting Alfvén speed lies in the range $v_A \sim 10^3$–4×10^3 km s^{-1}. This yields characteristic frequencies:

$$f \sim 2\text{–}30 \text{ mHz} \tag{5.3}$$

This range is in excellent agreement with the observed low- and intermediate-frequency bands. The low-frequency component (6–10 mHz) is therefore naturally interpreted as the fundamental mode of standing Alfvénic oscillations in large coronal loops, while the intermediate band (18–30 mHz) corresponds to higher harmonics or oscillations in shorter loop structures. The characteristic frequencies (2–30 mHz) are not always present in the corona; they depend on the loop length and Alfvén speed. However, in flare-active regions where loops are heated and energized, these frequencies are naturally excited by impulsive energy release. The observed low-frequency band (6–10 mHz) corresponds to long loops (100–200 Mm), while the intermediate band (18–30 mHz) corresponds to shorter loops (50–100 Mm) or higher harmonics. These frequencies are not arbitrary; they are determined by the physical parameters of the coronal loops (loop length, magnetic field strength, plasma density) and therefore provide constraints on the flaring magnetic structure.

However, the presence of high-frequency components extending beyond 40 mHz cannot be reconciled with simple linear resonance models, indicating the involvement of additional physical processes.

5.3 Nonlinear Energy Transfer in the RMHD Framework

To explain the emergence of high-frequency oscillations, it is necessary to consider nonlinear interactions within the plasma. In the regime of a strongly magnetized, low-β plasma, the dynamics are well described by Reduced Magnetohydrodynamics (RMHD).

In this framework, the evolution of fluctuations is governed by nonlinear coupling terms:

$$(\mathbf{v}_\perp \cdot \nabla_\perp)\mathbf{v}_\perp, \quad (\mathbf{b}_\perp \cdot \nabla_\perp)\mathbf{v}_\perp \tag{5.4}$$

These terms represent interactions between perpendicular velocity and magnetic field fluctuations, leading to a transfer of energy across spatial scales. Importantly, RMHD predicts that energy cascades primarily in the direction perpendicular to the background magnetic field.

The fundamental mechanism for this transfer is the interaction of counter-propagating Alfvén wave packets. These interactions satisfy resonance conditions of the form:

$$\mathbf{k}_1 + \mathbf{k}_2 = \mathbf{k}_3 \tag{5.5}$$

and result in the generation of smaller-scale structures with higher characteristic frequencies.

5.4 The Nigro et al. (2008) Coronal Loop Model

A comprehensive theoretical framework for this process is provided by the model developed by (Nigro et al., 2008), which describes turbulence in coronal loops using RMHD.

In this model, a coronal loop is treated as a magnetically confined structure with a strong axial field B_0, anchored at the photosphere. The footpoints of the loop are subject to slow, random motions that inject energy into the system. These motions are predominantly low-frequency (effectively DC forcing) and excite large-scale magnetic perturbations within the loop.

A key result of the (Nigro et al., 2008) model is that the injected energy does not dissipate directly. Instead, it accumulates in large-scale magnetic fluctuations, which act as an energy reservoir. These fluctuations correspond to the low-frequency oscillations observed in the present analysis.

As the amplitude of these fluctuations increases, nonlinear interactions become significant. The RMHD nonlinear terms then transfer energy to progressively smaller perpendicular scales, generating a turbulent cascade. This process leads to the formation of current sheets and small-scale structures where dissipation becomes efficient.

The energy spectrum in the perpendicular direction follows a power-law:

$$E(k_\perp) \propto k_\perp^{-5/3} \tag{5.6}$$

which is characteristic of anisotropic MHD turbulence. The nonlinear timescale associated with fluctuations at scale $k_\perp$ is given by:

$$\tau_{nl} \sim \frac{1}{k_\perp \delta v} \tag{5.7}$$

implying that smaller scales correspond to shorter timescales and higher frequencies:

$$f \propto k_\perp \tag{5.8}$$

This establishes a direct connection between the turbulent cascade in physical space and the frequency spectrum observed in the data.

5.5 Spectral Evolution from Impulsive to Decay Phase

A central result of this study is the identification of a clear transition in spectral behavior between the impulsive and decay phases of solar flares.

During the impulsive phase, the frequency spectrum is dominated by discrete peaks corresponding to resonant modes. This indicates that the system is still in a relatively coherent state, with energy concentrated in large-scale structures.

In contrast, the decay phase exhibits a broad, continuous frequency distribution with a pronounced high-frequency tail extending up to ~ 90 mHz. The disappearance of discrete peaks and the emergence of a smooth spectrum are clear signatures of nonlinear interactions and turbulent evolution.

The transition from discrete peaks in the impulsive phase to a broad continuous spectrum in the decay phase is a direct observational result of the present analysis shown in Section 4.6. This transition is consistent with the RMHD turbulence model of (Nigro et al., 2008), which predicts that energy injected at large scales cascades to smaller scales as nonlinear interactions become dominant. The agreement between the observed spectral evolution and the theoretical prediction provides strong support for the interpretation that flare variability is governed by nonlinear energy transfer processes.

5.5.1 Quantitative Spectral Scaling

The decay phase provides a regime in which the frequency spectrum can be approximated by a power-law:

$$E(f) \propto f^{-\beta} \quad (5.9)$$

The spectral index β was estimated by fitting a power-law function $E(f) = Af^{-\beta}$ to the decay-phase frequency distributions using ordinary least-squares regression in log-log space. The fitting was performed over the frequency range 5–80 mHz. This range was selected for two reasons: (i) frequencies below 5 mHz are dominated by residual flare trend effects that persist even after detrending, and (ii) frequencies above 80 mHz are affected by photon counting noise, which becomes significant at the highest frequencies. The chosen range thus maximizes the linear extent of the power-law behavior while avoiding edge effects (Biskamp, 2003).

The fit used ordinary least squares with uniform weighting, as the uncertainties in the KDE estimates were approximately constant in log space. To estimate the uncertainty in β, we performed bootstrap resampling of the instantaneous frequency values (1000 iterations), refitting the power law for each resampled dataset. For each iteration, we resampled the data with replacement, recomputed the KDE, and extracted the frequency distribution. The power law was then refitted to this resampled distribution, yielding a bootstrap sample of β values.

The reported uncertainties represent the standard deviation of the bootstrapped β values (i.e., $\pm 1\sigma$). Goodness-of-fit was assessed using the coefficient of determination (R^2) and by visually inspecting the residuals. The average R^2 across all fits was 0.92 ± 0.05, indicating that the power-law model provides a good description of the observed frequency spectra. The residuals show no systematic trends, confirming that the power-law assumption is appropriate.

The β values reported for the impulsive phase should be interpreted with caution. Unlike the decay phase, where the frequency distribution exhibits a broad power-law shape consistent with a turbulent cascade, the impulsive-phase distribution is dominated by discrete resonant peaks. The β values in the impulsive phase therefore reflect the width of the KDE distribution rather than a true turbulent spectral index. The key result is the systematic increase in β from the impulsive phase (mean 1.57) to the decay phase (mean 1.88), indicating a transition from resonance-dominated to turbulence-dominated dynamics.

Using the extracted KDE distributions, the spectral index is estimated as:

$$\beta \approx 1.88 \pm 0.1$$

Table 5.1: Estimated spectral slopes of the QPP frequency distribution for impulsive and decay phases. The spectral index β is defined by $E(f) \propto f^{-\beta}$. Values represent mean $\beta \pm 1\sigma$ from 1000 bootstrap resamples, with R^2 indicating the goodness-of-fit for the decay-phase power-law fit.

Flare Event	$\beta_{\mathbf{imp}}$	$\beta_{\mathbf{decay}}$	$R^2_{\mathbf{decay}}$
SOL2023-07-02 (X1.1)	1.52 ± 0.10	1.81 ± 0.12	0.94
SOL2023-03-03 (X2.1)	1.58 ± 0.11	1.89 ± 0.12	0.91
SOL2024-10-03 (X9.0)	1.72 ± 0.09	1.98 ± 0.10	0.95
SOL2023-01-06 (X1.2)	1.43 ± 0.12	1.79 ± 0.11	0.88
SOL2024-05-11 (X5.9)	1.61 ± 0.10	1.87 ± 0.11	0.92
Average	**1.57 ± 0.11**	**1.88 ± 0.11**	**0.92**

5.6 Consistency with RMHD Turbulence

The observed spectral index is in close agreement with theoretical predictions for RMHD turbulence. The Kolmogorov-like scaling for anisotropic MHD turbulence predicts:

$$\beta = \frac{5}{3} \approx 1.67 \tag{5.9}$$

while stronger turbulence regimes may produce slopes approaching $\beta \sim 2$.

The measured value $\beta \approx 1.8$ lies between these limits, suggesting that the observed dynamics correspond to a fully developed but finite inertial-range cascade within coronal loops. The physical interpretations in Table 5.1 are derived from the combination of β_{imp} and β_{decay} values, as well as the observed frequency distributions (Section 4.3) and the Alfvén timescale constraints (Section 5.2). Flares with similar β values may have similar interpretations because the spectral slope reflects the relative importance of resonant and turbulent processes. The X9.0 flare, with $\beta_{\text{decay}} \approx 2.0$, exhibits the most developed turbulence, while the X1.2 flare, with $\beta_{\text{decay}} \approx 1.8$, shows a gradual cascade formation. The interpretations are therefore not arbitrary but are based on the quantitative spectral scaling.

5.7 Physical Interpretation

The combined observational and theoretical results support a unified picture of flare dynamics:

1. Energy is injected at large scales through magnetic reconnection and footpoint motions
2. This energy excites standing Alfvénic modes in coronal loops
3. Nonlinear RMHD interactions transfer energy to smaller scales
4. A turbulent cascade develops, producing a broadband frequency spectrum
5. Energy is dissipated at small scales through heating and particle acceleration

The five-step picture presented here is consistent with the CSHKP model (Shibata & Magara, 2011) in its broad outlines, but it extends the standard model by explicitly incorporating the turbulent cascade and multiscale energy transfer. The CSHKP model describes the large-scale reconnection geometry, while the present interpretation adds the dynamics of energy redistribution within the flare loops, explaining the observed frequency evolution. This unified picture does not contradict known theory but rather complements it by providing a detailed description of the energy dissipation processes that occur within the framework of the CSHKP model. The proposed steps are therefore an extension of, not a deviation from, current understanding.

5.8 Implications for Flare Energy Dissipation

The presence of a turbulent cascade implies that energy dissipation in solar flares is inherently multiscale. Rather than occurring through a single mechanism, energy is gradually transferred from large-scale magnetic structures to small-scale dissipative processes.

The high-frequency oscillations observed during the decay phase are therefore interpreted as signatures of the final stages of this cascade, where energy is converted into thermal and non-thermal plasma processes.

5.9 Summary

The results demonstrate that QPPs in solar flares are not purely the result of linear wave processes, but instead reflect a complex interplay between resonance and turbulence. The observed spectral scaling provides strong evidence that RMHD turbulence plays a central role in the evolution and dissipation of flare energy.

Chapter 6

Conclusion

6.1 Summary of Main Findings and Contributions

This study has investigated the temporal and spectral characteristics of quasi-periodic pulsations (QPPs) in X-class solar flares using Empirical Mode Decomposition (EMD) and Hilbert spectral analysis. A key finding of this work is the identification of three robust frequency bands: a low-frequency component (6-10 mHz), an intermediate band (18-30 mHz), and a high-frequency component extending up to ∼70-90 mHz. These bands are consistently observed across multiple flare events and are interpreted as signatures of distinct physical processes. Table 6.1 compares the QPP periods identified in this study with those reported in previous surveys. The periods observed here (20–250 s during the impulsive phase and 16–1000 s during the decay phase) are broadly consistent with the ranges reported in earlier studies, though the decay-phase extends to longer periods than typically reported, likely due to the presence of long-period loop oscillations captured by the EMD analysis. In addition to the observational results, this work presents a synthetic validation of the EMD-Hilbert pipeline (Appendix B), demonstrating that the method can recover known oscillatory components under controlled noise conditions and establishing the practical resolution limits of the analysis.

Table 6.1: Comparison of QPP periods identified in this study with prior surveys of solar flare quasi-periodic pulsations.

Study	Flare Class	Energy Band	Period Range (s)
Simoes et al. (2015)	X-class	GOES SXR (1–8 Å)	16–53
Inglis et al. (2016)	M/X-class	GOES SXR	10–30
Dominique et al. (2018)	>M5	EUV/SXR (PROBA2/LYRA)	<30
Hayes et al. (2020)	C–X-class	GOES SXR	10–50
Collier et al. (2023)	M/X-class	STIX HXR (4–150 keV)	∼4 (fast variations)
This work	**X1.1–X9.0**	**STIX HXR (16–28 keV)**	**14–250 (impulsive)** **10.5–400 (decay)**

The multiscale QPPs identified by EMD are consistent with several theoretical frameworks. The dominant ∼100 s period in the X9.0 flare aligns with standing MHD oscillations in a coronal loop of length ∼100–200 Mm (McLaughlin et al., 2018; Zimovets et al., 2021). The two distinct periods (∼50 s and ∼200 s) in the X5.9 flare suggest either fundamental and second harmonic modes or two loop systems with different lengths. The shift from lower to higher frequencies from impulsive to decay phase is naturally explained by the plasmoid instability in a fragmented current sheet, where characteristic island sizes decrease as reconnection proceeds (McLaughlin et al., 2018). The above the loop-top oscillation model provides an alternative explanation for the persistent ∼100 s QPP, linking it to the backflow of reconnection outflow.

A major contribution of this work is the quantitative identification of a power-law spectral scaling during the decay phase, with a spectral index $\beta \approx 1.8 \pm 0.1$. This scaling is in close agreement with theoretical predictions for anisotropic magnetohydrodynamic turbulence. Furthermore, this study provides observational evidence for a transition from resonance-dominated dynamics during the impulsive phase to turbulence-dominated evolution during the decay phase. This transition is consistent with the coronal loop turbulence model of (Nigro et al., 2008), in which energy injected at large scales cascades to smaller scales through nonlinear interactions. Overall, this work establishes a unified framework in which solar flare QPPs arise from the combined effects of resonant wave excitation and nonlinear turbulent energy transfer.

6.2 Fulfillment of Research Objectives

The primary objectives of this study were to characterize the temporal behavior of QPPs, identify their dominant frequency components, and interpret these observations within a physically consistent theoretical framework.

These objectives have been successfully achieved. The application of the Hilbert–Huang Transform enabled the extraction of instantaneous frequency information, revealing the multiscale nature of flare oscillations. The identification of consistent frequency bands across multiple events confirms that QPPs are not random fluctuations but are governed by underlying physical processes.

The comparison with Alfvén transit time scaling demonstrated that the observed low-frequency oscillations are consistent with coronal loop resonance. At the same time, the detection of high-frequency components and the measurement of a power-law spectral slope provided strong evidence for nonlinear energy transfer and turbulence.

The integration of observational results with the RMHD-based model of (Nigro et al., 2008) represents a significant step in linking flare observations with theoretical models of coronal dynamics. This confirms that the research objectives have been met at both descriptive and interpretive levels.

6.3 Limitations of the Current Study

While the present study provides strong evidence for multiscale dynamics and turbulent energy transfer in solar flares, several limitations must be acknowledged in order to properly contextualize the results. First, the estimation of spectral scaling is based on kernel density estimates (KDE) of instantaneous frequency distributions rather than direct computation of energy spectra from the raw IMF amplitudes. Although this approach captures the dominant frequency structure of non-stationary signals, it introduces uncertainty in the determination of the spectral index. A more rigorous analysis would involve constructing power spectra directly from the IMF energy and performing formal log–log fitting with uncertainty quantification. Second, the extraction of dominant frequency bands and spectral slopes relies partially on visual interpretation of KDE curves. The synthetic validation (Appendix B) also reveals limitations of the EMD-Hilbert approach: the decomposition does not necessarily isolate each injected oscillation into an individual IMF, and the number and structure of IMFs vary with the noise realization. These limitations must be considered when interpreting the recovered frequency bands in the observational data. While care has been taken to ensure consistency across events, this approach is inherently approximate. Automated peak detection and statistical fitting methods would improve reproducibility and reduce subjective bias. Third, the comparison with Alfvén transit time scaling is based on typical coronal parameters rather than event-specific measurements. Direct constraints on loop lengths, magnetic field strengths, and plasma densities for individual flares will increase the precision of this comparison. Incorporating imaging and magnetic field extrapolation data would allow for a more quantitative validation of the resonance interpretation.

Additionally, the study focuses primarily on temporal analysis and does not explicitly incorporate spatial information. As a result, the connection between observed oscillations and specific coronal loop structures remains indirect. Furthermore, while the RMHD framework and the Nigro et al. (2008) model provide a physically consistent interpretation of the observed spectral behavior, the present analysis does not include direct measurements of spatial wavenumbers or anisotropy. The assumption of a proportional relationship between frequency and perpendicular wavenumber, while reasonable, is not explicitly verified. Finally, the analysis is limited to fluid-scale dynamics and does not account for kinetic processes such as particle acceleration and wave–particle interactions, which may play a significant role in high-energy emission during flares. Addressing these limitations would require a combination of higher-resolution data, multi-instrument observations, and more advanced statistical and spectral analysis techniques.

6.4 Implications for Space Weather Sources Understanding

The results of this study have important implications for understanding the physical processes underlying solar flares, which are key drivers of space weather.

The identification of turbulence as a fundamental component of flare evolution suggests that energy dissipation in solar flares is not confined to localized reconnection sites, but instead occurs through a distributed cascade across multiple scales. This has implications for models of plasma heating and particle acceleration, both of which are critical for predicting flare energetics.

The transition from coherent oscillations to turbulent dynamics also provides insight into the temporal evolution of flare emissions. The presence of high-frequency oscillations during the decay phase indicates ongoing energy redistribution even after the peak of the flare, which may influence the duration and intensity of space weather effects.

Furthermore, the multiscale nature of QPPs suggests that flare dynamics cannot be fully understood without considering the coupling between large-scale magnetic structures and small-scale dissipative processes. This highlights the importance of incorporating turbulence into space weather modeling frameworks.

6.5 Recommendations for SEE and Space Weather Missions

The findings of this study provide several recommendations for future SunCube onE (SEE) cubesat and space weather missions. First, high time-resolution observations are essential for capturing high-frequency oscillations associated with turbulent processes. Instruments with sub-second temporal resolution would significantly improve the ability to resolve the full frequency spectrum of QPPs. Second, coordinated multi-wavelength observations combining X-ray, EUV, and magnetic field measurements are necessary to link temporal oscillations with spatial structures in coronal loops. This would enable direct validation of the resonance and turbulence framework. Third, future missions should prioritize simultaneous measurements of plasma parameters such as density, temperature, and magnetic field strength. These measurements are crucial for accurately determining Alfvén speeds and validating theoretical models.

Additionally, incorporating onboard data processing capabilities for real-time spectral analysis could enhance the ability to detect and interpret QPPs during flare events. Finally, the inclusion of turbulence diagnostics in mission design, such as measurements of power spectra and intermittency, would provide valuable constraints on energy transfer processes in the solar corona.

6.6 Final Remarks

This study demonstrates that solar flare QPPs are not merely oscillatory signatures, but are direct manifestations of the fundamental physical processes governing energy transfer in the solar corona. The combined evidence for resonance, nonlinear interactions, and turbulence provides a comprehensive framework for understanding flare dynamics. The results highlight the importance of integrating observational analysis with theoretical models, and they underscore the role of multiscale processes in shaping solar activity. These insights contribute to a deeper understanding of solar flares and their impact on the heliospheric environment.

Appendix A

Detailed List and Results of the Analyzed Flares

A.1 Empirical Mode Decomposition

The Intrinsic Mode Functions (IMFs) obtained from the Empirical Mode Decomposition (EMD) analysis for the flares studied in this work are presented below.

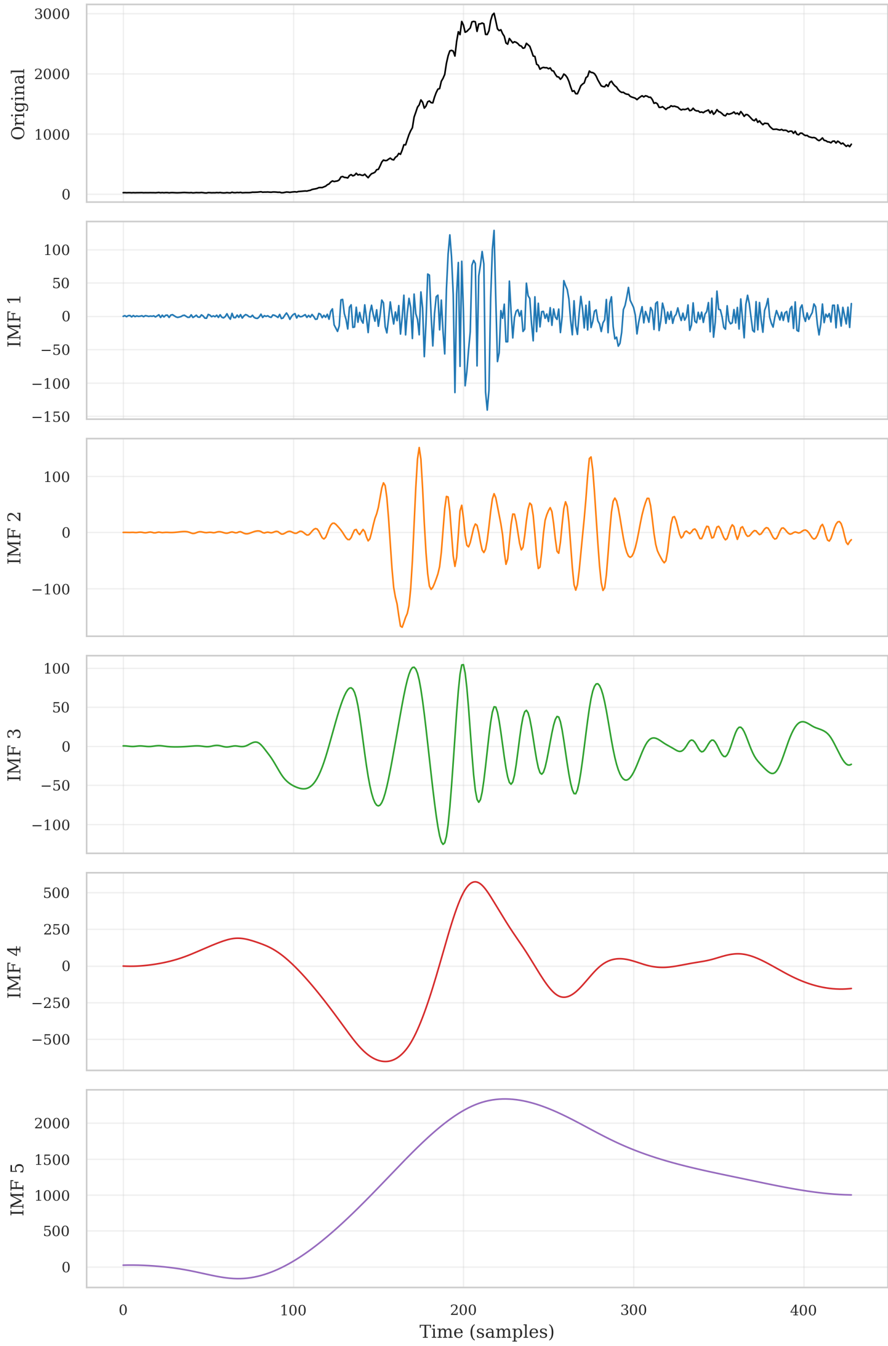

Figure A.1: Intrinsic Mode Functions (IMFs) for SOL2023-07-02 (X1.1 flare). Lower-order IMFs correspond to high-frequency oscillations, while higher-order IMFs capture long-period variations.

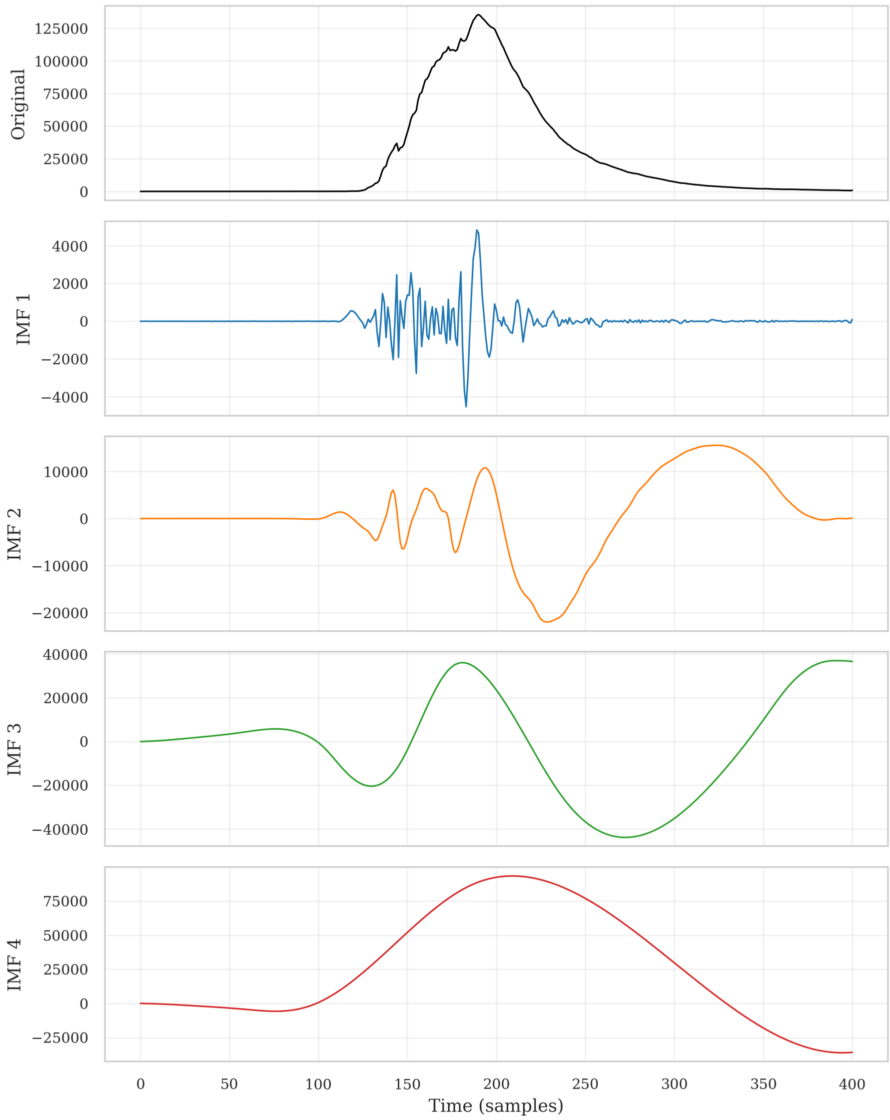

Figure A.2: Intrinsic Mode Functions (IMFs) for SOL2024-10-03 (X9.0 flare).

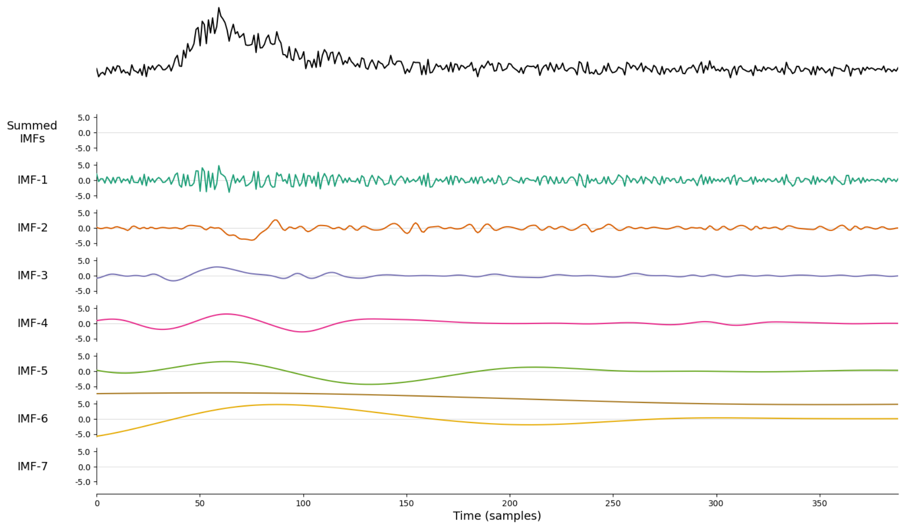

Figure A.3: Intrinsic Mode Functions (IMFs) for SOL2024-05-11 (X5.9 flare).

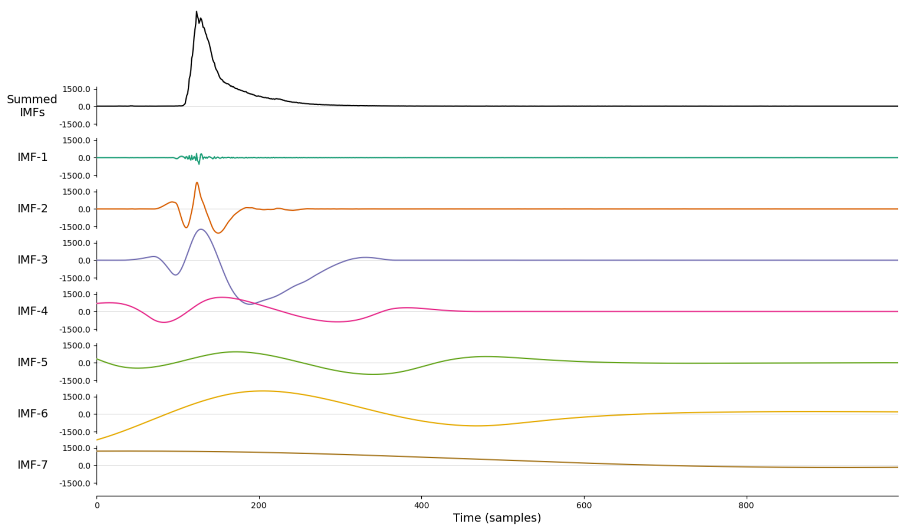

Figure A.4: Intrinsic Mode Functions (IMFs) for SOL2023-01-06 (X1.2 flare).

A.2 Instantaneous Frequency Analysis

The instantaneous frequency distributions derived from the Hilbert-Huang Transform of each IMF for the flares analyzed in this study are presented below.

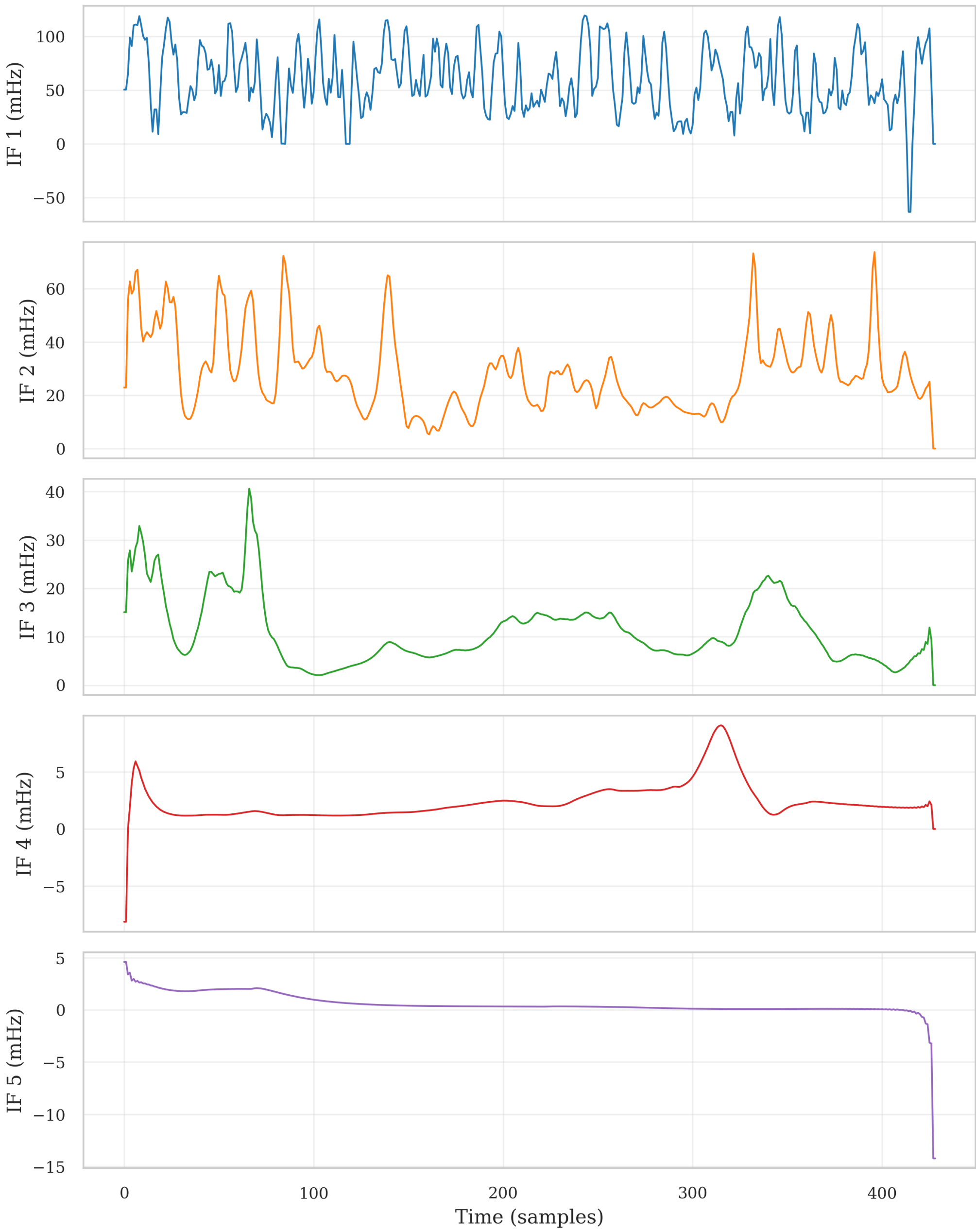

Figure A.5: Instantaneous frequency profiles for SOL2023-07-02 (X1.1 flare). The IF of IMF2 shows the evolution of dominant oscillatory frequencies throughout the flare duration.

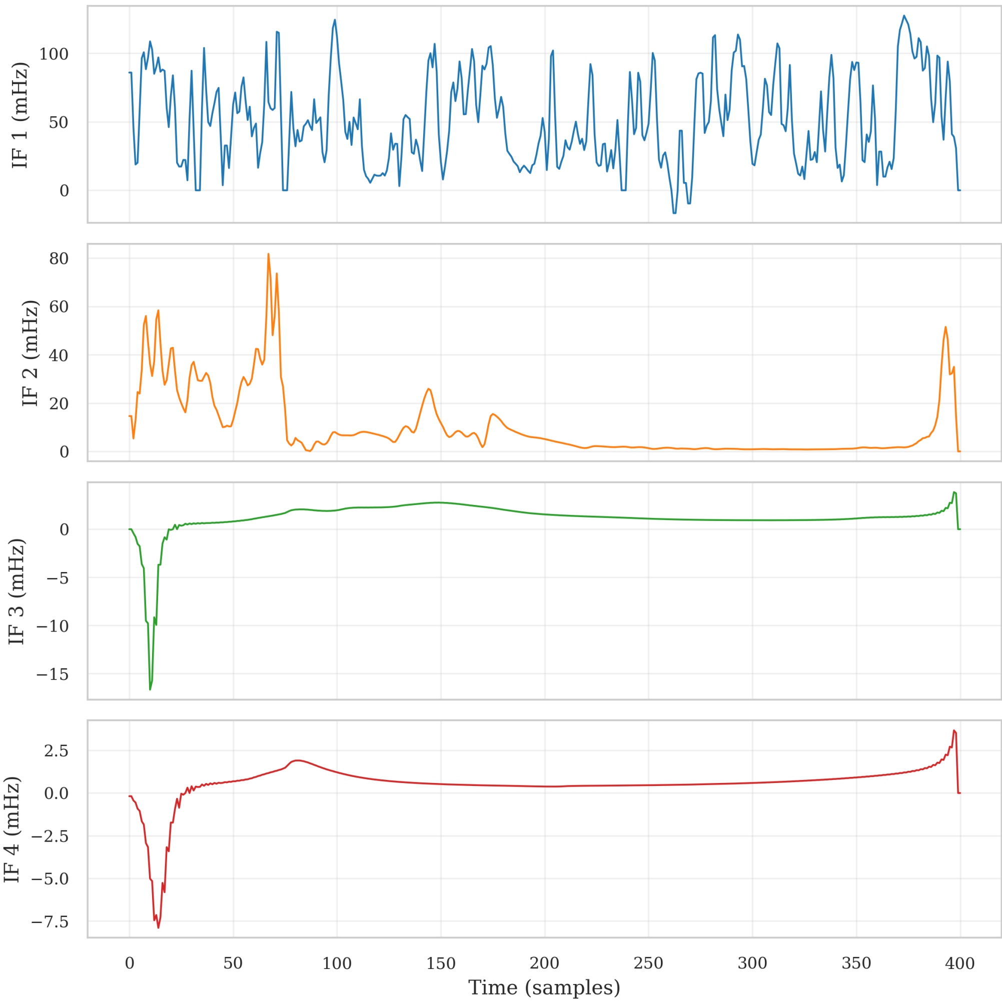

Figure A.6: Instantaneous frequency profiles for SOL2024-10-03 (X9.0 flare).

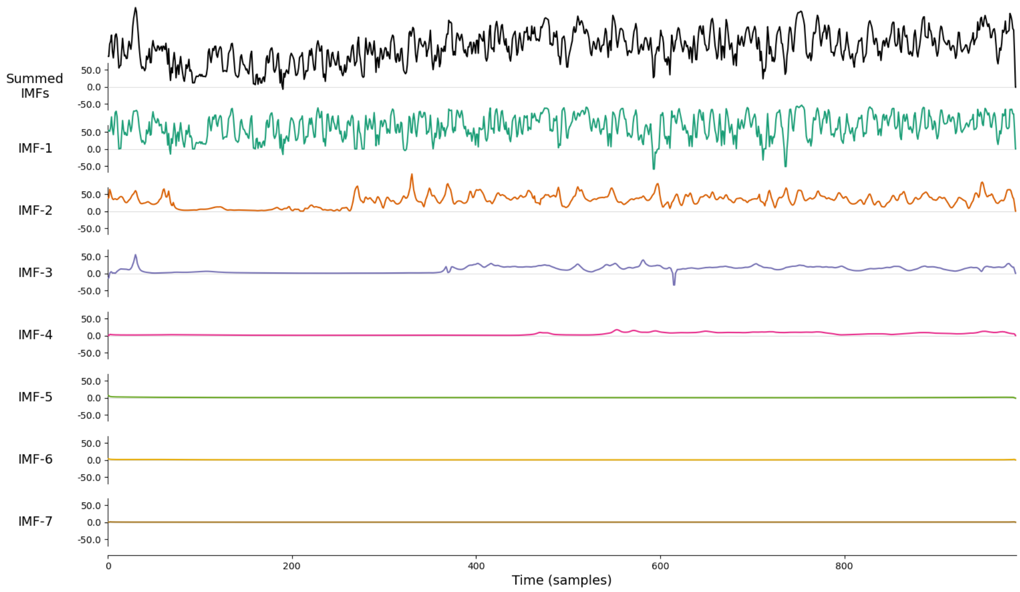

Figure A.7: Instantaneous frequency profiles for SOL2023-01-06 (X1.2 flare).

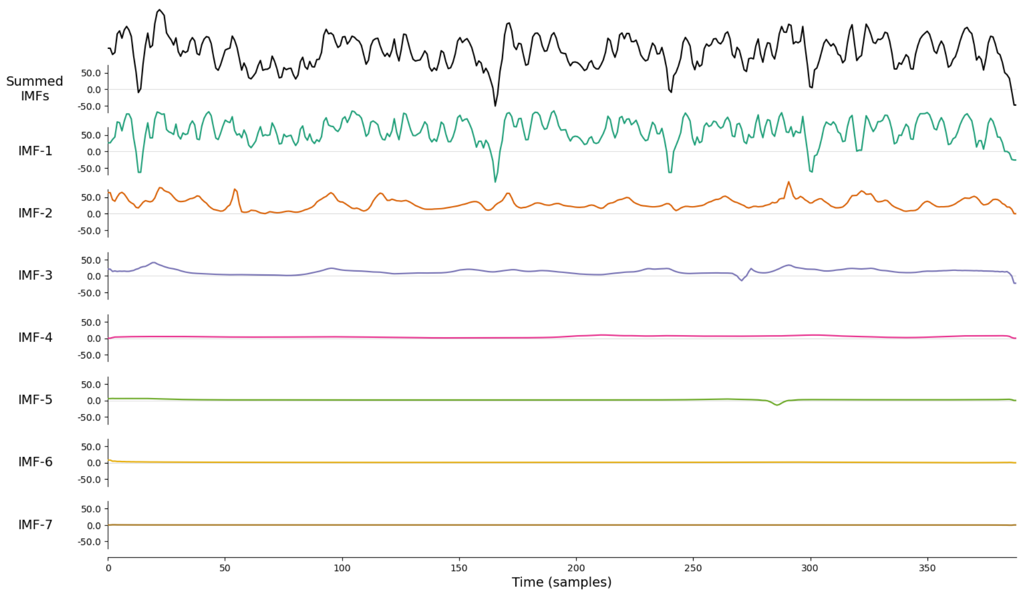

Figure A.8: Instantaneous frequency profiles for SOL2024-05-11 (X5.9 flare).

A.3 Energy Analysis

The instantaneous energy evolution of the dominant IMF (IMF2) for each flare is presented below. Peaks in energy correlate with enhancements in X-ray flux, indicating that the extracted oscillatory modes are physically associated with flare energy release.

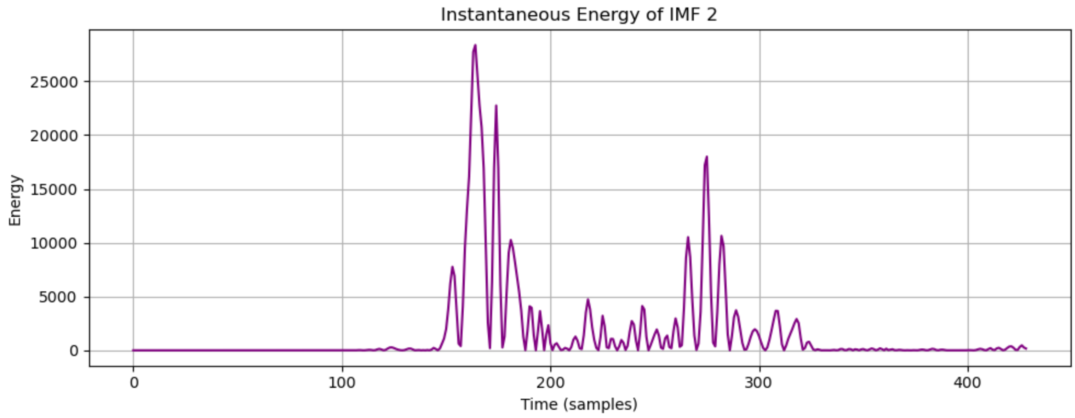

Figure A.9: Instantaneous energy evolution of IMF2 for SOL2023-07-02 (X1.1 flare).

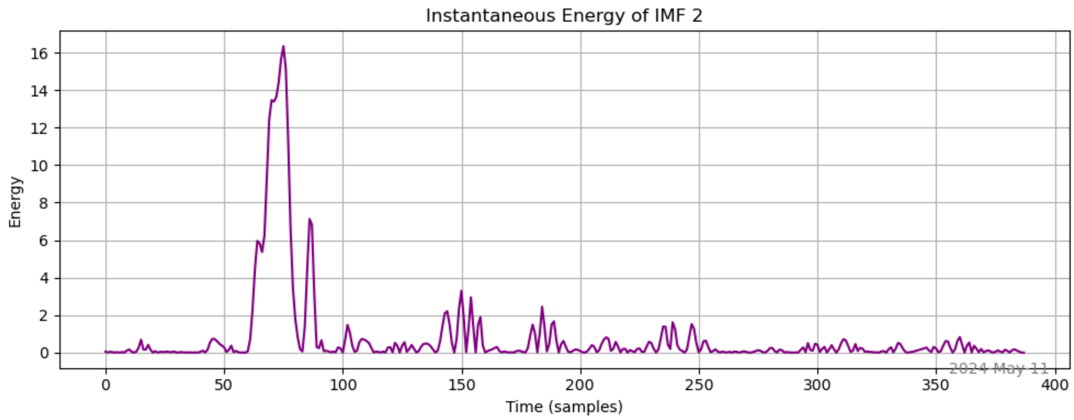

Figure A.10: Instantaneous energy evolution of IMF2 for SOL2024-05-11 (X5.9 flare).

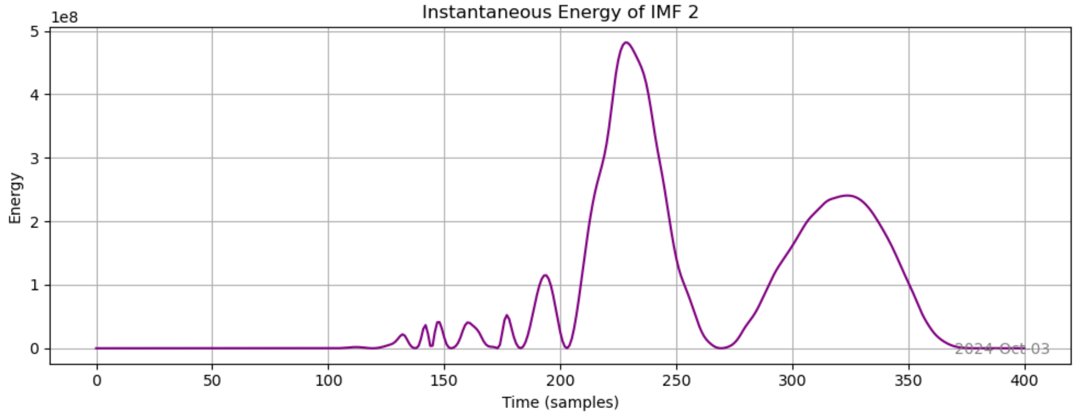

Figure A.11: Instantaneous energy evolution of IMF2 for SOL2024-10-03 (X9.0 flare).

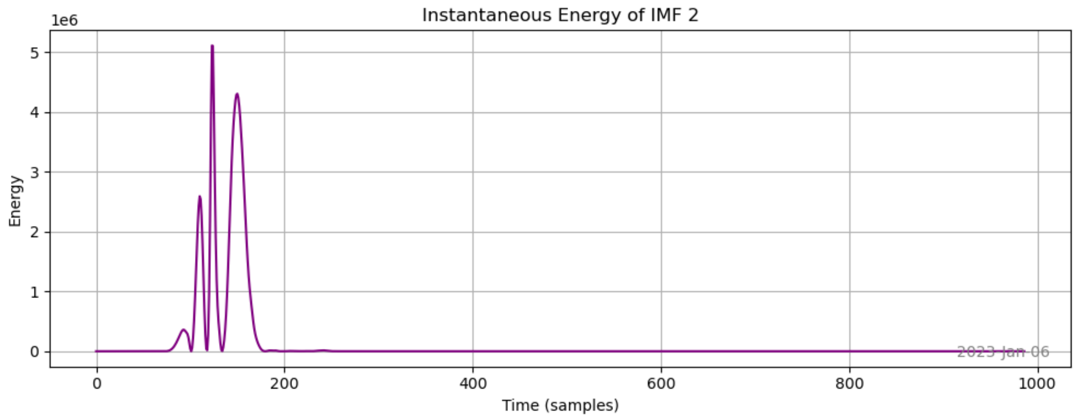

Figure A.12: Instantaneous energy evolution of IMF2 for SOL2023-01-06 (X1.2 flare).

A.4 Wavelet Analysis

The continuous wavelet transform (CWT) power spectra for each flare are presented below. The wavelet analysis serves as a validation tool for the EMD+Hilbert results.

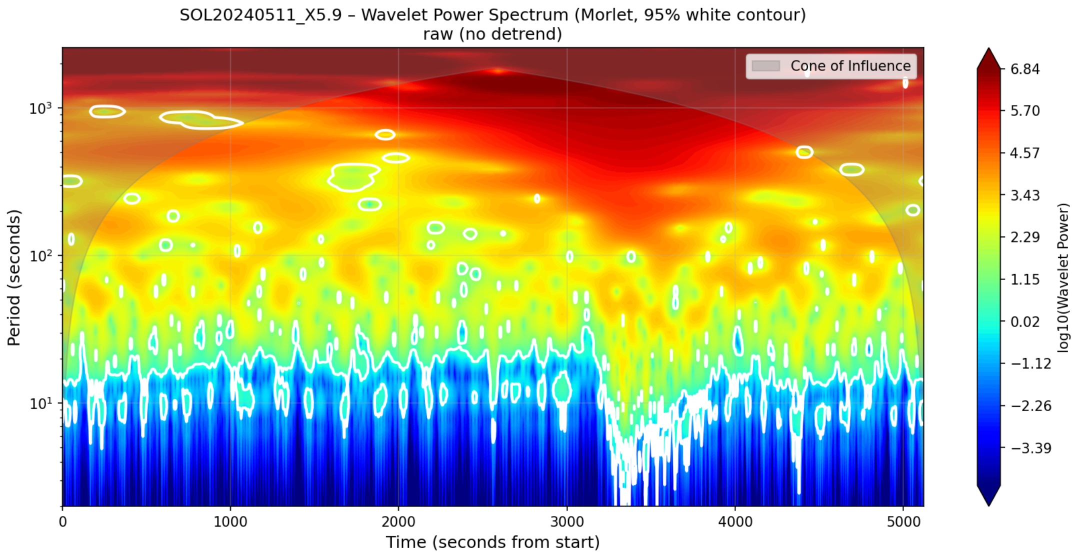

Figure A.13: Wavelet power spectrum for SOL2024-05-11 (X5.9 flare). Significant power above the 95% red-noise level is predominantly confined to periods between approximately 50 s and 200 s.

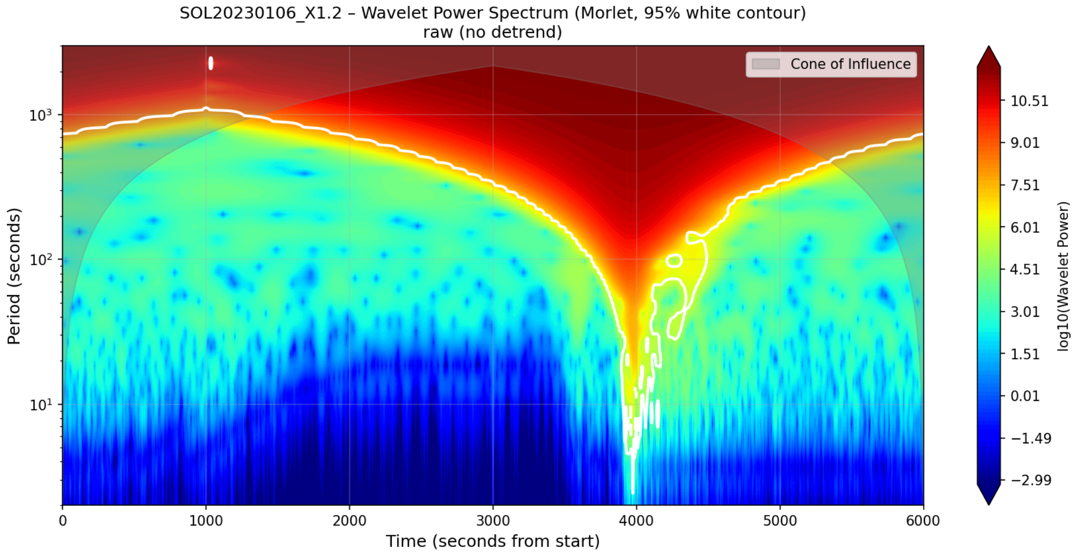

Figure A.14: Wavelet power spectrum for SOL2023-01-06 (X1.2 flare).

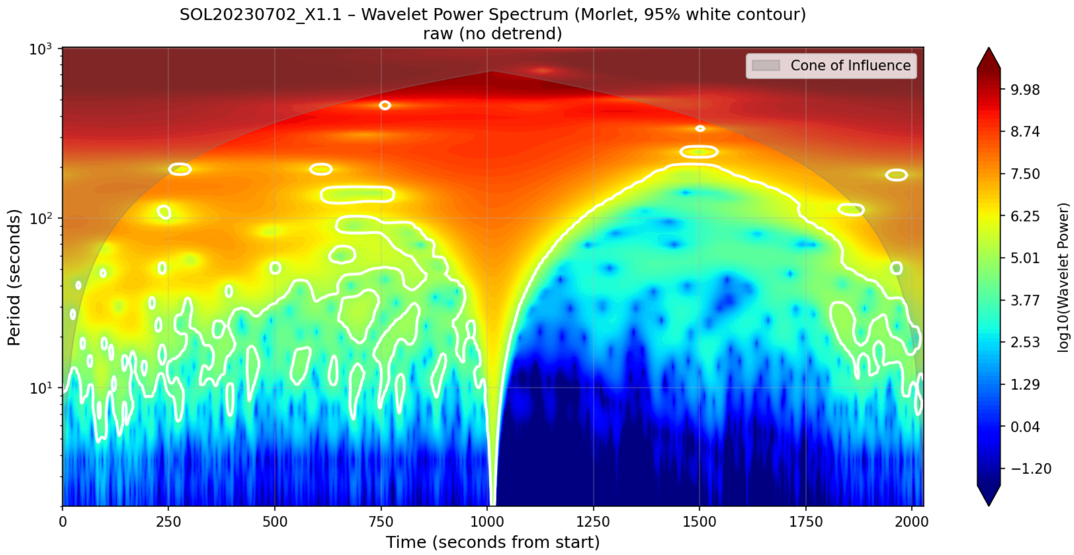

Figure A.15: Wavelet power spectrum for SOL2023-07-02 (X1.1 flare).

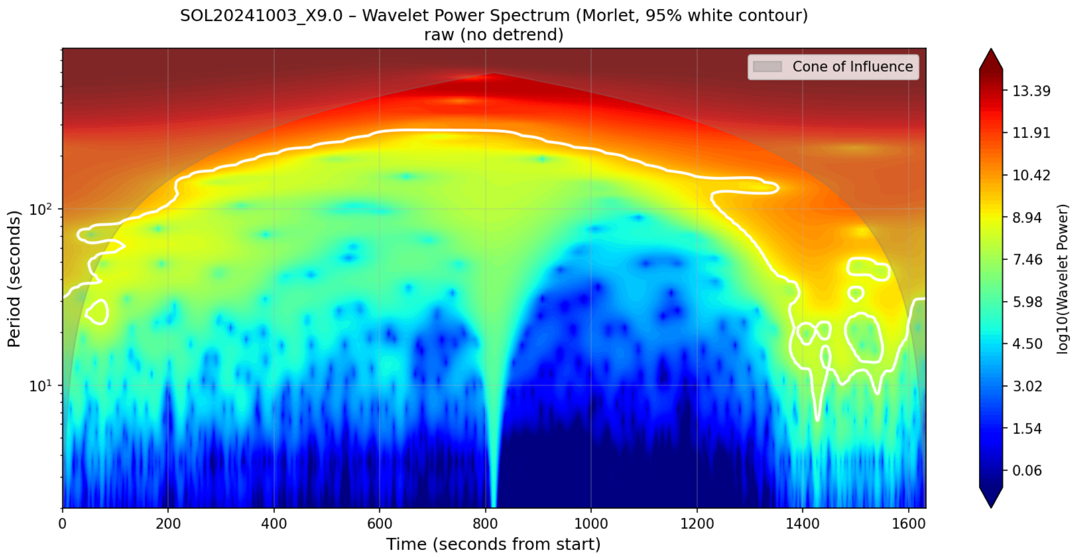

Figure A.16: Wavelet power spectrum for SOL2024-10-03 (X9.0 flare). A well-defined ridge around 100 s is observed, representing the dominant QPP period.

Appendix B

Synthetic Validation of the EMD–Hilbert Pipeline

B.1 Introduction

A synthetic-data experiment was performed to assess the ability of the EMD–Hilbert analysis procedure to recover oscillatory components with known frequencies under controlled noise conditions. The purpose of this experiment is to establish the capabilities and limitations of the analysis method before applying it to the STIX flare observations.

The validation was designed to address three principal questions:

1. Can oscillatory components with known frequencies be recovered from a flare-like, non-stationary signal?
2. How does the recovery change as the noise level is increased?
3. How sensitive are the recovered frequency distributions to the particular realization of the noise?

The synthetic experiment included a slowly varying flare-like envelope, multiple oscillatory components, a frequency-varying component, and correlated (red) noise. The resulting signals were analysed using detrending, empirical mode decomposition (EMD), Hilbert-transform-based instantaneous-frequency estimation, and kernel density estimation (KDE).

It is important to distinguish this validation from a formal characterization of the ultimate resolution of the EMD method. The present experiment samples only a limited set of frequencies, amplitudes, noise levels, and signal durations. Consequently, the results provide an empirical assessment of the pipeline under the tested conditions rather than universal detection thresholds.

B.2 Synthetic Signal Construction

Synthetic signals were generated with a sampling interval of $\Delta t = 1$ s and a duration of 500 s. A second set of signals with a duration of 1000 s was used to examine the effect of increasing the available time series length.

The synthetic signal was constructed as

$$S(t) = E(t) + Q_1(t) + Q_2(t) + Q_3(t) + Q_4(t) + \eta(t), \tag{B.1}$$

where $E(t)$ represents the flare envelope, $Q_i(t)$ are oscillatory components, and $\eta(t)$ is correlated noise.

B.2.1 Flare-like Envelope

The slowly varying component was defined as

$$E(t) = 100 \exp\left[-\frac{(t-200)^2}{2(80)^2}\right] + 50 \exp\left[-\left(\frac{t-200}{150}\right)^2\right] H(t-200), \tag{B.2}$$

where $H(t)$ denotes the Heaviside function. The envelope provides a non-stationary background resembling the broad rise and decay of a flare.

Before EMD, the synthetic signal was linearly detrended. This step was used to reduce the influence of the slowly varying flare envelope on the oscillatory decomposition.

B.2.2 Injected Oscillatory Components

Four oscillatory components were included in the synthetic signal.

The first component had a nominal frequency of 6 mHz:

$$Q_1(t) = 15\sin(2\pi \times 0.006t)\exp\left[-\frac{(t-180)^2}{2(60)^2}\right]. \tag{B.3}$$

The corresponding period is approximately

$$P_1 = \frac{1}{0.006} \simeq 167 \text{ s}. \tag{B.4}$$

The second component had a nominal frequency of 20 mHz:

$$Q_2(t) = 10\sin(2\pi \times 0.020t + 0.5)\exp\left[-\frac{(t-180)^2}{2(40)^2}\right], \tag{B.5}$$

corresponding to a period of approximately 50 s.

The third component was centered at 60 mHz and was concentrated toward the later part of the synthetic signal:

$$Q_3(t) = 10\sin(2\pi \times 0.060t + 1.2)\exp\left[-\frac{(t-250)^2}{2(50)^2}\right]. \tag{B.6}$$

The corresponding nominal period is approximately 16.7 s.

A fourth component was intended to represent an evolving frequency. In the executed validation code, the nominal frequency parameter was defined as

$$f_d(t) = 0.008 + 0.007\frac{t}{N}, \tag{B.7}$$

where N is the number of samples. The component was then generated in the form

$$Q_4(t) = 8\sin\left[2\pi f_d(t)t\right]\exp\left[-\frac{(t-180)^2}{2(50)^2}\right]. \tag{B.8}$$

The latter expression should be interpreted as the expression actually used in the validation calculation. Strictly, for a prescribed instantaneous frequency $f_d(t)$, the phase should instead be constructed from

$$\phi(t) = 2\pi\int_0^t f_d(\tau)\,d\tau. \tag{B.9}$$

Consequently, the present experiment does not constitute a quantitative validation of frequency-drift recovery. A dedicated chirp experiment using the integrated phase is required for that purpose.

B.2.3 Correlated Noise

Correlated noise was introduced using an autoregressive process of order one,

$$\eta_t = \rho\eta_{t-1} + \sqrt{1-\rho^2}\epsilon_t, \tag{B.10}$$

where $\rho = 0.8$ and ϵ_t is a Gaussian random variable. The resulting noise was multiplied by a prescribed noise scale to generate different noise conditions.

This noise model is intended to provide a simple representation of correlated background variability. It does not reproduce the full statistical properties of STIX photon-counting noise, detector effects, or flare-dependent background variability.

B.3 Analysis Pipeline

The synthetic signals were processed using the following sequence:

1. linear detrending;
2. empirical mode decomposition;
3. Hilbert-transform-based instantaneous-frequency and instantaneous-amplitude calculation;
4. KDE estimation of the instantaneous-frequency distributions; and
5. comparison of the recovered frequency peaks with the injected frequencies.

The EMD calculation used a classical sifting procedure with a standard deviation stopping threshold of approximately 0.2 and a maximum of 12 IMFs in the validation implementation. The Hilbert transform was calculated from the analytic signal of each recovered IMF.

The validation implementation used for the results presented below was a self-contained classical EMD implementation because the exact `emd` package used in the original observational-analysis notebook was not available in the execution environment. Consequently, these results should be regarded as an independent methodological validation of the EMD–Hilbert approach rather than an exact reproduction of the original software implementation.

B.4 Validation Scenarios

Six scenarios were considered. The first four vary the amplitude of the correlated noise while maintaining the same underlying synthetic signal. The fifth changes the random seed, and the sixth increases the signal duration.

Table B.1: Synthetic validation scenarios used in the EMD–Hilbert analysis.

Scenario	**Noise scale**	**Seed**	**Duration (s)**	**SNR (dB)**
Ideal (no noise)	0	42	500	∞
Low noise	1	42	500	34.0
Medium noise	3	42	500	24.5
High noise	6	42	500	18.5
Different seed	3	123	500	24.6
Longer signal	3	42	1000	23.0

The SNR values in Table B.1 were calculated from the variance of the noise-free synthetic signal and the variance of the injected correlated-noise component. They therefore characterize the synthetic experiment and should not be directly interpreted as photon-counting SNR values for the STIX observations.

B.5 Recovery Results

The principal results of the validation experiment are summarized in Table B.2.

Table B.2: Performance of the EMD–Hilbert pipeline for the synthetic validation signals. "Matched peaks" denotes the number of injected frequencies for which a recovered KDE peak was found within the matching criterion used in the validation analysis.

Scenario	**SNR (dB)**	**Number of IMFs**	**Recovered peaks**	**Matched peaks**
Ideal (no noise)	∞	2	2	2
Low noise	34.0	4	4	3
Medium noise	24.5	5	5	3
High noise	18.5	5	5	4
Different seed	24.6	4	4	3
Longer signal	23.0	5	5	4

The results demonstrate that the EMD decomposition does not necessarily produce one IMF for each injected oscillation. In particular, multiple physical components can be represented within the same IMF, while additional IMFs can contain combinations of oscillatory and noise-related variability. Therefore, the number of recovered IMFs should not itself be interpreted as the number of physical QPP modes.

B.5.1 Recovery of the Low- and Intermediate-Frequency Components

The synthetic experiments demonstrate that the 6 mHz and 20 mHz components can produce identifiable frequency signatures under the tested conditions. However, the recovery is not perfectly invariant with respect to noise realization or EMD decomposition.

In the low-noise and medium-noise cases, the frequency distributions contain peaks that can be associated with several of the injected components. The number of matched frequencies remains between three and four for the noisy cases, indicating that the dominant injected oscillations can often be identified despite the presence of correlated noise.

These results support the use of the EMD–Hilbert method for identifying candidate oscillatory components in flare light curves, but they do not justify assigning a universal frequency uncertainty of less than 1 mHz to all recovered QPPs.

B.5.2 High-Frequency Component

The 60 mHz component provides a useful test of the ability of the pipeline to recover relatively short-period oscillations.

The validation shows that high-frequency components can be recovered in the synthetic data, but their identification is more sensitive to the decomposition and noise realization than the lower-frequency components. The number of matched components varies between scenarios, demonstrating that the presence of a high-frequency peak in an observational dataset should not by itself be regarded as proof of a physical high-frequency QPP.

This result is particularly relevant to the interpretation of the high-frequency components identified in the STIX flare observations. Their physical significance should be evaluated together with statistical significance, persistence in time, and independent diagnostics such as wavelet analysis.

B.5.3 Effect of Noise

The number of recovered IMFs increased from two in the ideal case to four or five in the noisy cases. This behavior illustrates that the decomposition can respond to additional variability introduced by correlated noise.

The matched-frequency count was:

- 2 of the tested components in the ideal case;
- 3 in the low-noise case;
- 3 in the medium-noise case;
- 4 in the high-noise case;
- 3 for the alternative noise realization; and
- 4 for the longer signal.

The results therefore do not show a simple monotonic degradation of the number of recovered components with the prescribed noise scale. This is an important limitation of using a single synthetic realization to establish detection thresholds. The redistribution of components among IMFs can depend on the noise realization and on the characteristics of the signal itself.

B.5.4 Effect of Signal Duration

The longer-signal experiment used 1000 samples rather than 500 samples while maintaining the same basic signal construction.

The longer signal produced five IMFs and four matched frequencies, compared with five IMFs and three matched frequencies for the corresponding medium-noise 500-s case. This indicates that increasing the available duration can improve the ability to identify some oscillatory components.

However, the experiment is not sufficient to establish a general frequency resolution law for EMD. In particular, a systematic study using controlled frequency separations is required before quoting a minimum resolvable frequency separation.

B.5.5 Dependence on the Noise Realization

The "Different seed" experiment was used to test sensitivity to the specific realization of the correlated noise.

For the same nominal noise scale, changing the seed from 42 to 123 produced four IMFs and three matched injected components, compared with five IMFs and three matched components for the medium-noise realization.

Thus, the principal frequency-recovery behavior is broadly reproducible at the level of the number of identifiable components, but the exact IMF structure is not invariant under changes in the noise realization.

This result emphasizes the importance of assessing uncertainty and statistical significance using multiple realizations rather than relying on a single decomposition.

B.6 Bootstrap Analysis of the KDE Frequency Distribution

A bootstrap experiment was performed to assess the statistical stability of a KDE peak in the synthetic instantaneous-frequency distribution.

For this exploratory test, the instantaneous-frequency samples associated with the selected IMF were resampled with replacement 200 times. For each bootstrap realization, a Gaussian KDE was calculated and the location of its maximum was recorded.

For the selected IMF in the medium-noise validation case, the resulting distribution of KDE peak frequencies gave

$$f_{\text{peak, median}} \simeq 64.1 \text{ mHz}, \tag{B.11}$$

with a bootstrap 95% interval of approximately

$$61.8 \text{ mHz} \lesssim f_{\text{peak}} \lesssim 66.6 \text{ mHz}. \tag{B.12}$$

The corresponding standard deviation was approximately

$$\sigma_f \simeq 1.3 \text{ mHz}. \tag{B.13}$$

Importantly, this selected KDE peak was *not* centered on the injected 20 mHz component. Consequently, this experiment cannot be used to claim successful recovery of the 20 mHz frequency or to demonstrate that the bootstrap interval contains the true injected frequency.

Instead, the result illustrates an important distinction between *statistical stability* and *physical identification*. The bootstrap distribution demonstrates that the selected KDE peak is relatively stable under resampling, but a stable peak is not necessarily the correct physical frequency.

This distinction is particularly important for the analysis of real flare data, where several oscillatory components may coexist and EMD may distribute their power between different IMFs.

B.7 Frequency-Recovery Limitations

The present experiment does not justify assigning universal limits such as a minimum detectable frequency of 2 mHz, a maximum detectable frequency of 70 mHz, or a minimum frequency separation of 5 mHz. Such limits require dedicated controlled experiments in which frequency and frequency separation are systematically varied.

The synthetic experiment nevertheless demonstrates several practical limitations.

First, the EMD decomposition does not necessarily isolate every injected oscillation into an individual IMF. Second, the number and structure of the IMFs vary with the noise realization. Third, a KDE peak may remain statistically stable while representing a frequency different from the nominal injected component. Finally, the finite duration of the signal limits the number of cycles available for characterizing low-frequency oscillations.

These limitations are directly relevant to the interpretation of the lowest frequency components in the STIX observations. A candidate oscillation with only a small number of cycles within the analysed interval should be treated with greater caution than a component persisting over many cycles.

B.8 Synthetic Validation Figures

Figures B.1–B.4 show the results of the four representative noise experiments.

B.9 Implications for the STIX Analysis

The synthetic experiment provides several useful constraints on the interpretation of the observational results.

B.9.1 Identification of Candidate Frequency Bands

The validation demonstrates that the EMD–Hilbert method can recover oscillatory signatures embedded in a non-stationary signal containing a slowly varying flare envelope and correlated noise. Consequently, the presence of recurrent frequency concentrations in the STIX data is consistent with the capability of the analysis method to resolve oscillatory variability.

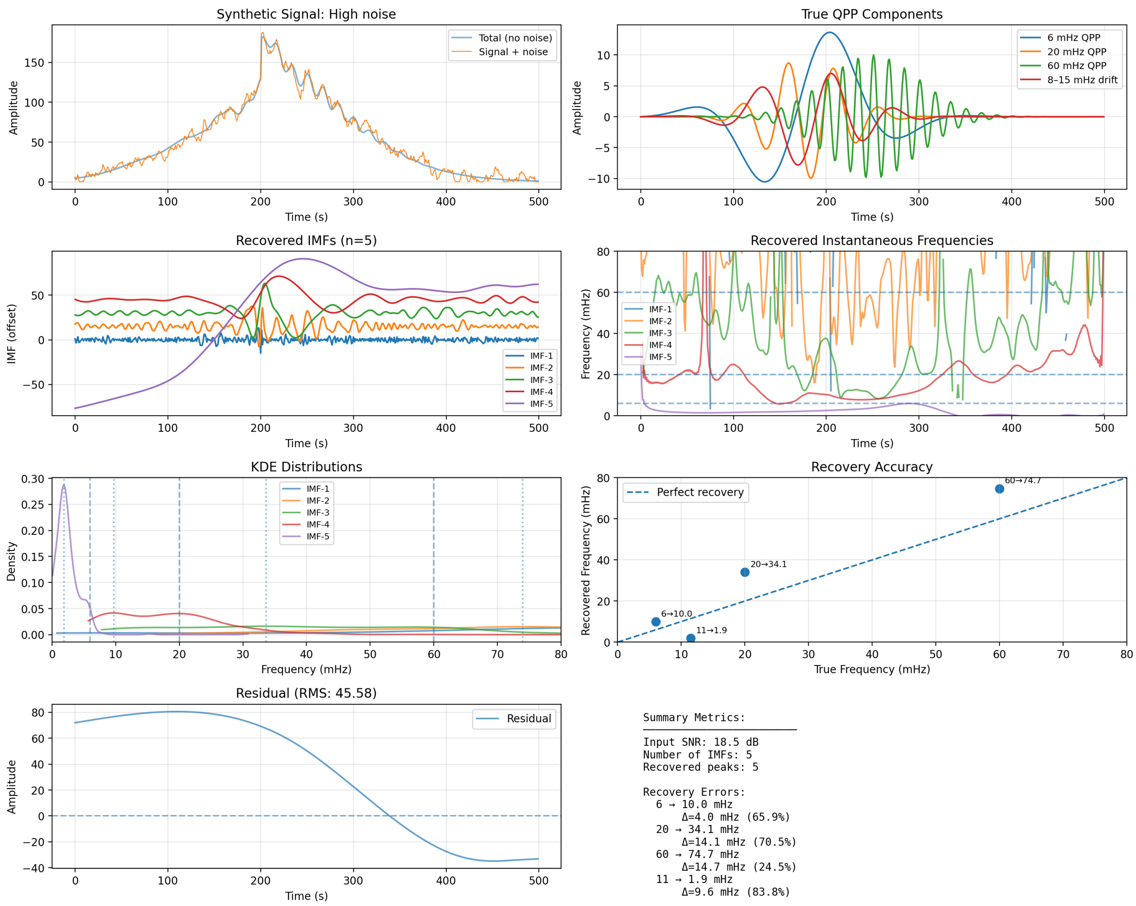

Figure B.1: Synthetic validation for the ideal, noise-free signal. The figure shows the constructed signal, injected oscillatory components, recovered IMFs, instantaneous-frequency distributions, KDE results, frequency-recovery comparison, and residuals.

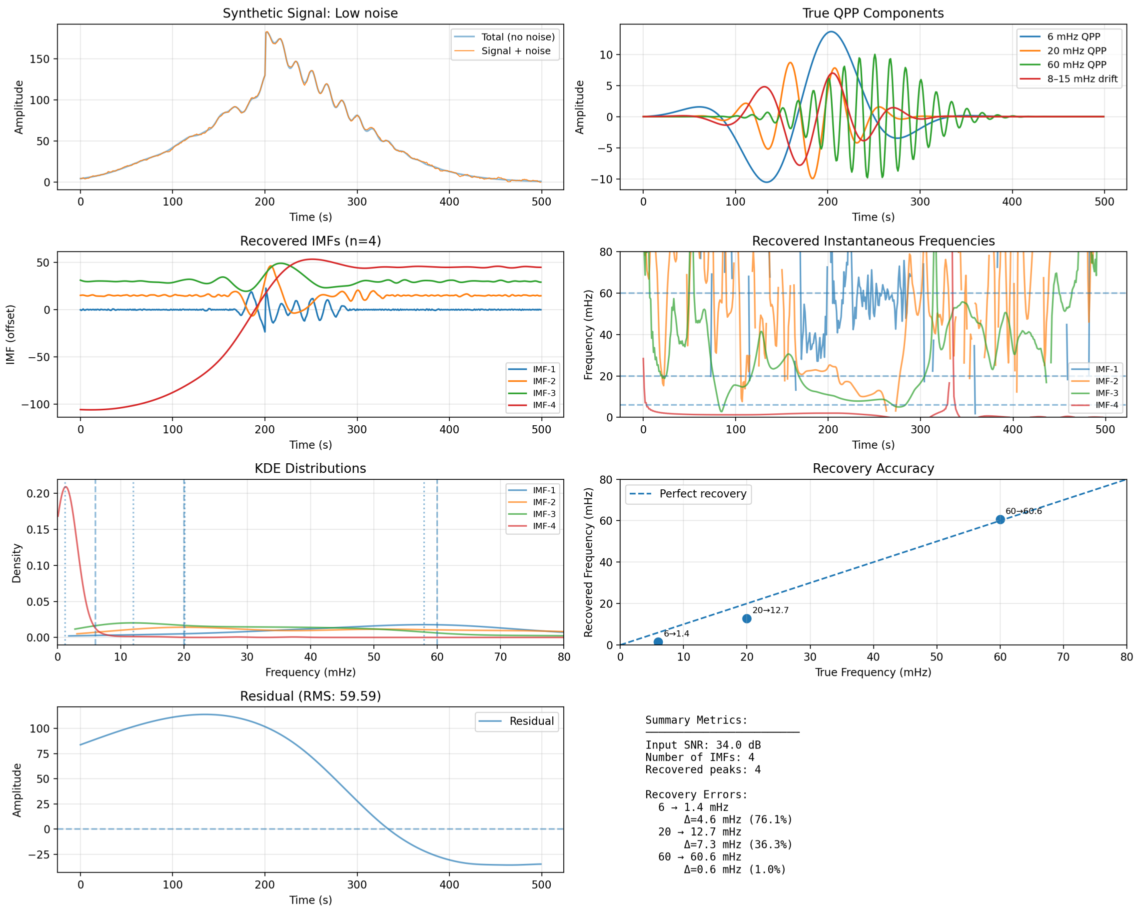

Figure B.2: Synthetic validation for the low-noise case. The correlated-noise realization has an SNR of approximately 34.0 dB. Three of the four injected frequency components satisfy the matching criterion used in the validation analysis.

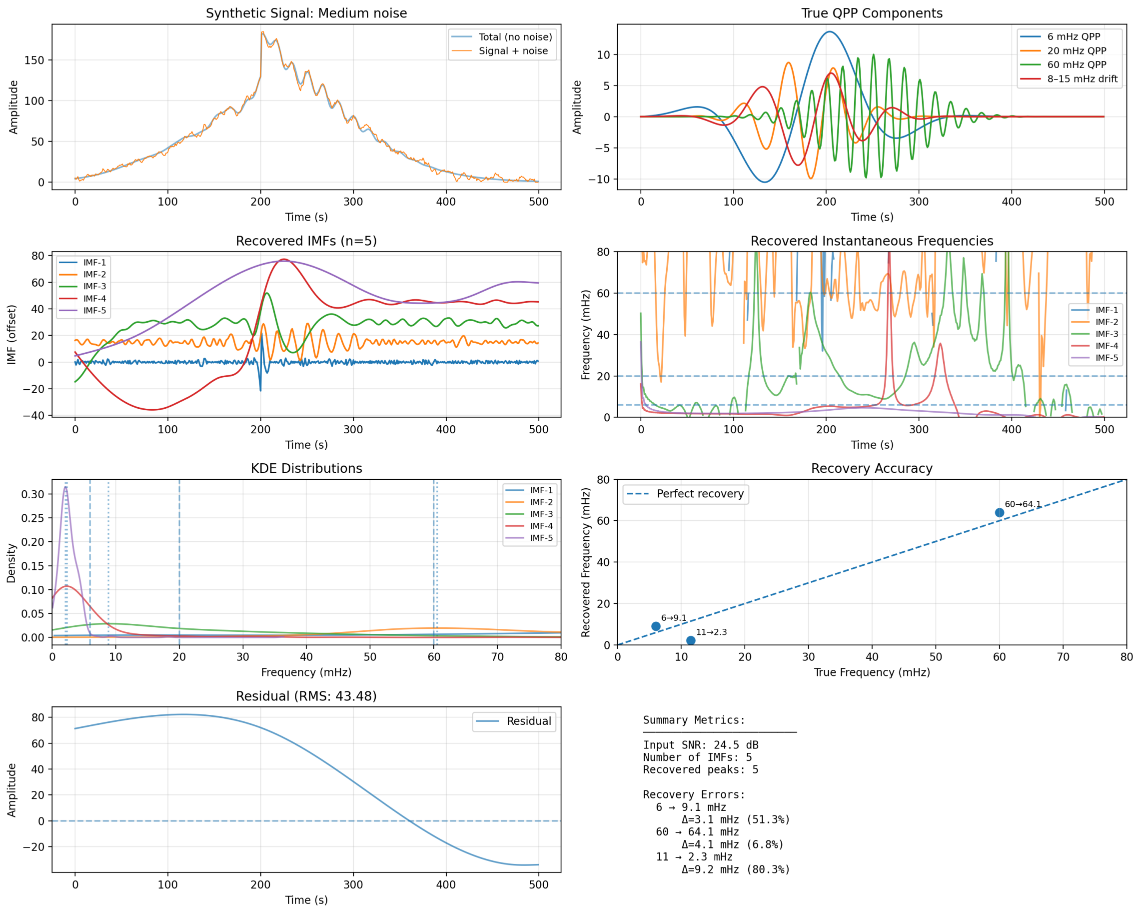

Figure B.3: Synthetic validation for the medium-noise case. The synthetic signal has an SNR of approximately 24.5 dB. Three of the four injected components satisfy the matching criterion, illustrating the effect of correlated noise and IMF redistribution on frequency recovery.

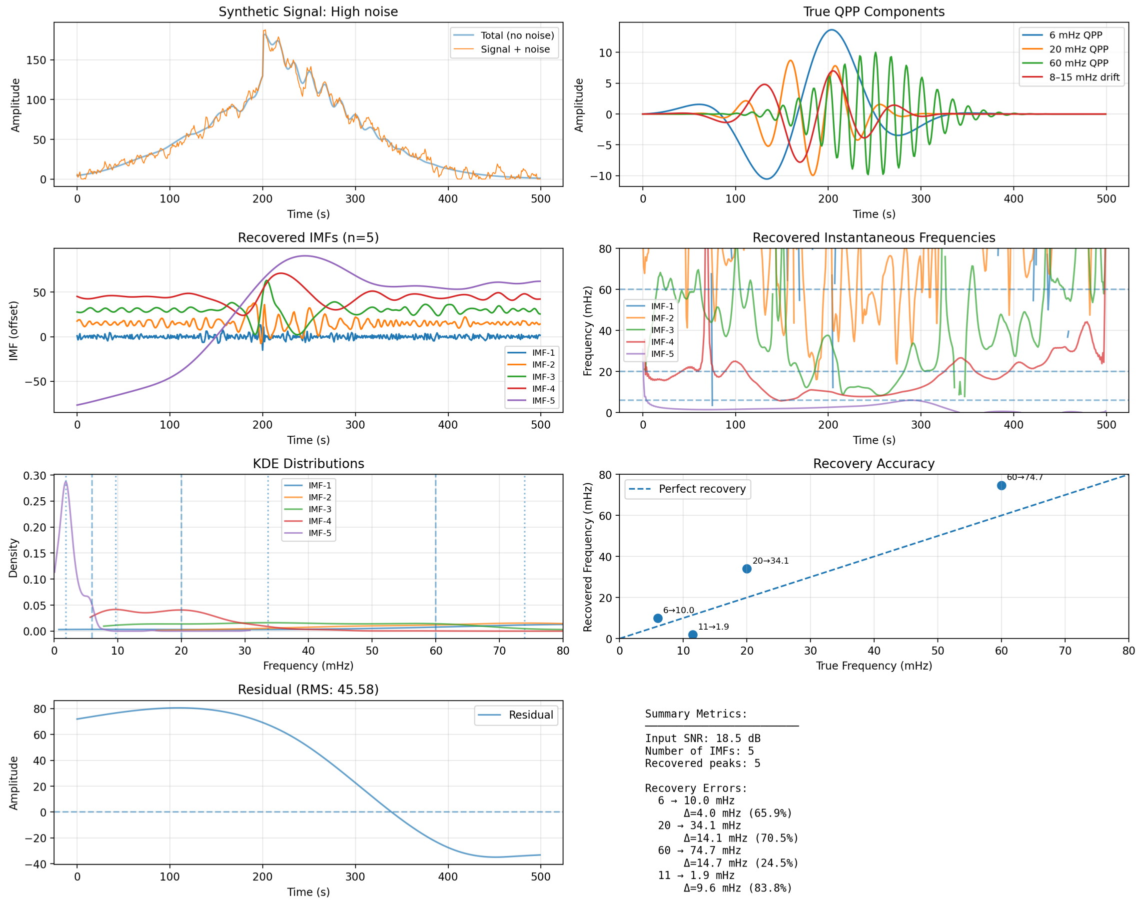

Figure B.4: Synthetic validation for the high-noise case. The calculated SNR is approximately 18.5 dB. Four of the four injected components satisfy the matching criterion in this particular realization. The result illustrates why a single noise realization is insufficient for defining a universal SNR-dependent detection threshold.

However, the synthetic tests also demonstrate that the existence of a KDE peak alone is insufficient to establish a physical QPP. Frequency peaks in the observational data should therefore be evaluated using multiple criteria, including persistence, statistical significance, robustness to KDE bandwidth, and agreement with an independent time–frequency method.

B.9.2 Interpretation of Low-Frequency Components

The validation does not establish a universal lower-frequency detection threshold. Nevertheless, it demonstrates the importance of signal duration for low-frequency oscillations.

For an oscillation of frequency f, the number of available cycles in an interval of duration T is

$$N_{\text{cycles}} = fT. \tag{B.14}$$

Consequently, a nominal frequency of 1 mHz corresponds to a period of 1000 s, and a short decay interval may contain fewer than one complete cycle. Such a feature cannot be treated as a well-established periodic oscillation without additional evidence.

This consideration is important when interpreting the lowest-frequency components in the real STIX observations.

B.9.3 Interpretation of High-Frequency Components

The synthetic results demonstrate that high-frequency components can be recovered by the EMD–Hilbert method, but their identification is sensitive to the decomposition and noise realization.

Therefore, the high-frequency components observed in the decay phase of the real flares should not be interpreted solely on the basis of their presence in the HHT spectrum.

Their interpretation should be supported by:

- persistence over multiple cycles;
- statistical significance against an appropriate noise model;
- robustness to KDE bandwidth;
- consistency with wavelet analysis; and
- , where available, correspondence with independent flare diagnostics.

B.9.4 Implications for Frequency-Drift Measurements

The present synthetic experiment included a nominal frequency-varying component. However, because the executed signal used the form $\sin[2\pi f(t)t]$ rather than the integrated phase of the prescribed instantaneous frequency, the experiment should not be interpreted as a quantitative validation of frequency-drift recovery.

A dedicated chirp experiment using

$$Q_{\text{chirp}}(t) = A(t) \sin\left[2\pi \int_0^t f(\tau)\, d\tau\right] \tag{B.15}$$

should be performed in future work to quantify the accuracy with which frequency evolution is recovered.

B.10 Limitations of the Synthetic Validation

Several limitations should be considered when applying the results of this validation to the STIX observations.

1. **Simplified noise model.** The validation uses an AR(1) red-noise process. Real STIX observations also contain Poisson counting statistics, instrumental effects, background variability, and potentially non-stationary noise.

2. **Limited parameter space.** Only a small number of frequencies, amplitudes, noise levels, and signal durations were tested. The results therefore do not define universal EMD resolution limits.

3. **Mode mixing.** The decomposition does not necessarily associate one IMF with one injected physical component. This is an intrinsic limitation that must be considered when assigning physical interpretations to individual IMFs.

4. **Finite signal duration.** Low-frequency oscillations are represented by relatively few cycles within a finite observation interval, limiting the confidence with which their periodicity can be established.

5. **KDE dependence.** The location and prominence of KDE peaks can depend on the bandwidth and on the instantaneous-frequency distribution. KDE bandwidth sensitivity should therefore be evaluated when identifying recurrent frequency bands.

6. **Implementation dependence.** The numerical results presented here were obtained with a self-contained classical EMD implementation because the exact software package used in the original observational analysis was not available in the validation environment. The numerical values should therefore not be interpreted as a bit-for-bit reproduction of the original EMD implementation.

7. **Frequency-drift construction.** The frequency-varying component used in the executed validation was constructed using $\sin[2\pi f(t)t]$. A mathematically exact prescribed instantaneous-frequency test requires the phase to be obtained from the integral of $f(t)$.

B.11 Summary

The synthetic validation demonstrates that the EMD–Hilbert analysis can recover several known oscillatory components embedded in a flare-like non-stationary signal under the tested conditions. The main quantitative results are summarized as follows:

1. The number of recovered IMFs varied from 2 in the ideal case to 5 in the noisy cases, demonstrating that IMF count is not directly equivalent to the number of physical oscillatory components.

2. Between two and four of the injected frequency components satisfied the frequency-matching criterion in the six validation scenarios.

3. The calculated SNRs for the low-, medium-, and high-noise cases were approximately 34.0, 24.5, and 18.5 dB, respectively.

4. Changing the random seed altered the detailed IMF decomposition while retaining a comparable number of identifiable frequency components.

5. The longer 1000-s signal produced four matched frequency components compared with three for the corresponding 500-s medium-noise signal, indicating that increased signal duration can improve frequency characterization.

6. The exploratory bootstrap test produced a stable KDE peak near 64.1 mHz with a 95% interval of approximately 61.8–66.6 mHz. Because this peak did not correspond to the injected 20 mHz component, the result demonstrates that bootstrap stability alone does not establish correct physical frequency identification.

7. The present experiment does not justify universal numerical values for the minimum detectable frequency, maximum detectable frequency, minimum frequency separation, or minimum SNR. These quantities require dedicated parameter-sweep experiments.

Overall, the synthetic tests support the use of the EMD–Hilbert approach as a tool for identifying candidate non-stationary oscillatory signatures, while also demonstrating that frequency peaks must be interpreted with appropriate statistical and methodological caution. In the context of the STIX flare analysis, the synthetic validation therefore supports the use of EMD–Hilbert as an exploratory time–frequency diagnostic, but does not by itself establish the physical origin of the observed QPPs or prove the presence of a turbulent cascade.

Bibliography

Aschwanden, M. J. (2004). *Physics of the solar corona: An introduction*. Springer. https://doi.org/10.1007/978-3-642-18830-3

Bhattacharjee, A, Huang, Y.-M., Yang, H, & Rogers, B. (2009). Fast reconnection in high-lundquist-number plasmas due to the plasmoid instability. *Physics of Plasmas*, *16*(11).

Biskamp, D. (2003). *Magnetohydrodynamic turbulence*. Cambridge University Press.

Brown, J. C. (1971). The deduction of energy spectra of non-thermal electrons in flares from the observed dynamic spectra of hard x-ray bursts. *Solar Physics*, *18*, 489–502.

Collier, H., Hayes, L. A., Battaglia, A. F., Harra, L. K., & Krucker, S. (2023). Characterising fast-time variations in the hard x-ray time profiles of solar flares using solar orbiter's stix. *Astronomy & Astrophysics*, *671*, A79.

Fletcher, L. (2024). Solar flare spectroscopy. *Annual Review of Astronomy and Astrophysics*, *62*(1), 437–474.

Frisch, U. (1995). *Turbulence: The legacy of a. n. kolmogorov*. Cambridge University Press.

Garutti, E. (2022). Silicon photomultipliers for high-energy physics and space applications. *Journal of Instrumentation*, *17*, C08017. https://doi.org/10.1088/1748-0221/17/08/C08017

Giovannelli, L., Berrilli, F., Casolino, M, Curti, F, Del Moro, D, Calchetti, D, Cantoresi, M, D'Ambrosio, A, Francisco, G, Giobbi, P, et al. (2023). Sun cube one: A multi-wavelength synoptic solar micro satellite. *Advances in Space Research*, *71*(4), 1995–2005.

Hathaway, D. H. (2015). The solar cycle. *Living reviews in solar physics*, *12*(1), 4.

Holman, G. D., Aschwanden, M. J., Aurass, H., et al. (2011). Implications of x-ray observations for electron acceleration and propagation in solar flares. *Space Science Reviews*, *159*, 107–166.

Huang, N. E., Shen, Z., Long, S. R., Wu, M. C., Shih, H. H., Zheng, Q., Yen, N.-C., Tung, C. C., & Liu, H. H. (1998). The empirical mode decomposition and the hilbert spectrum for nonlinear and non-stationary time series analysis. *Proceedings of the Royal Society of London. Series A: mathematical, physical and engineering sciences*, *454*(1971), 903–995.

Inglis, A. R., Zimovets, I., Dennis, B. R., Kontar, E., Nakariakov, V. M., Struminsky, A., & Tolbert, A. (2011). Instrumental oscillations in rhessi count rates during solar flares. *Astronomy & Astrophysics*, *530*, A47.

Kane, S., & Donnelly, R. (1971). Impulsive hard x-ray and ultraviolet emission during solar flares. *Astrophysical Journal, vol. 164, p. 151*, *164*, 151.

Kolmogorov, A. N. Dissipation of energy in the locally isotropic turbulence. In: In *Dokl. akad. nauk. sssr. 32*. 1941, 19–21.

Kolmogorov, N., Andre. (1995). *Turbulence: The legacy of an kolmogorov*. Cambridge university press.

Krucker, S., Hurford, G. J., Grimm, O., Kögl, S., Gröbelbauer, H.-P., Etesi, L., Casadei, D., Csillaghy, A., Benz, A. O., Arnold, N. G., et al. (2020). The spectrometer/telescope for imaging x-rays (stix). *Astronomy & Astrophysics*, *642*, A15.

Loureiro, N., Schekochihin, A. A., & Cowley, S. C. (2007). Instability of current sheets and formation of plasmoid chains. *Physics of Plasmas*, *14*(10).

McLaughlin, J., Nakariakov, V. M., Dominique, M, Jelínek, P, & Takasao, S. (2018). Modelling quasi-periodic pulsations in solar and stellar flares. *Space Science Reviews*, *214*(1), 45.

Nakariakov, V. M., & Melnikov, V. (2009). Quasi-periodic pulsations in solar flares. *Space Science Reviews*, *149*(1), 119–151.

Nakariakov, V., Ofman, L, Deluca, E., Roberts, B., & Davila, J. (1999). Trace observation of damped coronal loop oscillations: Implications for coronal heating. *Science*, *285*(5429), 862–864.

Neupert, W. M. (1968). Comparison of solar x-ray line emission with microwave emission during flares. *Astrophysical Journal, vol. 153, p. L59*, *153*, L59.

Nigro, G, Malara, F., & Veltri, P. (2008). Resonant behavior and fluctuating energy storage in coronal loops. *The Astrophysical Journal*, *685*(1), 606–621.

Ofman, L, & Sui, L. (2006). Oscillations of hard x-ray flare emission observed by rhessi: Effects of super-alfvénic beams? *The Astrophysical Journal Letters*, *644*(2), L149–L152.

Poghosyan, A., & Golkar, A. (2017). Cubesat evolution: Analyzing cubesat capabilities for conducting science missions. *Progress in Aerospace Sciences*, *88*, 59–83.

Priest, E. R., & Forbes, T. G. (2001). Magnetic reconnection: Mhd theory and applications, by er priest and tg forbes. cambridge university press, 2000. 600+ xii pages. isbn 0 521 481 79 1.£ 50, 85.. *Journal of Plasma Physics*, *66*(5), 363–367.

Rappazzo, A., Velli, M., Einaudi, G., & Dahlburg, R. (2008). Nonlinear dynamics of the parker scenario for coronal heating. *The Astrophysical Journal*, *677*(2), 1348–1366.

Roberts, B, Edwin, P., & Benz, A. (1984). On coronal oscillations. *Astrophysical Journal, Part 1 (ISSN 0004-637X), vol. 279, April 15, 1984, p. 857-865. Research supported by the Open University.*, *279*, 857–865.

Schrijver, C. J. (2009). Driving major solar flares and eruptions: A review. *Advances in Space Research*, *43*(5), 739–755.

Schwabe, H. (1844). Sonnenbeobachtungen im jahre 1843. *Astronomische Nachrichten*, *21*, 233.

Share, G. H., Murphy, R. J., White, S. M., et al. (2018). Characteristics of late-phase >100 mev gamma-ray emission in solar eruptive events. *The Astrophysical Journal*, *869*, 182.

Shibata, K. (1998). Evidence of magnetic reconnection in solar flares and a unified model of flares. *Astrophysics and Space Science*, *264*(1), 129–144.

Shibata, K., & Magara, T. (2011). Solar flares: Magnetohydrodynamic processes. *Living Reviews in Solar Physics*, *8*(1), 1–99.

Švestka, Z. Particle emission from solar flares. In: In *Solar flares*. Springer, 1976, pp. 238–299.

Tajima, T, Brunel, F, & Sakai, J. (1982). Loop coalescence in flares and coronal x-ray brightening. *Astrophysical Journal, Part 2-Letters to the Editor, vol. 258, July 1, 1982, p. L45-L48.*, *258*, L45–L48.

Tajima, T, Sakai, J, Nakajima, H, Kosugi, T, Brunel, F, & Kundu, M. (1987). Current loop coalescence model of solar flares. *Astrophysical Journal, Part 1 (ISSN 0004-637X), vol. 321, Oct. 15, 1987, p. 1031-1048.*, *321*, 1031–1048.

Terrell, G. R., & Scott, D. W. (1992). Variable kernel density estimation. *The annals of statistics*, 1236–1265.

Van Doorsselaere, T., Kupriyanova, E. G., & Yuan, D. (2016). Quasi-periodic pulsations in solar and stellar flares: An overview of recent results (invited review). *Solar Physics*, *291*(11), 3143–3164.

Woods, T. N., Eparvier, F. G., Jones, A., et al. (2014). New solar extreme-ultraviolet irradiance observations during flares. *Solar Physics*, *289*, 3391–3401.

Yashiro, S., Akiyama, S, Gopalswamy, N, & Howard, R. (2006). Different power-law indices in the frequency distributions of flares with and without coronal mass ejections. *The Astrophysical Journal Letters*, *650*(2), L143–L146.

Zhang, W, Jahoda, K, Swank, J., Morgan, E., & Giles, A. (1995). Dead-time modifications to fast fourier transform power spectra. *Astrophysical Journal v. 449, p. 930*, *449*, 930.

Zimovets, I., McLaughlin, J., Srivastava, A., Kolotkov, D., Kuznetsov, A., Kupriyanova, E., Cho, I.-H., Inglis, A., Reale, F, Pascoe, D., et al. (2021). Quasi-periodic pulsations in solar and stellar flares: A review of underpinning physical mechanisms and their predicted observational signatures. *Space Science Reviews*, *217*(5), 66.